Heat Integration Optimization and Dynamic Modeling Investigation for Advancing the Coal-Direct Chemical Looping Process

FINAL TECHNICAL REPORT

AWARDED UNDER

DOE/NETL DE-FE0029093

PREPARED BY

The Ohio State University

151 West Woodruff Ave

Columbus, OH 43210

PRINCIPAL INVESTIGATOR

Professor Andrew Tong

Phone: 614-361-7737

Tong.48@osu.edu

AUTHORS

Dikai Xu, Yu-Yen Chen, Jianhua Pan, Yitao Zhang, Dawei Wang, Yaswanth Pottimurthy, Thomas J. Flynn, Bartev Sakadjian, William Arnold, Travis Flower, Andrew S. Tong, Liang-Shih Fan

SUBMITTED TO

National Energy Technology Laboratory, Department of Energy

Table of Contents

Disclaimer

Executive Summary

The purpose of the project is to address the optimization and startup operation of a modular coal direct chemical looping (CDCL) combustion system integrated with a steam cycle for power generation to reduce the risks involved in further scale-up of the technology. The modular reactor design of the CDCL process provides flexibility in the fabrication of the reactor and in its operating capacity (i.e. turndown ratio) at the cost of a more complex heat exchange network (HEN) design and integration. To address the technology gaps and advance the efficiency and economic feasibility of the CDCL technology, the project will perform a detailed and comprehensive analysis of the integration of a modular CDCL reactor system and a steam cycle system under both static and transient conditions via HEN process performance simulations and system dynamic modeling, respectively. The scope of work consists of 1) Experimental and computational studies of the CDCL combustor reactor 2) Comprehensive static (i.e. steady-state) system HEN design analysis in CDCL 550 MWe commercial unit for power generation and 3) Dynamic modeling of site specific design of 10MWe CDCL large pilot plant.

The project team has successfully developed and validated a kinetic model for the oxidation of oxygen carriers in the combustor using the unreacted shrinking core model (UCSM). The model is capable of capturing the oxidation kinetics of fully or partially reduced oxygen carrier particles. A computational fluid dynamics (CFD) model is developed to simulate the hydrodynamics, heat transfer, and chemical reaction occurring in the CDCL combustor. The model is developed in MFIX and ANSYS Fluent. Key aspects of CDCL combustor operation, including heat transfer, oxygen carrier oxidation, and the transport of oxygen carrier particles, are simulated using this CFD model. The HEN for a commercial scale 550 MWe CDCL power plant is simulated and optimized using ASPEN Plus. Practical design considerations are incorporated based on industrial experiences. The performance and cost for the commercial CDCL plant is updated based on these analyses. A dynamic model for the 10 MWe CDCL pilot plant is developed in ProTRAX simulation software. The model is based on the pilot plant design developed in project DE-FE0027654 “10 MWe CDCL Large Pilot Plang – Pre-FEED Study” and the steam cycle data obtained from Dover Light & Power plant. The transient behaviors during pilot plant load variation are simulated using the dynamic model.

1. Modeling of Oxygen Carrier Oxidation Kinetics

In order to simulate the oxidation reaction kinetics of the oxygen carrier particles in the combustor, an unreacted shrinking core model (UCSM) is developed. The USCM considers three resistances that govern the reaction kinetics of the oxygen carrier particle.[1] These three resistances have been defined based on the oxidation mechanism where oxygen in the bulk gas phase diffuses through the gas film around the particle to reach its outer surface. It then diffuses through the product layer of the particle to react at the reaction interface. Therefore, the three resistances are: mass transfer from bulk gas phase to the outer surface of the particle (Gas film diffusion), diffusion through the different phases of the oxygen carrier particle (Intraparticle diffusion) and the chemical reaction at the interface.

1.1 Oxidation of Fully Reduced Oxygen Carrier Particles

The USCM developed for oxidation of fully reduced oxygen carrier particles, which considers three different phases and two reaction interfaces in the oxygen carrier particle as shown in Figure 1. The following assumptions have been made for the model:

1. The particle is assumed to be a perfectly spherical and no structural or volume change occurs during oxidation reaction.
2. The oxidation reaction takes place at isothermal conditions within the particle.
3. The oxidation of completely reduced oxygen carrier particle takes place in two steps i.e. from Fe to Fe^{2+} and Fe^{2+} to Fe^{3+}.[2] Therefore there are two chemical reaction interfaces in the particle as show in Figure 2.

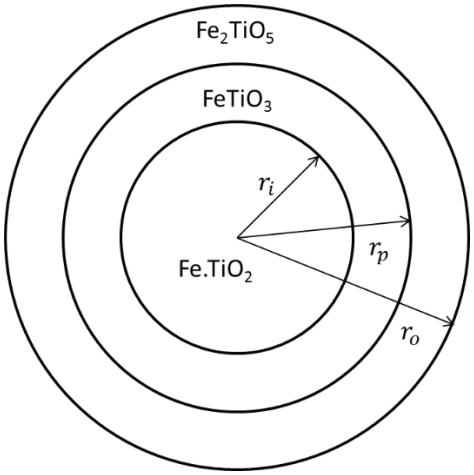

Figure 1 Representation of the oxygen carrier particle in the unreacted shrinking core model

In the USCM, a spherical particle of radius r_o is considered in a gaseous atmosphere with partial pressure of oxygen to be p_{b,O_2}, the other gas being nitrogen. The radius of the pseudobrookite (Fe_2TiO_5)-ilmenite ($FeTiO_3$) interface is denoted by r_p and that of ilmenite ($FeTiO_3$)-iron ($Fe.TiO_2$) interface by r_i, also, the oxygen partial pressures at these interfaces are denoted by p_{p,O_2} and p_{i,O_2}, respectively. The objective of this model is to determine the rate of oxygen consumption by the oxygen carrier particle which would then be used to calculate the rate of solids conversion. The rate of oxygen consumption will be affected by the mass transfer and chemical reaction resistances, which will act in series, based on the oxidation mechanism described above. The molar flow rate of oxygen as a function of the three resistances is as described below:

1) Gas film diffusion

The molar flow rate of oxygen into the particle across the gas film surrounding the particle ($N_{F,j}$) can be represented by

$$\mathrm{N_{F,O_2}} = -\frac{1}{\mathrm{R_{F,O_2}}}(\mathrm{p_{b,O_2}} - \mathrm{p_{o,O_2}}) \tag{1.1}$$

where,

$$\mathrm{R_{F,O_2}} = \frac{\mathrm{RT}}{\mathrm{k_{g,O_2} 4\pi r_o^2}} \tag{1.2}$$

is the gas film diffusion resistance and k_{g,O_2} is the mass transfer coefficient for O_2.

2) Intraparticle diffusion

The oxygen after reaching the surface of the particle will diffuse through the different product layers to get to the reaction interfaces. The molar rate of oxygen diffusion through the pseudobrookite (N_{S,p,O_2}) and ilmenite (N_{S,i,O_2}) product layer are:

a) Diffusion through Pseudobrookite layer

$$N_{S,p,O_2} = -\frac{1}{R_{S,p,O_2}}(p_{o,O_2} - p_{p,O_2}) \tag{1.3}$$

$$R_{S,p,O_2} = \frac{RT}{D_{p,O_2}^{eff}} \frac{(r_o - r_p)}{4\pi r_o r_p} \tag{1.4}$$

b) Diffusion through ilmenite layer

$$N_{S,i,O_2} = -\frac{1}{R_{S,i,O_2}}(p_{p,O_2} - p_{i,O_2}) \tag{1.5}$$

$$R_{S,i,O_2} = \frac{RT}{D_{i,O_2}^{eff}} \frac{(r_p - r_i)}{4\pi r_i r_p} \tag{1.6}$$

where, R_{S,p,O_2}, R_{S,i,O_2} and D_{p,O_2}^{eff} , D_{i,O_2}^{eff} represent the resistance to oxygen diffusion and diffusivity of oxygen through the pseudobrookite and ilmenite product layers, respectively.

3) Chemical reaction

The rate of oxygen consumption at the pseudobrookite-ilmenite interface (N_{I,p,O_2}) and ilmenite-iron interface (N_{I,i,O_2}) because of chemical reaction are

a) Pseudobrookite-ilmenite interface

$$N_{I,p,O_2} = -\frac{1}{R_{I,p,O_2}}\left(p_{p,O_2}{}^{a}\right) \tag{1.7}$$

$$R_{I,p,O_2} = \frac{(RT)^a}{k_{p,r}4\pi {r_p}^2} \tag{1.8}$$

b) Ilmenite-iron interface

$$N_{I,i,O_2} = -\frac{1}{R_{I,i,O_2}}\left(p_{i,O_2}{}^{b}\right) \tag{1.9}$$

$$R_{I,i,O_2} = \frac{(RT)^b}{k_{i,r}4\pi {r_i}^2} \tag{1.10}$$

where $k_{p,r}$, $k_{i,r}$ and a, b are the reaction rate constant and reaction rate order with respect to oxygen for pseudobrookite-ilmenite interface and ilmenite-iron interface, respectively.

The three different resistances can be combined to form one generalized expression by oxygen material balance over the entire particle. Starting from the interior of the particle, the rate of oxygen consumption at the ilmenite-iron interface is equal to the rate of oxygen diffusion through the ilmenite product layer as represented by the following equation,

$$N_{I,i,O_2} = N_{S,i,O_2} \tag{1.11}$$

The rate of oxygen diffusion across the pseudobrookite product layer will be a sum of the rate of oxygen diffusion through the ilmenite product layer and the rate of oxygen consumption at the pseudobrookite-ilmenite interface as given below,

$$N_{S,p,O_2} = N_{S,i,O_2} + N_{I,p,O_2} \tag{1.12}$$

Finally, the rate of oxygen diffusion through the gas film at the exterior of the particle will be equal to the rate of oxygen diffusion through the pseudobrookite product layer i.e.

$$N_{F,j} = N_{S,p,O_2} \tag{13}$$

Equations (1.11), (1.12) and (1.13) would be solved simultaneously to evaluate the oxygen partial pressures at the exterior surface of the particle and the two reaction interfaces, which would

be difficult to measure experimentally, in terms of the easily measurable oxygen partial pressure in the gas bulk phase.

From equation (1.11),

$$-\frac{1}{R_{I,i,O_2}}\left(p_{i,O_2}{}^{b}\right) = -\frac{1}{R_{S,i,O_2}}\left(p_{p,O_2} - p_{i,O_2}\right)$$

$$p_{p,O_2} = \frac{R_{S,i,O_2}}{R_{I,i,O_2}}\left(p_{i,O_2}{}^{b}\right) + p_{i,O_2} \tag{1.14}$$

From equation (1.12),

$$-\frac{1}{R_{S,p,O_2}}\left(p_{o,O_2} - p_{p,O_2}\right) = -\frac{1}{R_{S,i,O_2}}\left(p_{p,O_2} - p_{i,O_2}\right) - \frac{1}{R_{I,p,O_2}}\left(p_{p,O_2}{}^{a}\right)$$

$$p_{o,O_2} = p_{p,O_2} + \frac{R_{S,p,O_2}}{R_{I,p,O_2}}\left(p_{p,O_2}{}^{a}\right) + \frac{R_{S,p,O_2}}{R_{S,i,O_2}}\left(p_{p,O_2} - p_{i,O_2}\right)$$

$$p_{o,O_2} = \frac{R_{S,i,O_2}}{R_{I,i,O_2}}\left(p_{i,O_2}{}^{b}\right) + p_{i,O_2} + \frac{R_{S,p,O_2}}{R_{I,p,O_2}}\left[\frac{R_{S,i,O_2}}{R_{I,i,O_2}}\left(p_{i,O_2}{}^{b}\right) + p_{i,O_2}\right]^{a} + \frac{R_{S,p,O_2}}{R_{I,i,O_2}}\left(p_{i,O_2}{}^{b}\right) \tag{1.15}$$

From equation (1.13),

$$-\frac{1}{R_{F,O_2}}\left(p_{b,O_2} - p_{o,O_2}\right) = -\frac{1}{R_{S,p,O_2}}\left(p_{o,O_2} - p_{p,O_2}\right)$$

$$p_{b,O_2} = \left(1+\frac{R_{F,O_2}}{R_{S,p,O_2}}\right) p_{o,O_2} - \frac{R_{F,O_2}}{R_{S,p,O_2}} p_{p,O_2}$$

$$p_{b,O_2} = \left(1 + \frac{R_{F,O_2}}{R_{S,p,O_2}}\right)\left\{\frac{R_{S,i,O_2}}{R_{I,i,O_2}}\left(p_{i,O_2}{}^{b}\right) + p_{i,O_2} + \frac{R_{S,p,O_2}}{R_{I,p,O_2}}\left[\frac{R_{S,i,O_2}}{R_{I,i,O_2}}\left(p_{i,O_2}{}^{b}\right) + p_{i,O_2}\right]^{a} + \frac{R_{S,p,O_2}}{R_{I,i,O_2}}\left(p_{i,O_2}{}^{b}\right)\right\} - \frac{R_{F,O_2}}{R_{S,p,O_2}}\left\{\frac{R_{S,i,O_2}}{R_{I,i,O_2}}\left(p_{i,O_2}{}^{b}\right) + p_{i,O_2}\right\} \tag{1.16}$$

Once the partial pressures of oxygen at the reaction interfaces are known from equations (1.14), (1.15) and (1.16), it would be possible to calculate the rate of oxidation reaction at the two reaction interfaces. The oxidation reaction would result in volume change of the product phase which can be represented by the following general equation

$$\sigma c_o \frac{dV}{dt} = 4\pi r^2 \frac{k_r}{(RT)^n} p_{O_2}{}^{n} \tag{1.17}$$

Where V is the volume of the product phase, r is the radius of the product layer, c_o is the oxygen density, σ is the fraction of oxygen density to convert from the reactant to product phase, k_r is the reaction rate constant, p_{O_2} is the partial pressure of the oxygen and n is the order of reaction with respect to oxygen. Equation (1.17) can be modified to calculate the rate of interface radii growth as follows

$$\frac{dr_p}{dt} = -\frac{k_{p,r}}{\sigma_p c_{p,o}}\left(\frac{p_{p,O_2}}{RT}\right)^a \tag{1.18}$$

$$\frac{dr_i}{dt} = -\frac{k_{i,r}}{\sigma_i c_{i,o}}\left(\frac{p_{i,O_2}}{RT}\right)^b \tag{1.19}$$

The rate of interface growth would determine the rate of product layer growth and hence the rate of solids conversion, where the solids conversion is calculated using

$$X = \frac{\sigma_p\left[r_o^3 - (r_p)^3\right] + \sigma_i\left[(r_p)^3 - (r_i)^3\right]}{r_o^3} \tag{1.20}$$

In the USCM model developed above there are six unknown parameters which would have to be determined experimentally. The unknown parameters are reaction rate constants ($k_{p,r}$, $k_{i,r}$), reaction rate orders (a, b) with respect to oxygen and the effective oxygen diffusivities (D_{p,O_2}^{eff} , D_{i,O_2}^{eff}) in the product layers.

The oxidation experiments to determine the reaction rate order and reaction rate constants were done at 800°C to operate in a region where the kinetics was reaction controlled rather than diffusion controlled. It was for determining the activation energy that the experiments were conducted at 5% and 10% O_2, respectively, at temperatures of 900°C and 1000°C. In the TGA, 20mg of oxygen carrier sample was used and it was first dried at 200°C under N_2 flow of 248 ml/min, before ramping up to 800°C under the same flow. After reaching the desired temperature, the gas was switched to the desired O_2 concentration stream by mixing air and N_2 gas streams via gas manifold mixing panel while keeping the total flow rate at 248ml/min. After reaching a steady weight under the oxygen containing gas stream, the TGA reactor was flushed with N_2 and then 50% H_2/N_2 gas was sent to reduce the sample completely. The same concentration of oxygen gas was then sent in till the sample reached a steady weight.

The chemical reaction rate expressions for both the phases can be rewritten as follows

(a) Pseudobrookite-ilmenite interface

$$N_{I,p,O_2} = -\frac{1}{R_{I,p,O_2}}\left(p_{p,O_2}{}^a\right)$$

$$R_{I,p,O_2} = \frac{(RT)^a}{k_{p,r} 4\pi {r_p}^2}$$

$$\log_{10} N_{I,p,O_2} = \log_{10} k_{p,r} 4\pi {r_p}^2 + a \log_{10} \frac{p_{p,O_2}}{RT} \tag{1.21}$$

(b) Ilmenite-iron interface

$$N_{I,i,O_2} = -\frac{1}{R_{I,i,O_2}}({p_{i,O_2}}^b)$$

$$R_{I,i,O_2} = \frac{(RT)^b}{k_{i,r}4\pi {r_i}^2}$$

$$\log_{10} N_{I,i,O_2} = \log_{10} k_{i,r}4\pi {r_p}^2 + b \log_{10} \frac{p_{i,O_2}}{RT} \quad (1.22)$$

Finding the reaction rate kinetic parameters at the pseudobrookite-ilmenite interface and ilmenite-iron interface is equivalent to finding them for $FeTiO_3$ and Fe phases respectively. The maximum rate of weight change observed while oxidizing both, $FeTiO_3$ and Fe, was measured and recorded as the initial rate of reaction. The maximum rate of weight change was converted to units of mol/s by dividing it by molecular weight of O_2 and then divided by the sample weight used to calculate the reaction rate on sample weight basis. $\log_{10}(reaction\ rate)$ was plotted against $\log_{10}(p_{O_2}/RT)$ for both powder samples. Equations (1.21) and (1.22) were used to fit the experimental data to obtain the values of reaction rate constants and reaction rate orders. The intercept and slope of the line obtained from linear fitting was used to determine the reaction rate constant and reaction rate orders, respectively. However, the reaction rate constant obtained from the experimental data was on a weight basis and hence to convert it to a basis of surface area, the following expression was used

$$\begin{aligned} k_w \times sample\ mass &= k_s \times sample\ surface\ area \\ &= k_s \times Number\ of\ particles \times Surface\ area\ of\ one\ particle \\ &= k_s \times \frac{Sample\ mass}{Mass\ of\ one\ particle} \times \pi d^2 \times \frac{1}{Sample\ mass} \\ &= k_s \times \frac{1}{\pi/_6\, d^3 \rho} \times \pi d^2 \end{aligned}$$

where k_w and k_s are the reaction rate constants based on the sample weight and surface area, respectively, d is the diameter of one particle i.e. 69 microns and ρ is the density of particle i.e. 4.5 g/cm^3.

Therefore, $k_s = 0.052k_w$. Here k_s is equivalent to $k_{p,r}$ and $k_{i,r}$ in equations (1.21) and (1.22), respectively. Equations (1.21) and (1.22) can be further expanded as

$$\log_{10} N_{I,p,O_2} = \log_{10} {k_{p,r}}^o 4\pi {r_p}^2 - \frac{E_{p,r}}{RT} + a \log_{10} \frac{p_{p,O_2}}{RT} \quad (1.23)$$

$$\log_{10} N_{I,i,O_2} = \log_{10} {k_{i,r}}^o 4\pi {r_p}^2 - \frac{E_{i,r}}{RT} + b \log_{10} \frac{p_{i,O_2}}{RT} \quad (1.24)$$

where $k_{p,r}{}^{o}$ and $k_{i,r}{}^{o}$ are pre-exponential factors and $E_{p,r}$ and $E_{i,r}$ are the activation energies for $FeTiO_3$ and Fe, respectively. Equations (1.23) and (1.24) were used to fit the experimental data obtained at temperatures of 800°C, 900°C and 1000°C, and oxygen partial pressure for $FeTiO_3$ and Fe of 5% and 10%, respectively. The fittings were performed in MATLAB using the trust-region-reflective algorithm to reach a convergence criterion of 10^{-5}.

Figure 1 and Figure 2 show the reaction rate experimental data obtained for $FeTiO_3$ and Fe powders, respectively, from the TGA at 800°C at different concentrations of oxygen. The equation of line obtained from using linear fit in Microsoft excel is also shown in the figures. Table 1 shows the values of the reaction rate constants and reaction rate orders based on the intercept and slope of the lines shown in Figure 2 and Figure 3. The pre-factor and activation energy fittings based on experimental results at different temperatures are shown in Figure 4, and the corresponding rate constants are summarized in Table 2.

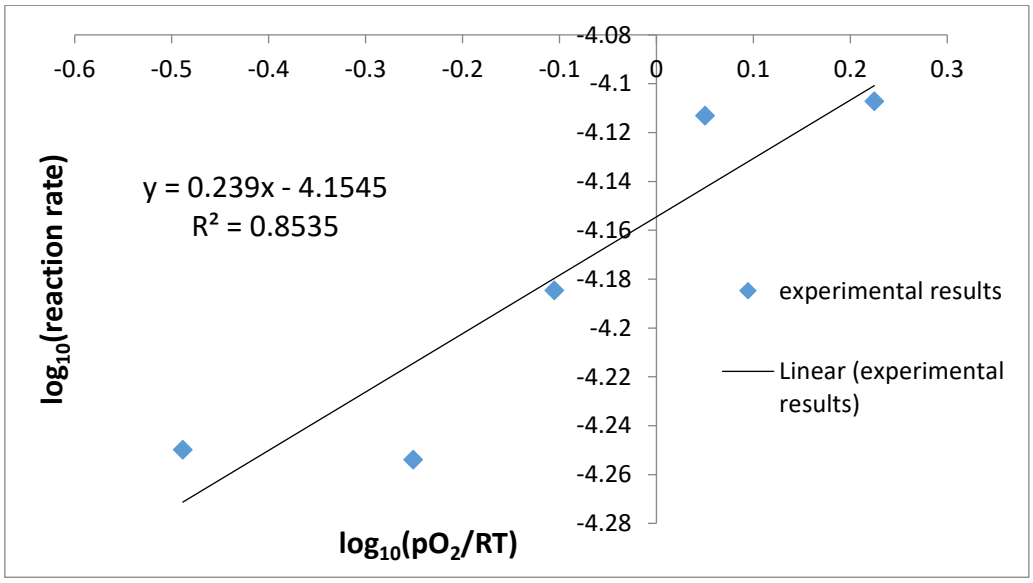

Figure 2 Experimental results for oxidation of $FeTiO_3$ powder at 800°C under different O_2 concentrations in a TGA. (◆) experimental data (──) linear fit in excel

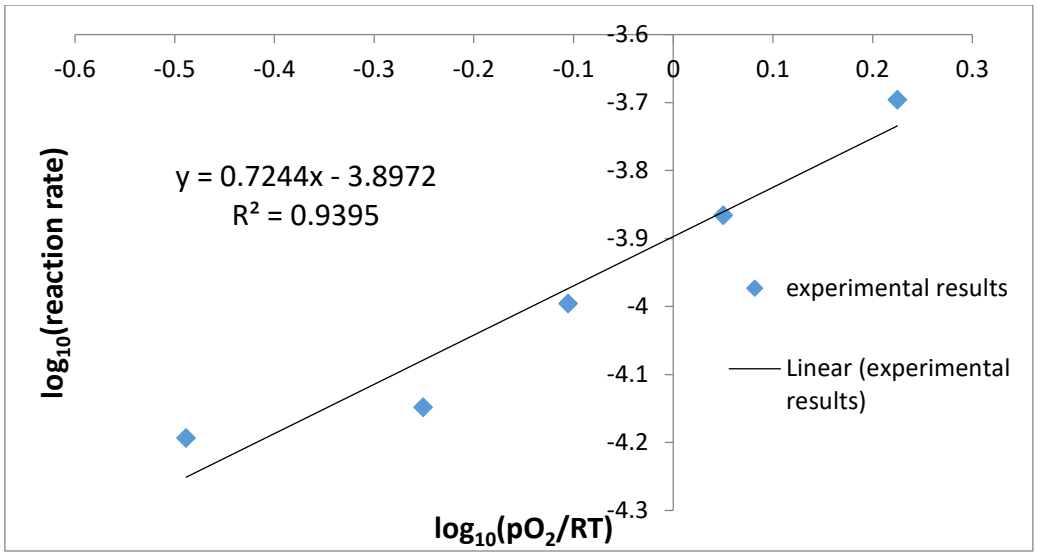

Figure 3 Experimental results for oxidation of $FeTiO_3$ powder at 800°C under different O_2 concentrations in a TGA. (◆) experimental data (──) linear fit in excel

Table 1 Reaction rate constants and reaction rate orders for $FeTiO_3$ and Fe phases

Phase	**$FeTiO_3$**		**Fe**	
Reaction rate constant	$k_{p,r}$ at 800°C ($mol^{0.761}m^{-1.238}s^{-1}$)	$3.66x10^{-6}$	$k_{i,r}$ at 800°C ($mol^{0.276}m^{0.172}s^{-1}$)	$6.66x10^{-6}$
Reaction rate order	a	0.239	b	0.724

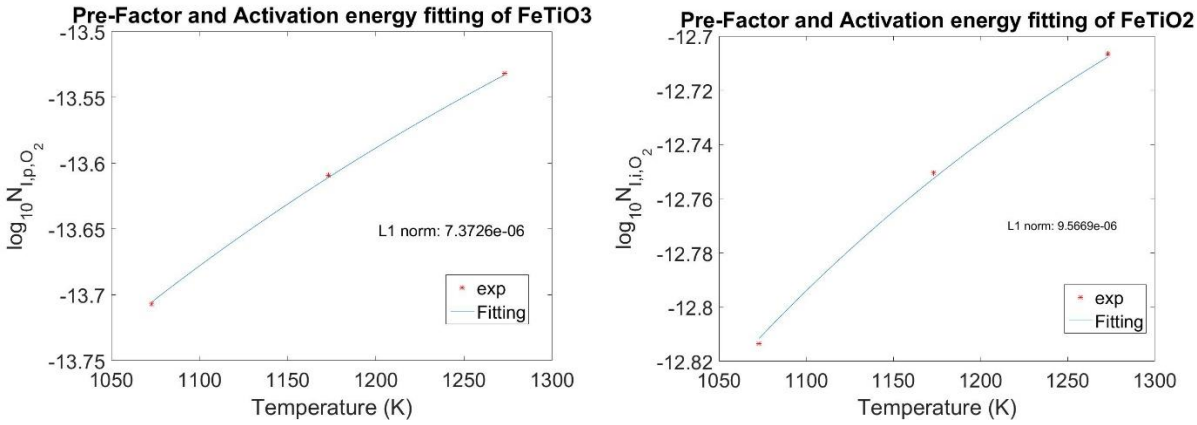

Figure 4 Pre-factor and activation energy fitting results of $FeTiO_3$ and Fe oxidation under different temperature, where asterisk represents the experimental data and solid line is the fitting result

Table 2 Activation energies and reaction rate constants and reaction rate orders for $FeTiO_3$ and Fe phases under different temperatures

Phase	$FeTiO_3$		Fe	
Activation energy (J/mol.K)	$E_{p,r}$	12929	$E_{i,r}$	13400
Reaction rate constants	$k_{p,r}$ at 900°C ($mol^{0.761}m^{-1.238}s^{-1}$)	$4.14x10^{-6}$	$k_{i,r}$ at 900°C ($mol^{0.276}m^{0.172}s^{-1}$)	$7.57x10^{-6}$
	$k_{p,r}$ at 1000°C ($mol^{0.761}m^{-1.238}s^{-1}$)	$4.59x10^{-6}$	$k_{i,r}$ at 1000°C ($mol^{0.276}m^{0.172}s^{-1}$)	$8.43x10^{-6}$

The effective oxygen diffusivities were estimated using the following equation:[3]

$$D_{t,O_2}^{eff} = D_{N_2-O_2}\frac{\in}{\tau} \quad (1.25)$$

where D_{p,O_2} is the diffusivity coefficient, $\in$ is the porosity and τ is the tortuosity of the phase t.

The diffusivity coefficients for O_2 in N_2 were determined using equation proposed by Fuller et al. for low pressure binary gas systems:[4-6]

$$D_{A-B} = \frac{0.00143\,T^{1.75}}{PM_{AB}^{1/2}[(\sum_v A)^{\frac{1}{3}}+(\sum_v B)^{\frac{1}{3}}]^2} \quad (1.26)$$

where T is the temperature, P is pressure, M_{AB} is the reduced molecular mass i.e. $(\left({}^{1}/_{M_A}\right)+({}^{1}/_{M_B}))^{-0.5}$ for molecules A and B, and $\sum_v$ A and $\sum_v$ B are the diffusion volumes of molecules A and B. For the oxidation experiments molecules A and B are N_2 and O_2, respectively. $D_{N_2-O_2}$, was thus equal to $2.64x10^{-4}$ m^2/s at a temperature of 1273K and pressure of 1 bar. The values of porosities for oxygen carrier particles containing majority of $FeTiO_3$ and Fe phase were estimated using pore volume measurement in a NOVA 4200e Quantachrome Brunauer−Emmett−Teller (BET) analyzer to be 0.0315 and 0.009, respectively. The tortuosity values for both phases was assumed to be 2. Therefore, from equation (25), the diffusivity values for the $FeTiO_3$ and Fe phases at 1273K are estimated as $4.16\ x10^{-6}$ m^2/s and $1.19\ x10^{-6}$ m^2/s, respectively.

Oxidation experiments were carried out for oxygen carrier particles that are representative of those used in the CDCL process. The results of these experiments were used to test the accuracy of the USCM model developed and the various kinetic parameters determined above.

The oxygen carrier particles of 1.5mm diameter were used for these experiments carried out in the TGA. These particles were initially sintered at 950°C under air for 12hrs. Only one

oxygen carrier particle was used for the experiment. Oxidation was carried out on particles that were completely reduced as well as partially reduced. Experiments were repeated three times at 1000°C and O_2 concentration of 5%, which represents the operating condition of the combustor in the subpilot chemical looping system.

The oxygen carrier particle was first dried at 200°C for 15 minutes under 248ml/min flow of N_2 before ramping up to the desired temperature. The gas flow was then switched to 50% H_2/N_2 to reduce the particle either completely or partially by varying the reduction times. After reducing the particle, the TGA reactor was flushed with N_2 and gas of the required O_2 concentration was then injected till complete oxidation of the particle.

In order to determine the relation between conversion and time, the system of equations in the proposed model is solved numerically. Setting both r_p and r_i initially equal to the particle radius, the following calculation procedure is implemented at each time increment:

1. The mass transfer resistances (i.e., resistances from gas film diffusion, intraparticle diffusion, and chemical reaction in different phases) are calculated at the current time step. One thing worth mentioning here is that the resistances of the intraparticle diffusion are approximated to zero at the very first time step to avoid the numerical singularity.

2. The oxygen partial pressure at the $Fe/FeTiO_3$ interface, p_{i,O_2}, is solved according to equation (1.16) using Newton's method with termination tolerance set at $1x10^{-20}$. The oxygen partial pressure at the $FeTiO_3/Fe_2TiO_5$ interface, p_{p,O_2}, can subsequently be obtained.

3. The updated position of core radii can be calculated based on the following system of ordinary differential equations:

$$\frac{dr_p}{dt} = -\frac{k_{p,r}}{\sigma_p c_{p,o}}\left(\frac{p_{p,O_2}}{RT}\right)^a \tag{1.27}$$

$$\frac{dr_i}{dt} = -\frac{k_{i,r}}{\sigma_i c_{i,o}}\left(\frac{p_{i,O_2}}{RT}\right)^b \tag{1.28}$$

where c_o is the oxygen density, and σ is the fraction of oxygen density to convert from the reactant to product phase. A classical fourth order Runge-Kutta method with a constant time step size of 0.5 second is implemented to solve equation (1.27) and (1.28). In addition, if any updated core radius is smaller than 1% of the original particle radius, the particular phase is considered to be fully oxidized and its core radius updated process is terminated.

4. Calculations return to step one. If both the positions of the core radii are less than 1% of the original particle radius, the whole oxidation process is considered to be completed, and the numerical simulation stops.

Figure 5 to Figure 7 compare results between proposed oxidation unreacted shrinking core model with experimental data in TGA at 1000°C and 5% O_2, which were repeated three times, and the results show the proposed model matches the experimental data well.

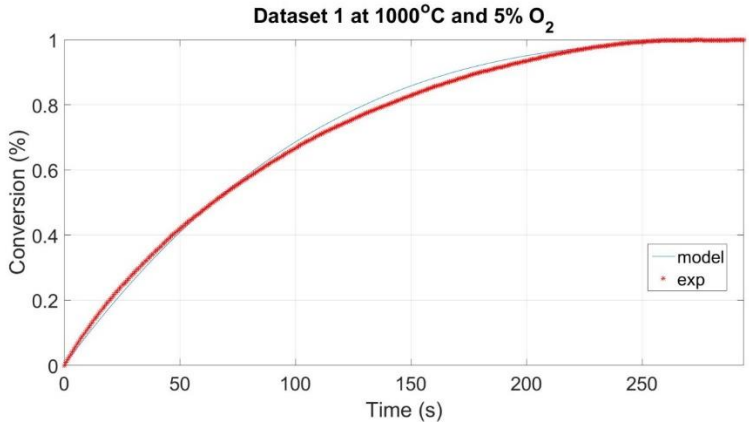

Figure 5 Comparison between TGA experimental data and model results at 1000°C and 5% O_2

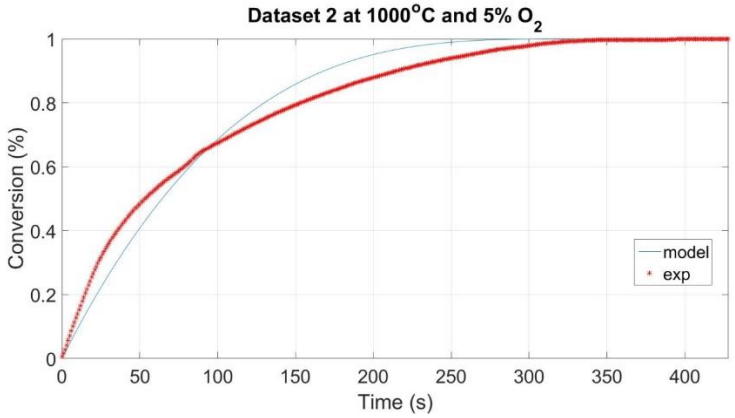

Figure 6 Comparison between TGA experimental data and model results at 1000°C and 5% O_2

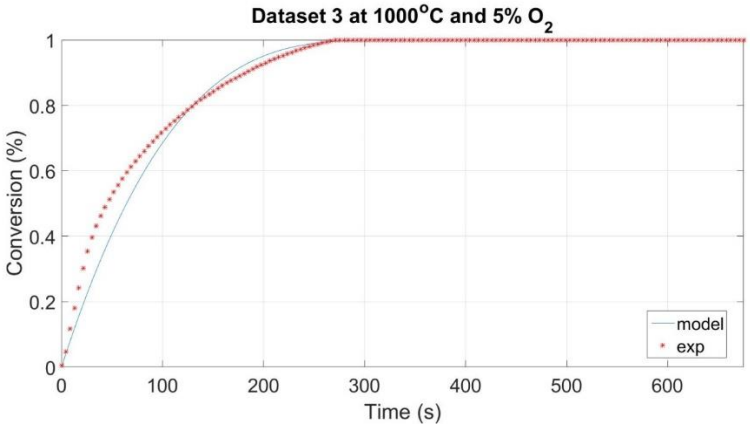

Figure 7 Comparison between TGA experimental data and model results at 1000°C and 5% O_2

1.2 Effect of Particle Morphology

In the previous model, morphological effects are neglected, and the oxygen carrier particle is assumed to be composed of only solid phases with no voids. The no-voids assumption, however, might oversimplify the problem since oxygen carrier particles should actually be porous so that gases can diffuse via the shell layers. In this part, morphological parameters like porosity and effective surface area are integrated into the model to enable it to capture the essential oxidation behaviors in the porous oxygen carrier particle. The basis of the model for oxidation of fully reduced particles remains the same as shown in Figure 1, in which three different phases and two reaction interfaces are presented during oxidation. Mass transfer resistances considered in the model include gas film diffusion, intra-particle gas diffusion, and interface chemical reaction.

To incorporate the morphological effects into the model, the following two modifications are adopted: (1) directly using $4\pi r^2$ to account for the surface area might underestimate the effective surface area due to the fact that the surface might be highly irregular and porous. Hence, the effective surface area is formulated as $\alpha(4\pi r^2)$, where α is a morphological parameter to describe the complex structure of the surface, (2) the solid volume terms are corrected with the $(1-\epsilon_i)$ term, where ϵ_i is the porosity of phase i. Note that the above two modifications would not affect the procedure for solving partial pressure at each interface since the α term is involved in all mass transfer resistances and would therefore be cancelled out. The expressions for the rate of change of core radii are now modified to be:

$$\frac{dr_p}{dt} = -\frac{\alpha_p k_{p,r}}{(1-\varepsilon_p)\sigma_p c_{p,o}}\left(\frac{p_{p,O_2}}{RT}\right)^a \tag{1.29}$$

$$\frac{dr_i}{dt} = -\frac{\alpha_i k_{i,r}}{(1-\varepsilon_i)\sigma_i c_{i,o}} \left(\frac{p_{i,O_2}}{RT}\right)^b \tag{1.30}$$

1.3 Oxidation of Partially Reduced Oxygen Carrier Particles

In the CDCL operating condition, oxygen carrier particles in the reducer are partially reduced to Fe/$FeTiO_3$ mixture to prevent particles from melting. However, the topochemical fashion in reduction is opposite to that of oxidation, and therefore, the inner core becomes $FeTiO_3$ while the outer shell is Fe. This makes the previous proposed model incapable of describing such scenario.

The schematic representation of oxidation for partially reduced particle is shown in Figure 8, where r_{Fe} denotes the initial interface between the Fe.TiO_2/$FeTiO_3$ phases in the mixture, and r_p, stands for the core radius of the inner Fe_2TiO_5 product layer.

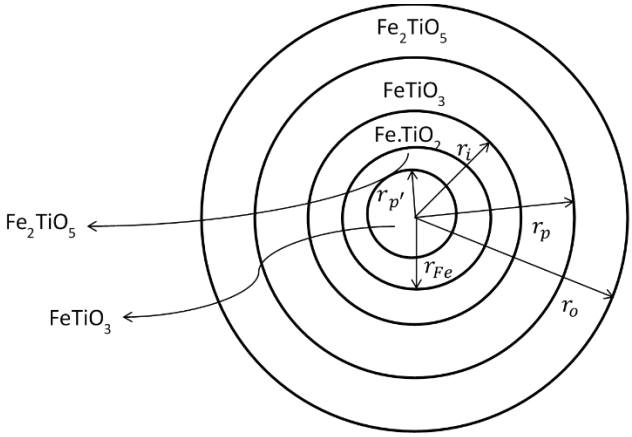

Figure 8 Schematic representation of USCM for partially reduced particles

The development of the oxidation model for the partially reduced particle is similar to the fully reduced particle.

1) Gas film diffusion

The molar flow rate of oxygen into the particle across the gas film surrounding the particle ($N_{F,j}$) can be represented by

$$N_{F,O_2} = -\frac{1}{R_{F,O_2}}(p_{b,O_2} - p_{o,O_2}) \tag{1.31}$$

Where

$$R_{F,O_2} = \frac{RT}{k_{g,O_2}\alpha 4\pi r_o^2} \tag{1.32}$$

is the gas film diffusion resistance and k_{g,O_2} is the mass transfer coefficient for O_2.

2) Intraparticle diffusion

The oxygen after reaching the surface of the particle will diffuse through the different product layers to get to the reaction interfaces. The molar rate of oxygen diffusion through the pseudobrookite (N_{S,p,O_2}), ilmenite (N_{S,i,O_2}), Fe.TiO_2 (N_{S,Fe,O_2}) and inner pseudobrookite (N_{S,p',O_2}) product layer are:

a) Diffusion through Pseudobrookite layer

$$N_{S,p,O_2} = -\frac{1}{R_{S,p,O_2}}(p_{o,O_2} - p_{p,O_2}) \tag{1.33}$$

$$R_{S,p,O_2} = \frac{RT}{D^{eff}_{p,O_2}} \frac{(r_o - r_p)}{\alpha 4\pi r_o r_p} \tag{1.34}$$

b) Diffusion through ilmenite layer

$$N_{S,i,O_2} = -\frac{1}{R_{S,i,O_2}}(p_{p,O_2} - p_{i,O_2}) \tag{1.35}$$

$$R_{S,i,O_2} = \frac{RT}{D^{eff}_{i,O_2}} \frac{(r_p - r_i)}{\alpha 4\pi r_i r_p} \tag{1.36}$$

c) Diffusion through Fe.TiO_2 layer

$$N_{S,Fe,O_2} = -\frac{1}{R_{S,Fe,O_2}}(p_{i,O_2} - p_{Fe,O_2}) \tag{1.37}$$

$$R_{S,Fe,O_2} = \frac{RT}{D^{eff}_{Fe,O_2}} \frac{(r_i - r_{Fe})}{4\pi\alpha r_i r_{Fe}} \tag{1.38}$$

d) Diffusion through inner Pseudobrookite layer

$$N_{S,p',O_2} = -\frac{1}{R_{S,p',O_2}}(p_{Fe,O_2} - p_{p',O_2}) \tag{1.39}$$

$$R_{S,p',O_2} = \frac{RT}{D^{eff}_{p',O_2}} \frac{(r_{Fe} - r_{p'})}{4\pi\alpha r_{Fe} r_{p'}} \tag{1.40}$$

where, R_{S,p,O_2}, R_{S,i,O_2}, R_{S,Fe,O_2}, R_{S,p',O_2} and D^{eff}_{p,O_2}, D^{eff}_{i,O_2}, D^{eff}_{Fe,O_2}, D^{eff}_{p',O_2} represent the resistance to oxygen diffusion and diffusivity of oxygen through the pseudobrookite, ilmenite, Fe.TiO_2 and inner pseudobrookite product layers, respectively.

3) Chemical reaction

The rate of oxygen consumption at the pseudobrookite-ilmenite interface (N_{I,p,O_2}), ilmenite-iron interface (N_{I,i,O_2}) and inner Pseudobrookite-ilmenite interface (N_{I,p',O_2}) because of chemical reaction are

a) Pseudobrookite-ilmenite interface

$$N_{I,p,O_2} = -\frac{1}{R_{I,p,O_2}}\left(p_{p,O_2}{}^{a}\right) \tag{1.41}$$

$$R_{I,p,O_2} = \frac{(RT)^a}{k_{p,r}\alpha 4\pi {r_p}^2} \tag{1.42}$$

b) Ilmenite-iron interface

$$N_{I,i,O_2} = -\frac{1}{R_{I,i,O_2}}\left(p_{i,O_2}{}^{b}\right) \tag{1.43}$$

$$R_{I,i,O_2} = \frac{(RT)^b}{k_{i,r}\alpha 4\pi {r_i}^2} \tag{1.44}$$

c) Inner pseudobrookite-ilmenite interface

$$N_{I,p',O_2} = -\frac{1}{R_{I,p',O_2}}\left(p_{p',O_2}{}^{a}\right) \tag{1.45}$$

$$R_{I,p',O_2} = \frac{(RT)^a}{k_{p,r}\alpha 4\pi {r_{p'}}^2} \tag{1.46}$$

where $k_{p,r}$, $k_{i,r}$ and a, b are the reaction rate constant and reaction rate order with respect to oxygen for pseudobrookite-ilmenite interface and ilmenite-iron interface, respectively.

The three different resistances can be combined to form one generalized expression by oxygen material balance over the entire particle. Starting from the interior of the particle, the rate of oxygen consumption at the inner pseudobrookite-ilmenite interface is equal to the rate of oxygen diffusion through the inner pseudobrookite product layer as represented by the following equation,

$$N_{I,p',O_2} = N_{S,p',O_2} \tag{1.47}$$

The rate of oxygen diffusion across the inner pseudobrookite product layer will be equal to the rate of oxygen diffusion through the $Fe.TiO_2$ as given below,

$$N_{S,p',O_2} = N_{S,Fe,O_2} \tag{1.48}$$

The rate of oxygen diffusion across the ilmenite product layer will be a sum of the rate of oxygen diffusion through the $Fe.TiO_2$ layer and the rate of oxygen consumption at the ilmenite-iron interface as given below,

$$N_{S,Fe,O_2} + N_{I,i,O_2} = N_{S,i,O_2} \tag{1.49}$$

The rate of oxygen diffusion across the pseudobrookite-ilmenite product layer will be a sum of the rate of oxygen diffusion through the ilmenite layer and the rate of oxygen consumption at the pseudobrookite-ilmenite interface as given below,

$$N_{S,i,O_2} + N_{I,p,O_2} = N_{S,p,O_2} \tag{1.50}$$

Finally, the rate of oxygen diffusion through the gas film at the exterior of the particle will be equal to the rate of oxygen diffusion through the pseudobrookite product layer i.e.

$$N_{F,j} = N_{S,p,O_2} \tag{1.51}$$

The oxygen partial pressure can then be obtained by solving equation (1.47)-(1.51) simultaneously, and the rate of change of core radii can be described by the following equations:

$$\frac{dr_p}{dt} = -\frac{\alpha_p k_{p,r}}{(1-\varepsilon_p)\sigma_p c_{p,o}} \left(\frac{p_{p,O_2}}{RT}\right)^a \tag{1.52}$$

$$\frac{dr_i}{dt} = -\frac{\alpha_i k_{i,r}}{(1-\varepsilon_i)\sigma_i c_{i,o}} \left(\frac{p_{i,O_2}}{RT}\right)^b \tag{1.53}$$

$$\frac{dr_{p\prime}}{dt} = -\frac{\alpha_{p\prime} k_{p,r}}{(1-\varepsilon_{p\prime})\sigma_p c_{p,o}} \left(\frac{p_{i,O_2}}{RT}\right)^a \tag{1.54}$$

The rate of interface growth would determine the rate of product layer growth and hence the rate of solids conversion, where the solids conversion is calculated using

$$X = \frac{\sigma_p\left[r_o^3 - (r_p)^3\right] + \sigma_i\left[(r_p)^3 - (r_i)^3\right] + \sigma_p\left[r_{Fe}^3 - \left(r_{p\prime}\right)^3\right]}{r_o^3} \tag{1.55}$$

The reaction rate constants were also modified from the values in Table 1 as per the following equations:

$$\begin{aligned} k_{obs} &= k_s \times sample\ surface\ area \\ &= k_s \times Number\ of\ particles \times Surface\ area\ of\ one\ particle \\ &= k_s \times \frac{Sample\ mass}{Mass\ of\ one\ particle} \times \pi d^2 \\ &= k_s \times \frac{1}{\pi/_6\, d^3 \rho} \times \pi d^2 \end{aligned}$$

where k_s is equivalent to $k_{p,r}$ and $k_{i,r}$ for $FeTiO_3$ and $Fe.TiO_2$ phases, respectively. The modified values for the rate constants are shown in Table 3.

Table 3 Reaction rate constants and reaction rate orders for $FeTiO_3$ and $Fe.TiO_2$ phases

Phase	**$FeTiO_3$**		**$Fe.TiO_2$**	
Reaction rate constant	$k_{p,r}$ at 800°C ($mol^{0.761}m^{-1.238}s^{-1}$)	6.04×10^{-3}	$k_{i,r}$ at 800°C ($mol^{0.276}m^{0.172}s^{-1}$)	1.46×10^{-2}
Reaction rate order	a	0.239	b	0.724

The model developed above is compared to the experimental data. Iron-based oxygen carrier particles of an average size of 1.5mm diameter were used for the experiments. The

oxidation experiments were conducted in a SETARAM SETSYS Evolution 1750 TGA (TGA). Only one oxygen carrier particle was used for the experiment.

In the TGA, the oxygen carrier particle was first dried at 200°C for 15 minutes under 248ml/min flow of N_2 before ramping up to the desired temperature. The gas flow was then switched to 50% H_2/N_2 to reduce the particle either completely or partially by varying the reduction times. After reducing the particle, the TGA reactor was flushed with N_2 and gas of the required O_2 concentration was then injected, by mixing air and N_2 gas streams, till complete oxidation of the particle.

Figure 9 compares results between the proposed oxidation model with experimental data in TGA at 1000° and 5% O_2. Given we don't have measurements for the morphological parameters at current stage, we manually choose porosity and α that yield reasonable results. In these two testes, the porosity for Fe_2TiO_5 and $FeTiO_3$ layer is set to be 0.005 and 0.008, respectively; α is set to be the same for different phases, and the value is chosen to be 25.

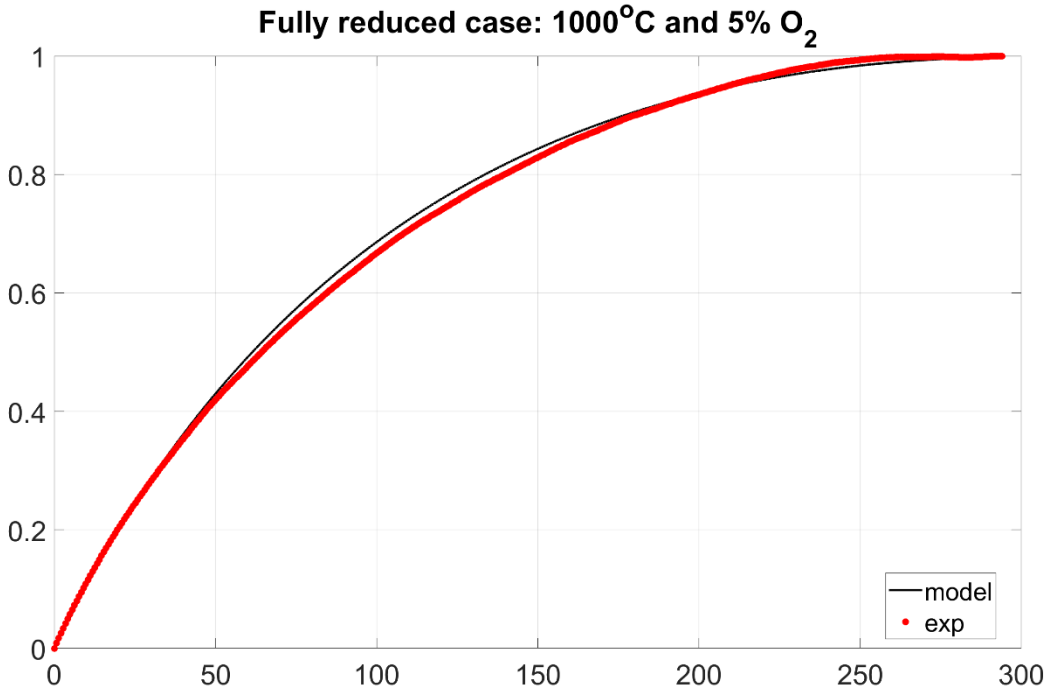

Figure 9 Comparison between TGA experimental data and model results at 1000°C and 5% O_2

Figure 10 shows the comparison between the proposed oxidation model for partially reduced particle with experimental data in TGA at 800° under 5% O_2, where the porosity for Fe_2TiO_5, $FeTiO_3$, and inner Fe_2TiO_5 layer is set to be 0.005, 0.008, and 0.01, respectively, while α is chosen to be 25 in this case.

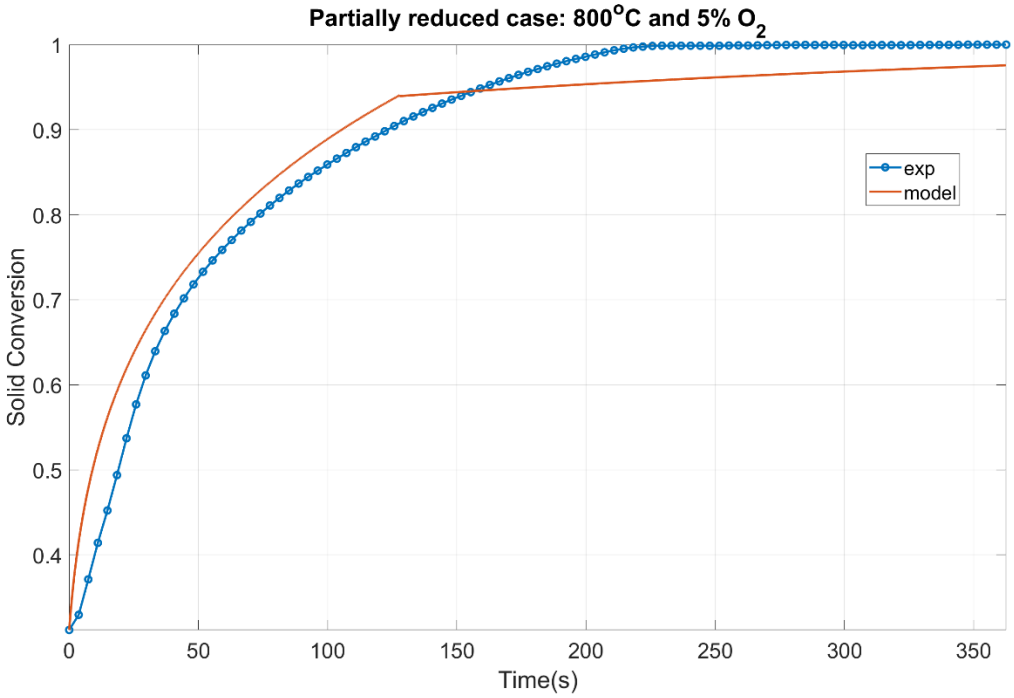

Figure 10 Comparison between TGA experimental data and model results at 800°C and 5% O_2

As shown in Figure 9 and Figure 10, the current model takes morphological effects into consideration and is able to capture the oxidation behaviors of both fully reduced and partially reduced particles. Furthermore, it is worth noting that the porosity matrix and α chosen for modeling all the two different cases are the same, which imply the current model can predict the oxidation behaviors consistently under different conditions.

The porosity of the oxygen carrier particle can be measured directly using techniques like BET, and therefore, no data fitting is required. However, measurement of α is nontrivial and a data fitting procedure might be required. One possible solution to tackle this issue is developing a correlation that relate α with the operating conditions like temperature and oxygen pressure. By doing so, the performance of the proposed model can at least be guaranteed under certain range of operating conditions. To develop such a correlation, more experimental data and model fitting will

be done in the future. Future work would involve testing the fully reduced and partially reduced models under different oxygen concentrations and temperatures.

The above model is further examined by extensive TGA experiments under different operating temperature (800, 900, and 1000 °C) and oxygen concentration (5-15%). The comparison between model and experimental results for fully reduced and partially reduced particles are summarized in Fig 11-13 and Fig 14-16, respectively. The results show that the established model can capture the oxidation kinetics accurately. The developed oxidation kinetic model can be used as a building block for the design of combustor in the chemical looping systems in the future.

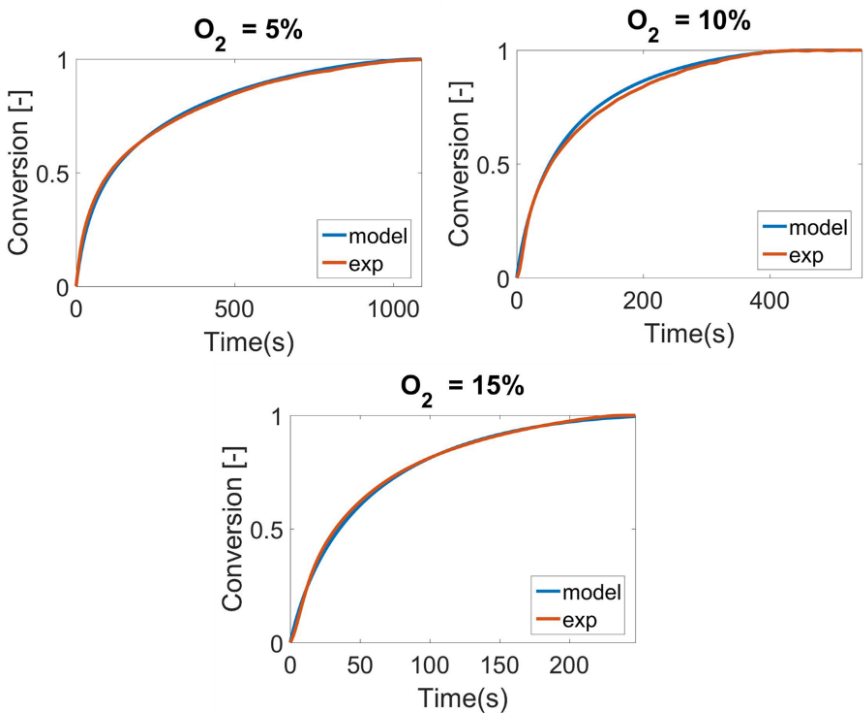

Figure 11 Comparison between TGA experimental data and model results for fully reduced particles at 800 °C under different level of oxygen concentration

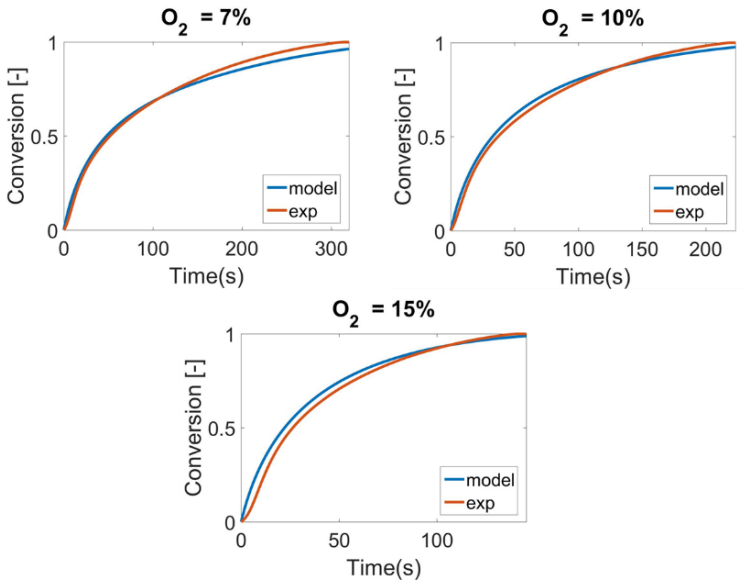

Figure 12 Comparison between TGA experimental data and model results for fully reduced particles at 900 °C under different level of oxygen concentration

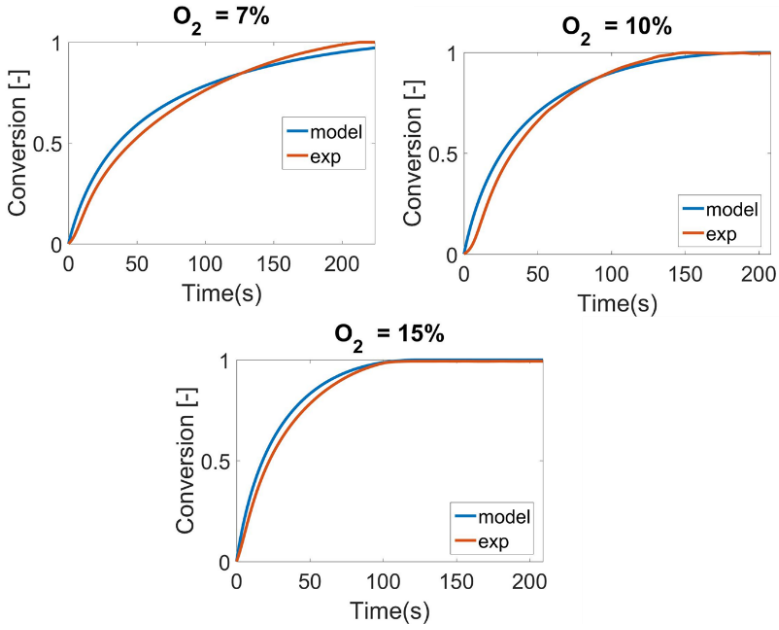

Figure 13 Comparison between TGA experimental data and model results for fully reduced particles at 1000 °C under different level of oxygen concentration

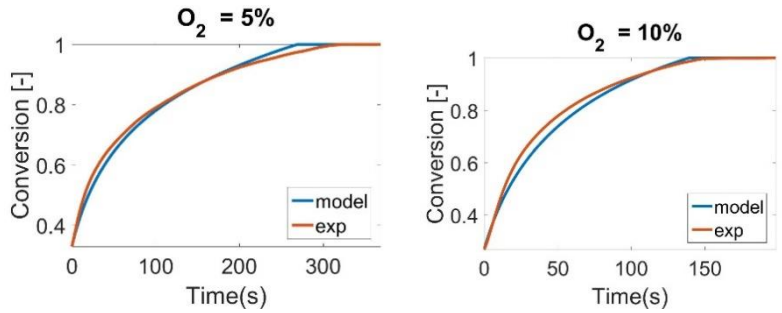

Figure 14 Comparison between TGA experimental data and model results for partially reduced particles at 800 °C under different level of oxygen concentration

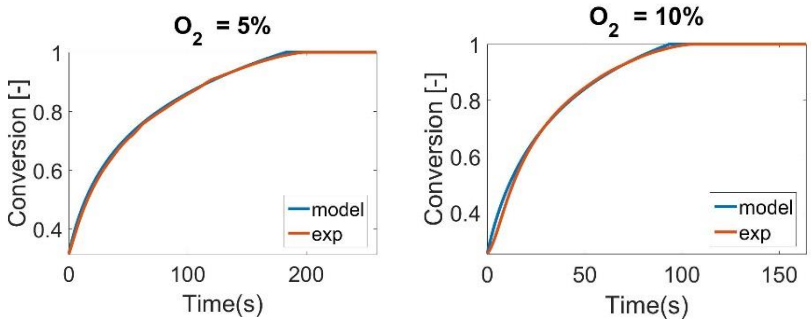

Figure 15 Comparison between TGA experimental data and model results for partially reduced particles at 900 °C under different level of oxygen concentration

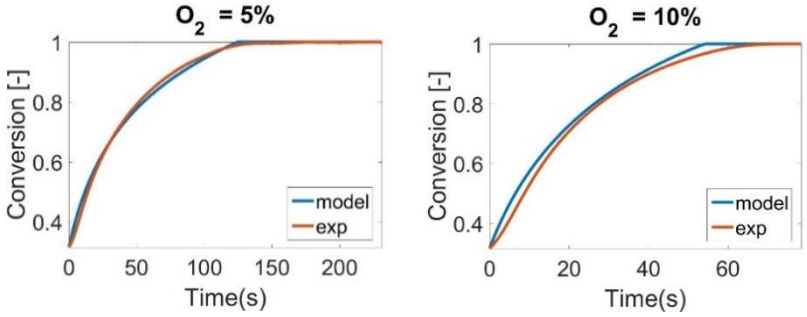

Figure 16 Comparison between TGA experimental data and model results for partially reduced particles at 1000 °C under different level of oxygen concentration

2. Chemical Looping Combustor Simulation

The properties of the granular flow in the combustor is one of the most important aspects in the design of chemical looping system. The granular flow can be modelled through several different approaches, for example, the particle-resolved direct-numerical simulations [7] (PR-DNS), the CFD-DEM method [7] and the two-fluid method (TFM) [8-12]. The PR-DNS method directly resolves the interaction between the fluid and the particles, while the CFD-DEM uses models to describe the momentum transfer between fluid and particles. Meanwhile, both PR-DNS and CFD-DEM use the Lagrangian method to trace the movement of each particle. Thus, both the PR-DNS and CFD-DEM are too time-consuming for an industrial application which involves hundreds of thousands of particles. On the other hand, the TFM method treats the particles as a continuous phase, which is governed by the equations derived from kinetic theory [13]. The TFM method is more efficient than the PR-DNS and CFD-DEM methods and is the only one candidate for extremely large-scale simulation currently.

In this report, the capability of the TFM method is validated from two different sides: the hydrodynamic properties and the heat transfer properties. The report is organized as follows. Firstly, the governing equations of the TFM method are briefly reviewed. Secondly, the result of an ECVT experiment [14] is used as a baseline to calibrate the parameters of TFM method regarding with the hydrodynamic properties. Thirdly, the heat transfer model for the TFM is calibrated based on a cold flow experiment in the fluidized bed. Then, a combustor flow is simulated through the TFM coupled with a shrinking-core model. At last, brief conclusions are made.

2.1 Governing Equations of TFM Method

The two-fluid model is a Eulerian-Eulerian model. Both the fluid and the solids as regarded as two interpenetrating continua. The control equations for the solid phased are derived from kinetic theories. Hence, properties for the particle phase are modeled in an analogous way like fluids, which include particle pressure, particle viscous force, granular temperature, etc. For the particle phase, in our simulation, only the simplest situation is considered, i.e. a monodispersed particle phase, characterized by an effective diameter and identical material properties.

The governing equations for the two-fluid model are introduced as the following equations.

$$\epsilon_g + \epsilon_s = 1 \tag{2.1}$$

$$\frac{\partial}{\partial t}\left(\epsilon_g \rho_g\right) + \nabla \cdot \left(\epsilon_g \rho_g \vec{v}_g\right) = \sum_{n=1}^{N_g} R_{gn} \tag{2.2}$$

$$\frac{\partial}{\partial t}\left(\epsilon_s \rho_s\right) + \nabla \cdot \left(\epsilon_s \rho_s \vec{v}_s\right) = \sum_{n=1}^{N_s} R_{sn}, \tag{2.3}$$

$$\frac{\partial \epsilon_g \rho_g \vec{v}_g}{\partial t} + \nabla \cdot \left(\epsilon_g \rho_g \vec{v}_g \vec{v}_g\right) = \nabla \cdot \bar{\bar{S}}_g + \epsilon_g \rho_g \vec{g} - \vec{I}_{gs} \tag{2.4}$$

$$\frac{\partial \epsilon_s \rho_s \vec{v}_s}{\partial t} + \nabla \cdot \left(\epsilon_s \rho_s \vec{v}_s \vec{v}_s\right) = \nabla \cdot \bar{\bar{S}}_s + \epsilon_s \rho_s \vec{g} + \vec{I}_{gs} \tag{2.5}$$

$$\epsilon_g \rho_g C_{pg} \left(\frac{\partial T_g}{\partial t} + \vec{v}_g \cdot \nabla T_g\right) = -\nabla \cdot \vec{q}_g - H_g - \Delta H_{rg} + H_{wall}\left(T_{wall} - T_g\right) \tag{2.6}$$

$$\epsilon_s \rho_s C_{ps} \left(\frac{\partial T_s}{\partial t} + \vec{v}_s \cdot \nabla T_s\right) = -\nabla \cdot \vec{q}_s + H_g - \Delta H_{rs} \tag{2.7}$$

$$\frac{3}{2}\left(\frac{\partial}{\partial t}\epsilon_s \rho_s \Theta + \nabla \cdot \epsilon_s \rho_s \Theta_s \vec{v}_s\right) = \left[\bar{\bar{S}}_s : \nabla \vec{v}_s - \nabla \cdot \vec{q}_\Theta - \gamma_\Theta + \phi_g\right], \tag{2.8}$$

where the subscript $\cdot_g$ stands for the variable of gas phase and the subscript $\cdot_s$ stands for the variable of solid phase. In Eq. (1-8), t is time, ϵ is the volume fraction, R is the source term for mass equation, ρ is density, $\vec{v}_s$ is velocity, $\bar{\bar{S}}$ is the stress tensor, $\vec{I}$ is the interaction force between gas and solid phases, $\vec{g}$ is the gravity, C_p is the specific heat coefficient with constant pressure, T is temperature, $\vec{q}$ is the conductive heat flux and ΔH_r is the heat of reaction. H_g is the heat exchange between gas and solid phase, Θ is the granular temperature, γ_Θ is the rate of granular energy dissipation due to the inelastic collision, and $\vec{q}_\Theta$ is the diffusive flux of granular energy. The term ϕ_g accounts for the granular energy transfer between the gas phase and solid phase.

The gas phase is treated as a perfect gas with state equation

$$P_g = \frac{\rho_g R T_g}{M_w},$$

where $R = 8.314\, J/(mol \cdot K)$, and M_w is the molar mass of the gas.

In Eq. (4-5), if we only consider the buoyancy, the drag force and the momentum transfer due to the mass transfer, $\vec{I}_{gs}$ can be written as

$$\vec{I}_{gs} = -\epsilon_s \nabla P_{\mathrm{g}} - F_{gs} \cdot \left(\vec{v}_s - \vec{v}_g\right) + R_{gs}\left[\xi_0 \vec{v}_s + \overline{\xi}_0 \vec{v}_g\right] \tag{2.9}$$

The first term of Eq. (9) describes the buoyancy force, the second term denotes the drag force and the third term is the momentum transfer due to the mass transfer. R_{gs} is the mass transfer rate from gas to solid phase, and $\xi_0 = 1 - \overline{\xi}_0$ is a switch function defined as

$$\xi_0 = \begin{cases} 0 & R_{gs} \geq 0 \\ 1 & R_{gs} < 0 \end{cases} \tag{2.10}$$

The drag force expression in our simulation follows the formula of Syamlal and O'Brien[15], and the drag force correlation F_{gs} is expressed as a function of terminal velocity V_{rs} as

$$F_{\mathrm{gs}} = \frac{3\epsilon_s \epsilon_g \rho_g}{4 V_{rs}^2 d_{ps}} C_{Ds} \left|\vec{v}_s - \vec{v}_g\right| \tag{2.11}$$

where d_{ps} is the diameter for the particle. And V_{rs} is the terminal velocity, approximated by

$$V_{rs} = 0.5\left(A - 0.06\mathrm{Re}_s + \sqrt{(0.06\mathrm{Re}_s^2) + 0.12\mathrm{Re}_s(2B - A) + A^2}\right) \tag{2.12}$$

where

$$A = \epsilon_g^{4.14}, \tag{2.13}$$

$$B = \begin{cases} 0.8\epsilon_g^{1.28} & if \epsilon_g \leq 0.85 \\ \epsilon_g^{2.65} & if \epsilon_g > 0.85 \end{cases} \tag{2.14}$$

and the particle Reynold number Re_s is expressed as

$$\mathrm{Re}_{\mathrm{s}} = \frac{d_s \left|\vec{v}_s - \vec{v}_g\right| \rho_g}{\mu_g} \tag{2.15}$$

C_{Ds} is the single-sphere drag function.

$$C_{Ds} = \left(0.63 + \frac{4.8}{\sqrt{\frac{\mathrm{Re}_s}{V_{rs}}}}\right)^2 \tag{2.16}$$

The stress tensor for the gas and solid phases are expressed as

$$\bar{\bar{S}}_g = -P_g \bar{\bar{I}} + \bar{\bar{\tau}}_g \tag{2.17}$$

$$\bar{\bar{S}}_s = -P_s \bar{\bar{I}} + \bar{\bar{\tau}}_s \tag{2.18}$$

respectively, where P_g and P_s are gas and solid pressure respectively, $\bar{\bar{I}}$ is the identity tensor and $\bar{\bar{\tau}}_g$ and $\bar{\bar{\tau}}_s$ are the viscous stress tensor.

For the Newtonian fluid, $\bar{\bar{\tau}}_g$ is expressed as

$$\bar{\bar{\tau}}_g = 2\epsilon_g \mu_g \bar{\bar{D}}_g + \epsilon_g \left(\lambda_g - \frac{2}{3}\mu_g\right) tr(\bar{\bar{D}}_g)\bar{\bar{I}} \tag{2.19}$$

where μ_g and λ_g are the first and second viscosity coefficient, respectively. And $\bar{\bar{D}}_g = \frac{1}{2}\left[\nabla\vec{v}_g + \left(\vec{v}_g\nabla\right)^T\right]$.

As to the solid phase, granular flow can be classified into two different regimes: a plastic flow, in which the stresses arise because of Coulomb friction and a viscous flow, in which stress arises from of the collisional or translational transfer of momentum. A switch quantity of ϵ_g^* can be introduced to combine these two theories, as shown in Eq. (20).

$$\bar{\bar{S}}_{sm} = \begin{cases} -P_{sm}^p \bar{\bar{I}} + \bar{\bar{\tau}}_{sm}^p & if \epsilon_g < \epsilon_g^* \\ -P_{sm}^v \bar{\bar{I}} + \bar{\bar{\tau}}_{sm}^v & if \epsilon_g \geq \epsilon_g^* \end{cases} \tag{2.20}$$

In our simulation, Lun's kinetic model[16] was used for the viscous flow regimes and Schaeffer's frictional model[17] was used for the plastic flow regimes.

The heat flux for the gas phase is determined by:

$$\vec{q}_g = -\epsilon_g \kappa_g \nabla T_{\mathrm{g}} \tag{2.21}$$

where ϵ_g is the volume fraction of the gas, κ_g the heat conductivity coefficient, and T_{g} the temperature for the gas phase. κ_g is determined by Sutherland's law and Prandtl number for the air:

$$\mu_g = \mu_{ref}\left(\frac{T}{T_{ref}}\right)^{1.5}\frac{T_{ref}+S}{T+S} \tag{2.22}$$

where $\mu_{ref} = 1.716 \times 10^{-5}\mathrm{kg/(m \cdot s)}$, $T_{ref} = 273.15K$ and $S = 110.4K$.

$$\mathrm{Pr}_g = \frac{\mu_g C_{p,g}}{\kappa_g} \tag{2.23}$$

And

$$C_{p,g} = 1003.4\frac{J}{kg \cdot K} \tag{2.24}$$

is the specific heat coefficient for the air and

$$\mathrm{Pr}_g = 0.74 \tag{2.25}$$

The heat flux for the solid phase is determined by:

$$\vec{q}_s = -\epsilon_s \kappa_s \nabla T_s, \tag{2.26}$$

where ϵ_s, κ_s and T_s are the same meaning for the gas phase and

$$\frac{\kappa_s}{\kappa_g} = \frac{\phi_k R_k + (1-\phi_k)\lambda_r}{\sqrt{(1-\epsilon_g)}} \tag{2.27}$$

where

$$\lambda_r = -\frac{2}{1-\frac{b}{R_k}}\left[\frac{(R_k-1)\frac{b}{R_k}}{\left(1-\frac{b}{R_k}\right)^2}\ln\left(\frac{b}{R_k}\right) + \frac{b-1}{1-\frac{b}{R_k}} + \frac{b+1}{2}\right], \tag{2.28}$$

$$R_k = \frac{\kappa_p}{\kappa_g}, \tag{2.29}$$

and for spherical particles

$$b = 1.25\left(\frac{1-\epsilon_g}{\epsilon_g}\right)^{\frac{10}{9}}, \tag{2.30}$$

and ϕ_k is the contact are fraction chosen as $\phi_k = 7.26 \times 10^{-3}$.

For a surface ∂S, the heat flow in the normal direction can be obtained as

$$H = \int_{\partial S} (\vec{q}_g + \vec{q}_s) \cdot \vec{n}\, \mathrm{d}s \tag{2.31}$$

Then the heat convection coefficient can be defined as:

$$h = \frac{H}{S(T_{wall} - T_0)}, \tag{2.32}$$

where S is the surface area of the heat exchanger.

2.2 Hydrodynamic Properties

In the fluidized bed, the size of the bubbles will grow due to the rapid coalescence of the bubbles as they rise through the bed. If the height of the bed is high enough, the size of the bubbles will increase eventually to the size of the bed diameter, and then the slug occurs. The slugging

phenomena will affect the mixture of the gas and particles in the combustor. Stewart and Davidson[18] described two different axisymmetric forms of slugging fluidized bed based on the specific particle size, i.e. round-nosed slugs and square-nosed slugs.

In this section, we focused on the coarse particles in a bench-scale fluidized bed, where square-nosed slugs happen. The baseline of the simulation is a three-dimensional ECVT result by Wang.[14] Both MFIX and Ansys Fluent solver were used for the simulation.

2.2.1 Effects of Boundary Conditions

Computational setup

The physical model refers to a 2-D slugging fluidized bed as shown in Fig. 17(a). The width of the bed is 0.0762 m (3 inches) and the height is 2.7 m. The bed of 2.7 m is high enough to avoid the loss of particles in the simulations. And most of the gas-solid flow structures locate under the height of 1 m. Thus, un-uniform Cartesian grids are used in the simulations, as shown in Fig. 17(b), where stretched grids are used along the height direction.

According to experiments of Wang [14], the initial bed height is set to be 0.4 m with a gas volume fraction of 0.37, which is also the value of ϵ_g^* . The particle composed of Fe_2O_3 and TiO_2 has a diameter of 0.0015m and a density of 2500 kg/m^3. The restitution coefficient between particles was set to be 0.9 and the angle of frictional angle is set be 21.5 degree.[19] The air with temperature of 300 Celsius and a uniform velocity is introduced through the bottom of the bed. With the increase of the inlet air velocity, the particles in the bed will be fluidized. With the increase of inflow air velocity, the size of air bubbles in bed will increase and eventually the slugging phenomena occur.

For the wall boundaries, non-slip boundary condition is applied for the gas-phase.

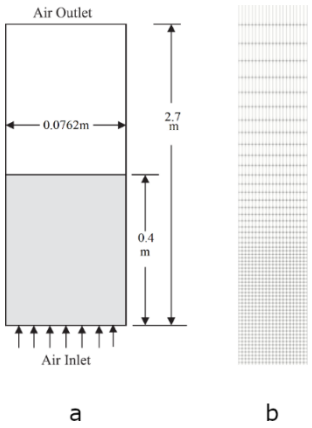

Figure 17 Illustration of the physical model (b) Ununiform Cartesian grids

For the solid phase, partial-slip boundary conditions are applied:

$$v_{s,w} = -A\frac{\partial v_{s,w}}{\partial n}, \tag{2.33}$$

with the subscript 's' denotes the solid phase, and 'w' denotes the wall. If $A \to \infty$, Eq. (33) degrades to a non-penetration boundary condition; if $A \to 0$, Eq. (33) becomes a Dirichlet boundary condition. The smaller the value of A is, the greater the stress forces are applied to the solid phase by the wall, which in turn results into a smaller slugging velocity.

In MFIX and Fluent. A is modelled using Johnson and Jackson [20] partial slip wall boundary condition as

$$A = \frac{6\mu_s\epsilon_{s,max}}{\sqrt{3}\pi\phi\rho_s\epsilon_s g_{0,ss}\sqrt{\Theta}}, \tag{2.34}$$

where $\epsilon_{s,max}$ is the maximum solid volume fraction for random packed particles and ϕ is the specularity coefficient.

In MFIX, Li 's method is used to calculate ϕ, where ϕ is a function of particle-wall restitution coefficient and particle-wall frictional coefficient.[21] The particle-wall restitution coefficient is set to be 0.9 as the same as the particle-particle restitution coefficient. However, in MFIX, the Jackson-Johnson boundary conditions cannot be used together with curved boundaries. Thus, when involved curved boundaries, A has to be set as a constant value in MFIX.

In Fluent, ϕ is treated as a constant value. The Johnson and Jackson boundary conditions can be applied whether or not the boundary is curved.

The superficial velocities under the experimental conditions with inflow temperature of 300^{o}C are 1.39, 1.5, 1.63, 1.77, 1.9, 2.01, 2.12, 2.23, 2.34, 2.45, 2.56, 2.67, 2.79, 2.9, 2.96, 3.07

m/s. Under each superficial velocity, through the signal phase delays obtained by the ECVT sensors located in different positions, the bubble/slug rising velocity can be obtained [14].

For the TFM simulation, according to the result of Goldschmidt[11], Bokkers[12] and Fullmer [22], to obtain a quantitative agreement between the TFM result and the CFD-DEM result for the Geldart D particles, the grid size should be the order of 2-4 particle diameters at moderate to mean concentration (where the particle volume fraction is about 0.25). Thus, for the following simulation, three gradually refined grids are used, which include 5×254 cells, 20×230 cells and 40×460 cells. For the mesh of 5×254 cells, the grids are uniform in both width and height direction and the grid size is almost 10 times of particle diameters. For the latter two sets of meshes, the grids are uniform along the width and are stretched along the height, and is approximately uniform under the height of 1m, where the grid size is approximately 2.5 and 1.25 times the particle diameters, respectively.

MFIX Results for the grid size of 2.5 particle diameters

Firstly, the influence of the particle-wall frictional coefficient is investigated using the coarse mesh.

In MFIX, the particle-wall frictional coefficient is either represented by the tangential of the particle-wall frictional angle denoted as β or directly modelled through a constant value of A in Eq. (2.33). For the MFIX simulation, three different particle-wall frictional angle were used in the simulation, i.e., $\beta = 2°, 6°, 11.31°$. And five different values of constant A are chosen, which are *1/75, 1/50, 1/30, 1/10,* to $+\infty$.

In Fluent, the particle-wall friction coefficient is represented by the specularity coefficient ϕ in Eq. (34) and $\phi = 0.001$ is used.

The end time for each simulation is 25s, which is long enough to eliminate the influence of initial conditions. Here, we select the superficial velocities for the simulation as 1.39, 1.63, 1.90, 2.12, 2.34, 2.56, 2.79, 2.96 (m/s). The result of MFIX simulation with different $\beta = 2°, 6°, 11.31°$ at time t =15s are shown in Fig. 18. As shown in Fig. 18, bubbles arise in the bottom of the bed and increase to slugging structures with the rise of bubbles.

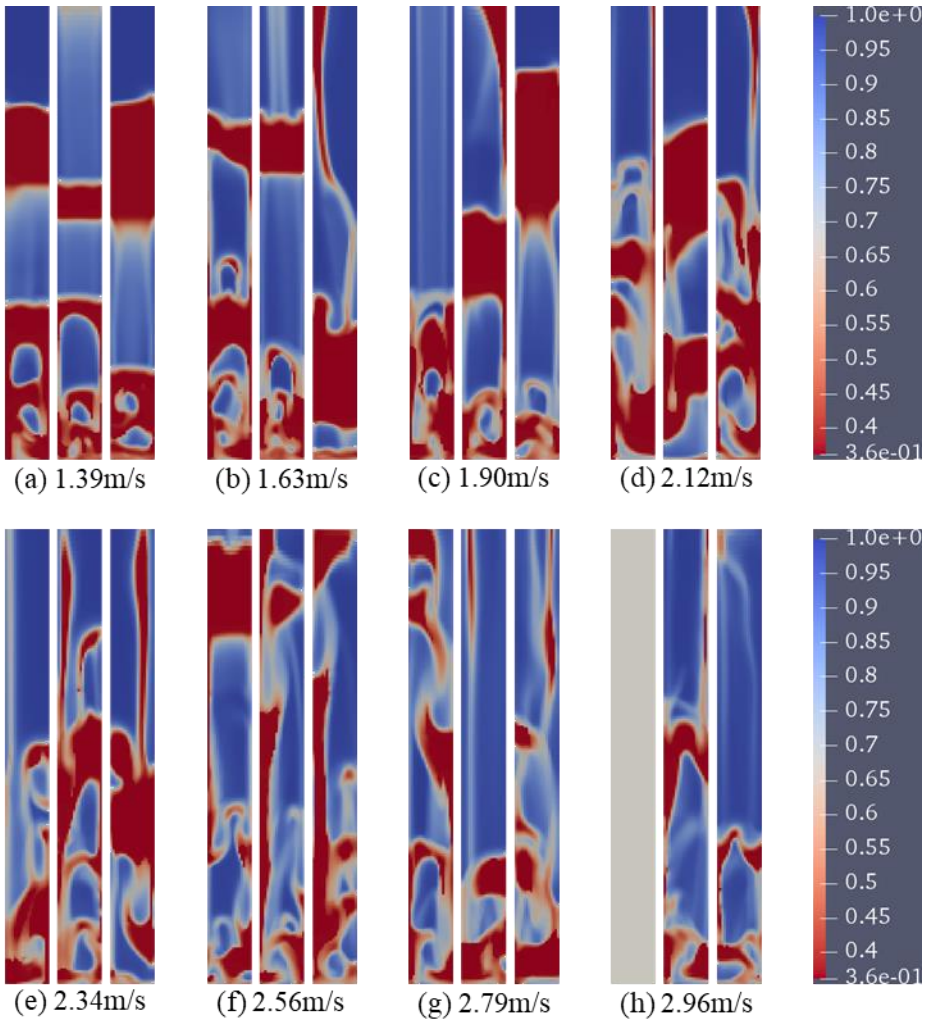

Figure 18 The gas volume fraction under different superficial velocity at time t=15s. Under each subfigure, the particle-wall frictional angle is $\boldsymbol{\beta = 2°, 6°, 11.31°}$ from left to right

In Wang's experiments,[14] signals in the up and bottom sides (height=0.4m and height=0.2m) of ECVT sensors were used to calculate the bubble/slug rising velocities. For the simulation, a cross section located in the height of 0.3m are used to monitor the slugs. When the averaged solid volume fraction over this cross section reaches 0.60, it is considered that the slug forms and then the particle velocity is used to approximate the slug rising velocity. Simulation results of the last 15 seconds are used to calculate this slug rising velocity.

Figure 19 is the obtained averaged slug rising velocities with different particle-wall frictional angle β. As shown in this figure, with the increasing of the particle-wall frictional angle,

the slug rising velocity decreases. Over the three different values of particle-wall frictional angle, results of $\beta = 6°$ conincide best with the experimental data of Wang.[14]

Figure 20 shows the averaged slug rising velocities with different constant value of A. As expected, with the increasing of A, the wall frictional forces reduce and the slug rising velocities increase. Figure 21 shows the approximately best value of A = 1/40.

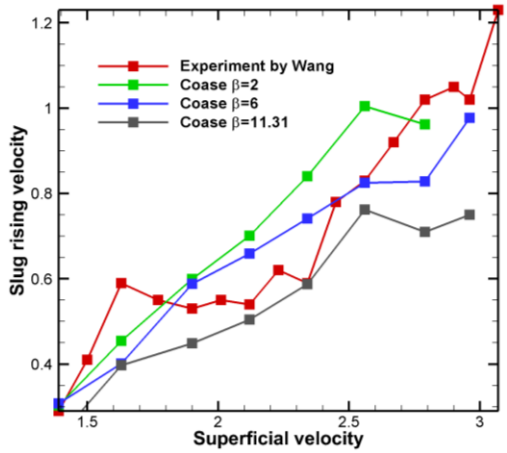

Figure 19 The averaged slug rising velocity over cross section height = 0.3 m of MFIX simulation with different particle-wall frictional angle β

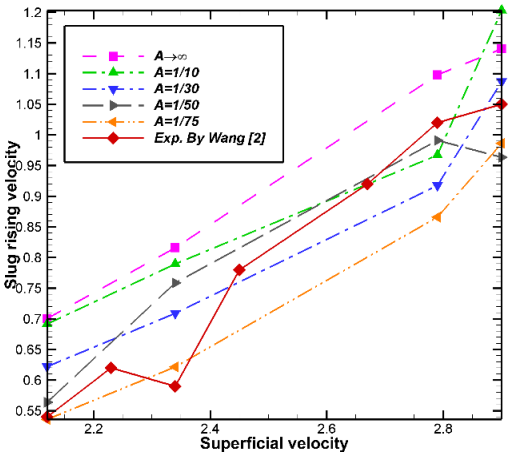

Figure 20 The averaged slug rising velocity over cross section height = 0.3m of MFIX simulation with different A

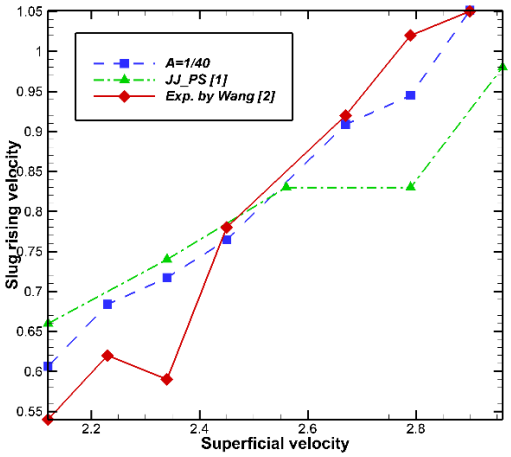

Figure 21 The averaged slug rising velocity over cross section height = 0.3m of MFIX simulation with A = 1/40

MFIX Results for grid size of 1.25 particle diameters

In this subsection, mesh with 40×460 cells is used to check the grid convergence of the results obtained by the coarse grids. Figure 22 is the gas volume fraction at time t=20s under different superficial velocities. Also, the slug rising velocity (approximated by particle velocity) over cross section of height = 0.3m are shown in Fig. 23. When the mesh is refined, the obtained slug rising velocities remain almost unchanged compared with the results of coarse mesh and fit well with the experimental data. It can be concluded that grid size of order 3 particle diameters is fine enough to capture the slug rising phenomena for the Geldart D particles.

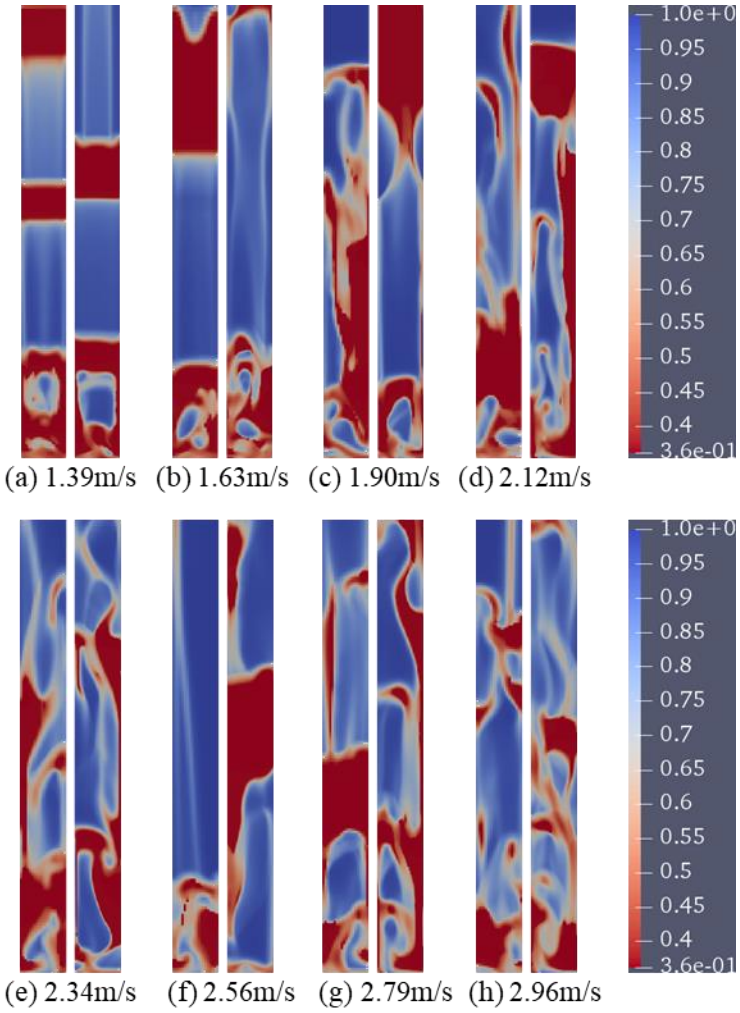

Figure 22 The gas volume fraction under different superficial velocity at time t=20s with particle-wall frictional angle $\beta = 6°$. Under each subfigure, coarse and fine mesh are used from left to right

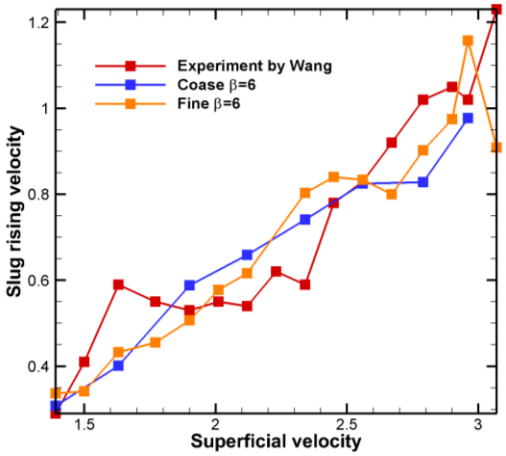

Figure 23 The averaged slug rising velocity over cross section height = 0.3m with particle-wall frictional angle of $\boldsymbol{\beta = 6°}$ on coarse and fine grids

Fluent Results for grid size of 10 particle diameters

In the previous section, the results of MFIX under different superficial velocities are obtained under grid size of 2.5 and 1.25 particle diameters. It shows that the grid size of 2.5 particle diameters is fine enough to capture the slugging rising velocities consistent with the experimental data.

However, for a large-scale simulation, the grid size of 2.5 particle diameter is still too small and resultant stable time forward step size will be approximately 0.0001s, which makes the simulation very inefficient.

Thus, in this section, the validity of mesh with grid size 10 particle diameters was checked using Ansys Fluent. The pre-calibrated specularity coefficient is $\phi = 0.001$, which makes the slugging rising velocities correspond very well with the experimental results for the grid size of order 2.5 particle diameters, as shown in Fig. 24.

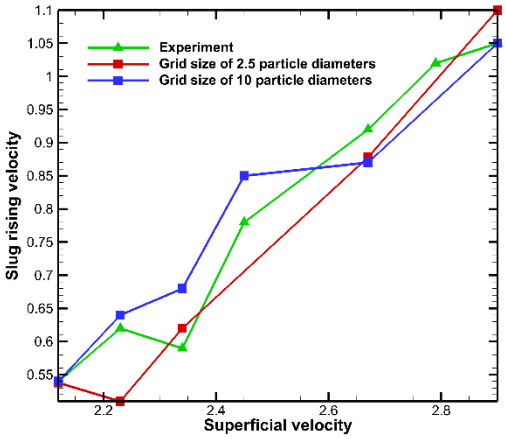

Figure 24 The averaged slug rising velocity over cross section of height = 0.3m by Fluent simulation with specularity coefficient 0.001

Figure 25 shows the snapshots of the slugging fluidized bed for the two sets of mesh with different grid size. Although the result of mesh with grid size 10 particle diameters is not as detailed as the result using mesh with grid size 2.5 particle diameters, their macro structures are almost the same.

Additionally, the slug rising velocities for the two different set of meshes are plotted in Fig. 8, which shows that slug rising velocities remain almost unchanged when the grid size is coarsened to 10 particle diameters. From this point of view, the grid size of 10 particle diameters is also fine enough to predict the slugging phenomena.

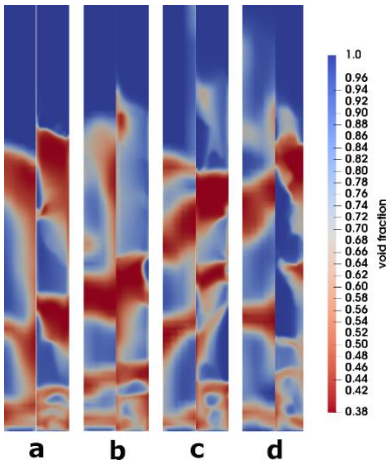

Figure 25 Snapshots of Ansys Fluent results for different superficial velocities. Left figure for each column: grid size of 10 particle diameters. Right figure for each column: grid size of 2.5 particle diameters. (a) 2.12 m/s (b) 2.34 m/s (c) 2.79 m/s (d) 2.90 m/s

2.2.2 Effects of the Bed Diameter

With the rising of gas phase, bubbles of different size coalesce together and will increase eventually to the size of the bed diameter if the bed is high enough. Thus, for a certain bed height, with the increasing of bed diameter, the slugging phenomenon will disappear, and the bed becomes fully fluidized.

In this section, the effect of the diameter will be verified using MFIX. The initial bed height and particle properties are the same with last section, except that the bed diameter varies from 3 inches, 6 inches to 12 inches. The wall boundaries are defined by the non-slip boundary conditions for the gas phase and partial slip boundary conditions for the solid phase of Eq. (33) with *A = 1/40*.

Two superficial gas velocities are considered, i.e. $v_g = 2.34m/s$ and $v_g = 2.79m/s$. The end time for the simulation is 25s. And the snapshots in a certain time point among the last 10s are shown in Fig. 26. When D = 3 inches, slugging structures can be captured obviously in the bed. If the diameter extended to D = 6 inches or 12 inches, slugging structures become less obvious and the bed turns to be a bubbling one.

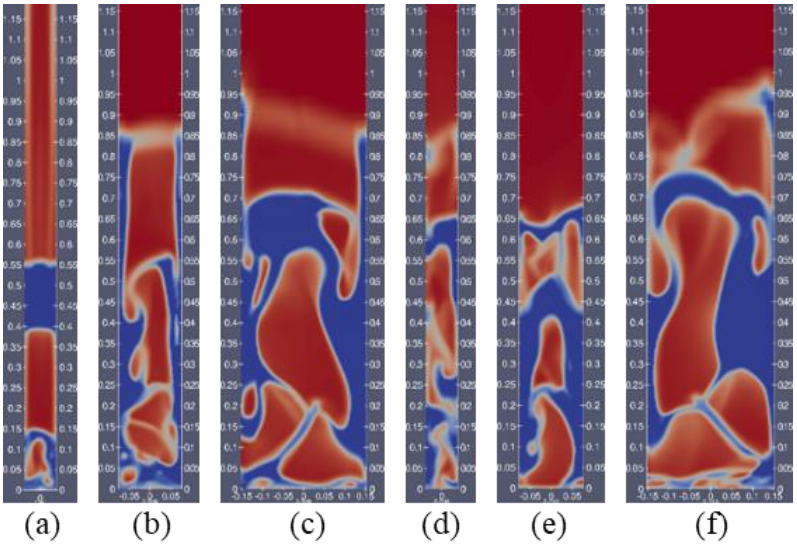

Figure 26 Snapshots of the void fraction for the bed with different diameters and superficial velocities(a)-(c): $v_g = 2.34m/s$; (d)-(f): $v_g = 2.79m/s$. (a),(d): D = 3 inches; (b),(e): D = 6 inches; (c),(f):D = 12 inches

To compare the slugging or bubbling structures under different bed diameters, the average void fraction in cross-section of height = 0.3m are plotted over time, shown as in Fig. 11 and 12.

As shown in Fig. 27-28, when D = 3 inches, large bubbles, where the average void fraction $\epsilon_g \rightarrow 1$ or slugging structures, where $\epsilon_g \rightarrow 0.37$ can be watched. When D = 6 inches, still some large bubbles or slugging structures exist, but become obviously less. When D = 12 inches, the bed becomes a bubbling one, and the time evolution of the void fraction becomes very high-frequency.

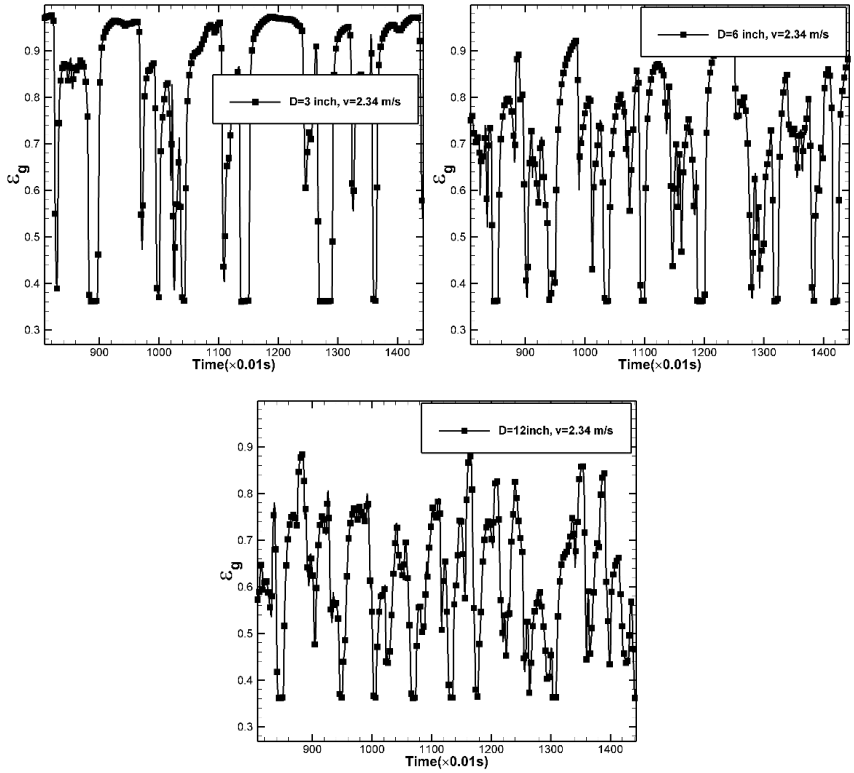

Figure 27 Average void fraction over cross-section of height = 0.3m. $v_g = 2.34 m/s$

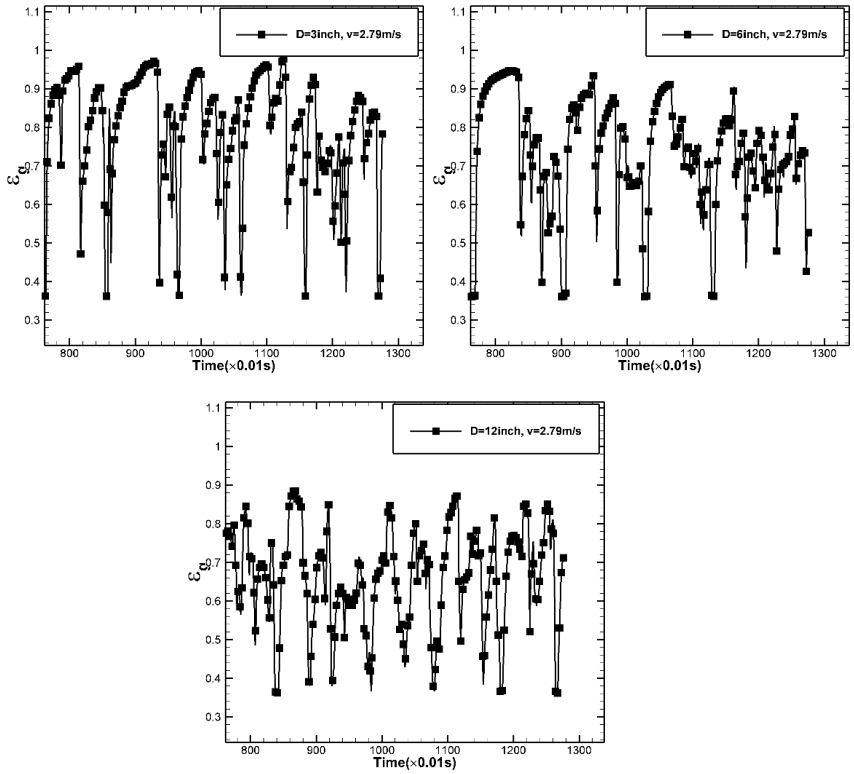

Figure 28 Average void fraction over cross-section of height = 0.3m. $v_g = 2.79 m/s$

2.2.3 Fluidized Bed with Heat Exchanger

In this section, the simplified 2-D physical model illustrated as in Fig. 29 are considered to check the effect of heat exchanger networks in the fluidized bed. The tubes of the exchanger are simplified as several columns of circles in 2-D cases and their diameter is 2.5 inches. The distance between different columns is *b*. The initial bed height is still 0.4 m (15.748 inches). Other geometrical parameters are shown in Fig. 29.

A mass inlet boundary condition is applied at the bottom of the bed while a pressure outlet boundary condition is applied at the upper side. The left and right sides are set to be periodic. At the surface of exchanger, a partial slip wall boundary condition with $A = 1/40$ shown as in Eq. (2.33) is applied for the solid phase and non-slip boundary condition applied for the gas phase.

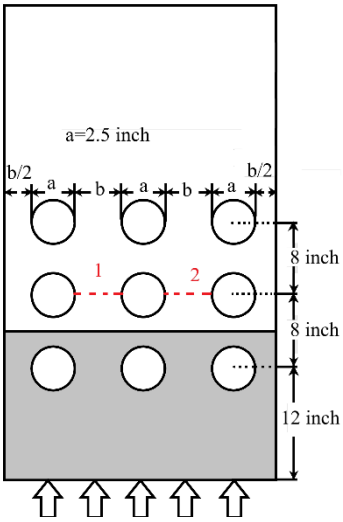

Figure 29 Illustration of the simplified 2-D physical model with heat exchanger

In the former sections of this report, the very basic fluidized bed without any imbedded objects are discussed. The wall effect and the bed diameter play important roles in the development of slugging structures. Here, the channels between different columns of heat exchangers can be regarded as these basic fluidized beds. The difference here is that these channels are not fully confined by wall surfaces since space exists between exchanger tubes of different height.

The simulations run at least for 10s for the bed to be fully developed. And the snapshots of void fraction at a certain time point for *b* varies from 3 inches, 6 inches to 12 inches with superficial velocities of $v_g = 2.34m/s$ and $v_g = 2.79m/s$ are shown as in Fig. 30 and 31.

It can be shown as in Fig. 30 and 31, bubbles and solid particles can go through the space between heat exchanger tubes. For the heat exchanger located as in Fig. 29, the space is enough even for channel of width 3 inches to be without slugging structures.

The time evolution of the void fraction at the cross-section 1 and 2 shown as the red dashed line in Fig. 29 are plotted in Fig. 32-34.

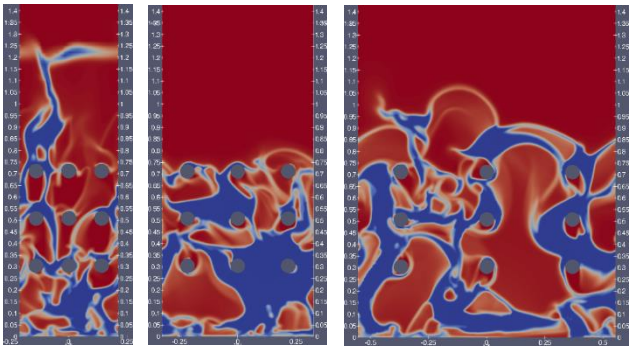

Figure 30 Snapshots of the void fraction for b = 3, 6 and 12 inches with $v_g = 2.34 m/s$

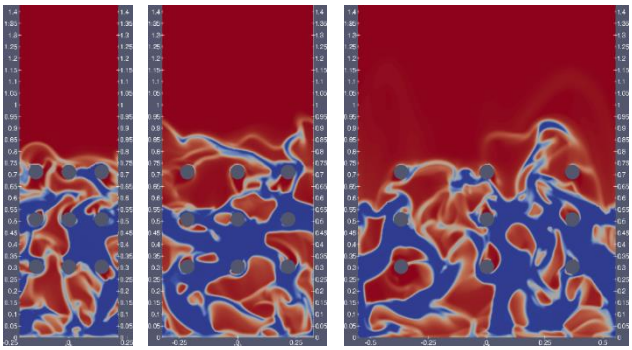

Figure 31 Snapshots of the void fraction for b = 3, 6 and 12 inches with $v_g = 2.79 m/s$

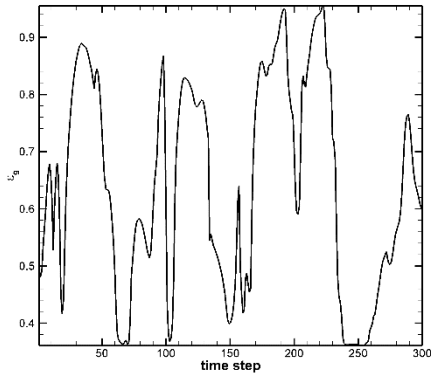

(a)cross-section 1, $v_g = 2.34m/s$

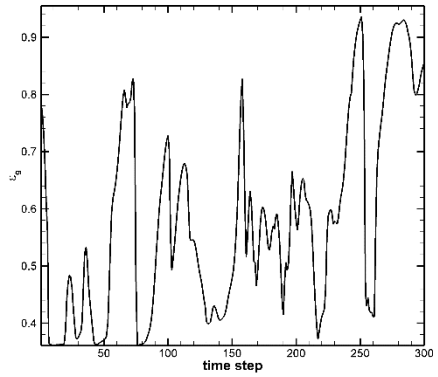

(b) cross-section 2, $v_g = 2.34m/s$

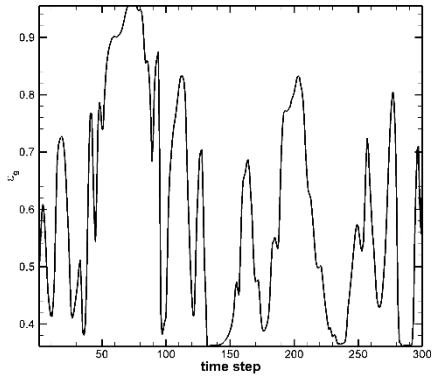

(c)cross-section 1, $v_g = 2.79m/s$

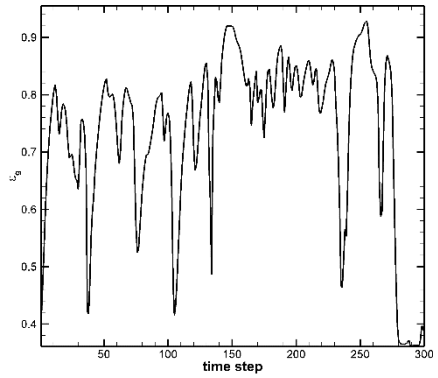

(d) cross-section 2, $v_g = 2.79m/s$

Figure 32 Void fraction evolution of fluidized bed with imbedded heat exchanger and *b* = 3 inches

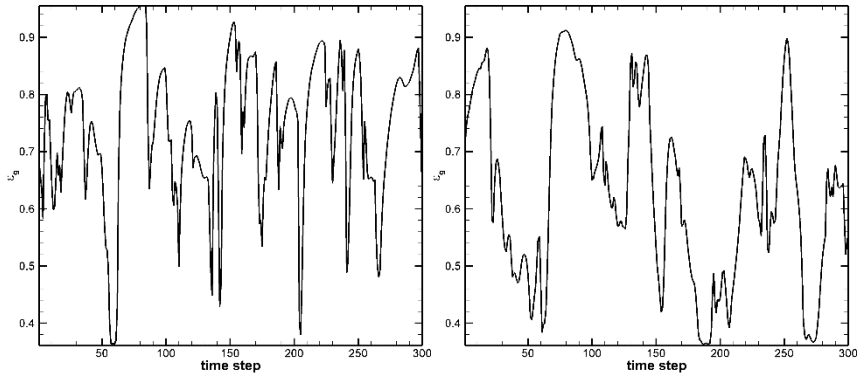

(a)cross-section 1, $v_g = 2.34m/s$ (b) cross-section 2, $v_g = 2.34m/s$

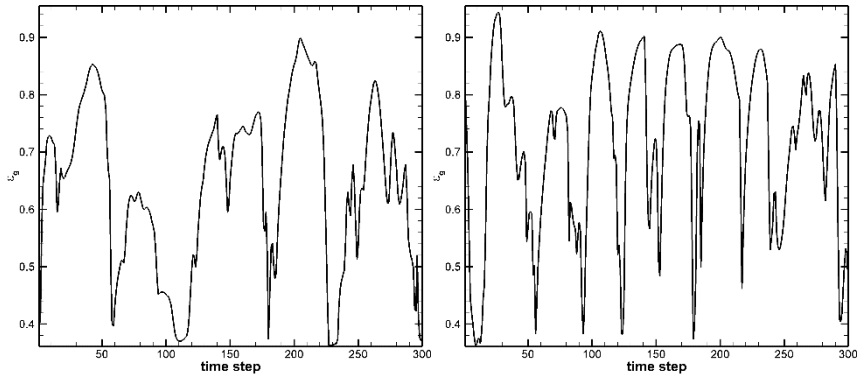

(c)cross-section 1, $v_g = 2.79m/s$ (d) cross-section 2, $v_g = 2.79m/s$

Figure 33 Void fraction evolution of fluidized bed with imbedded heat exchanger and *b* = 6 inches

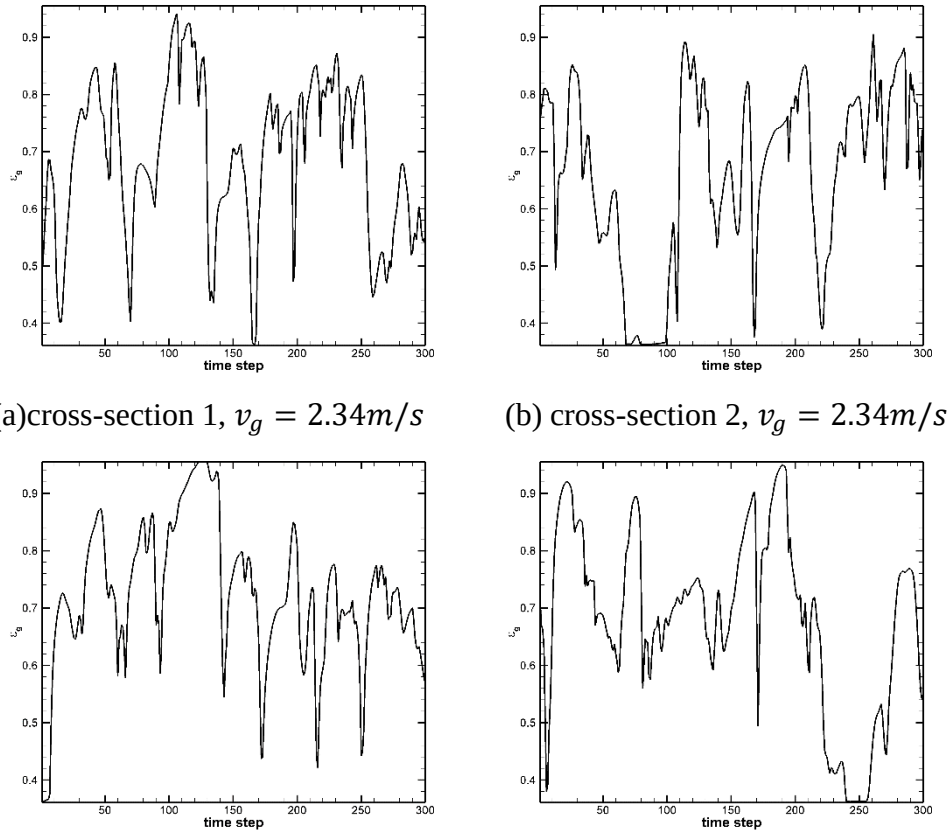

(a)cross-section 1, $v_g = 2.34m/s$ (b) cross-section 2, $v_g = 2.34m/s$

(c)cross-section 1, $v_g = 2.79m/s$ (d) cross-section 2, $v_g = 2.79m/s$

Figure 34 Void fraction evolution of fluidized bed with imbedded heat exchanger and b = 12 inches

2.2.4 Simulation for Large-Scale Combustor with Filtered TFM

For large scale apparatus, due to the constraints of computational resources, the filtered model[23,24] must be used to capture the evolution of small-scale properties while maintaining the low computational consumptions in relatively coarse grids. The filtered model proposed by Milioli[23] was used to simulation the gas-solid fluid in a combustor shown as in Fig. 19. The detailed model can be found in the reference and will not be explained here.

The scale of the combustor is shown as in Fig. 19. And three columns of heat exchangers are placed along the y-direction. Two simulations with and without heat exchangers are compared. The temperature of the simulation is 1373.15 K. The inlet gas velocity from the bottom is 4.2 m/s, which is about 5 times of minimum fluidized gas velocity. The solid inlet velocity from the right is 0.15 m/s. The wall boundary conditions are set with a transfer coefficient of A = 1/40 (m) shown as in Fig. 5. The grid size is about 46 times of particle diameter.

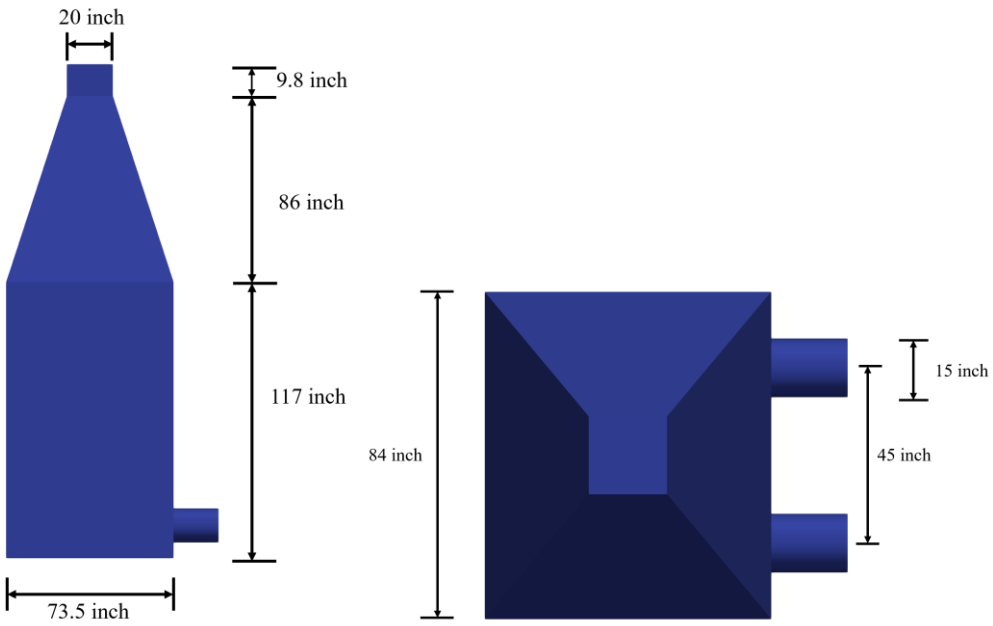

Figure 35 Illustration of the large-scale combustor model. Left: From view; right: top view

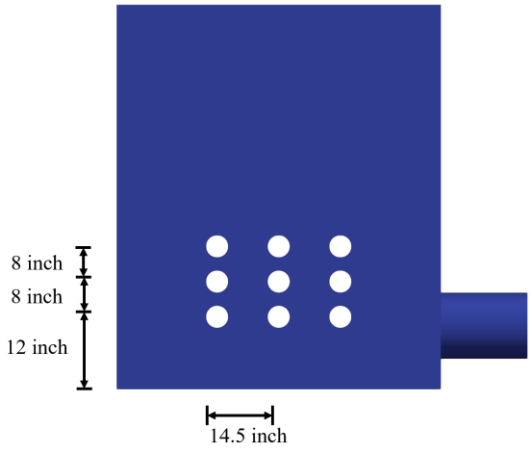

Figure 36 Illustration of the heat exchangers' location in the combustor, view from the front

After long enough time to reach the steady state, the fluid field is averaged over 50 seconds. The streamlines of the averaged field for the combustor without heat exchanger are shown in Fig. 37 and 38. For ease of presentation, the original points are defined in the bottom center of the combustor. As shown, there are two main vortex rings for the solid phase in the combustor. For one of the two vortices, the solid falls along the wall. For the other one, the solid falls along the centerline, i.e., the line defined by x = 0 and y = 0.

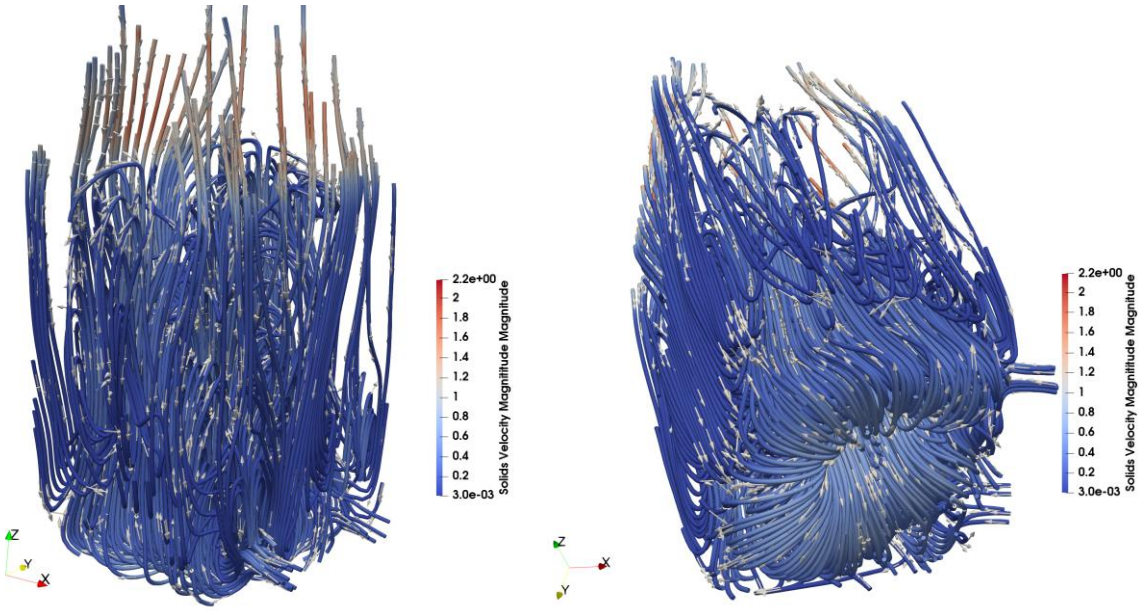

Figure 37 3-D streamlines for the combustor without heat exchanger

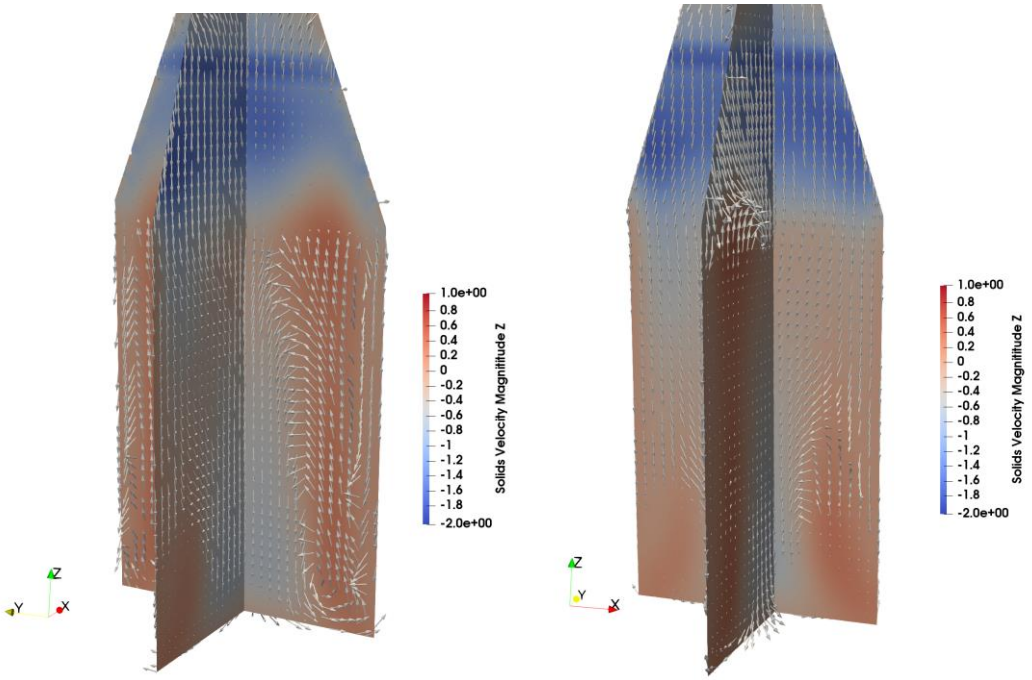

Figure 38 3-D gas solid velocity vectors in slices of x = 0 and y = 0

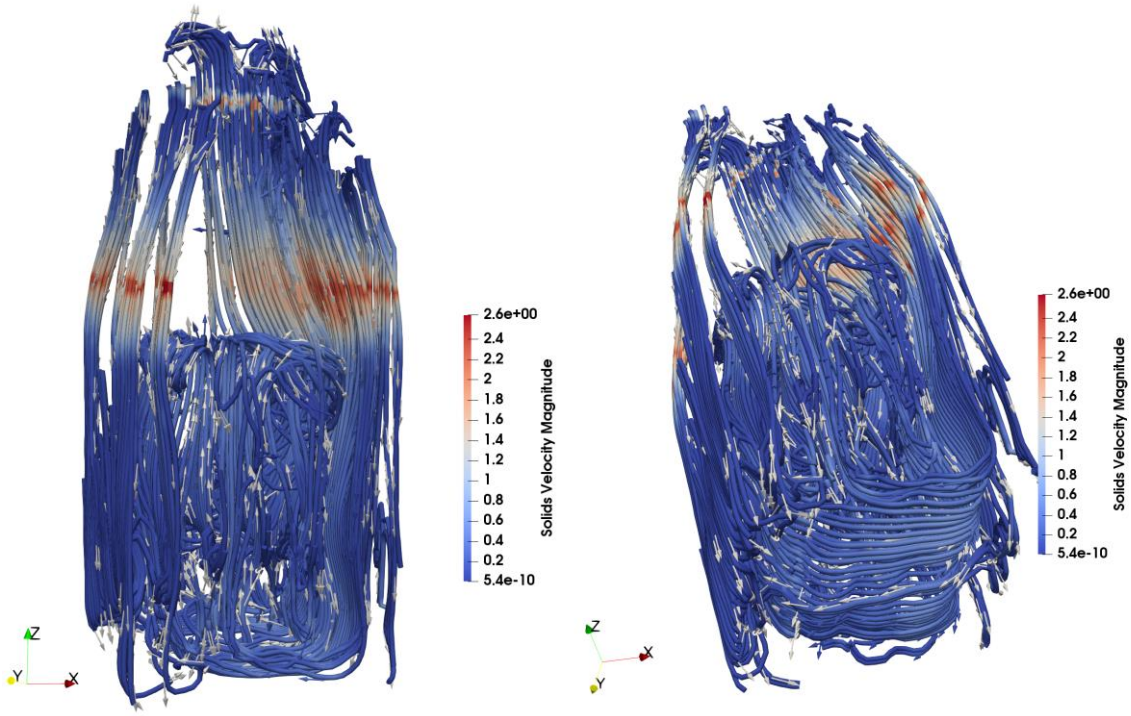

Figure 39 3-D streamlines for the combustor with heat exchanger

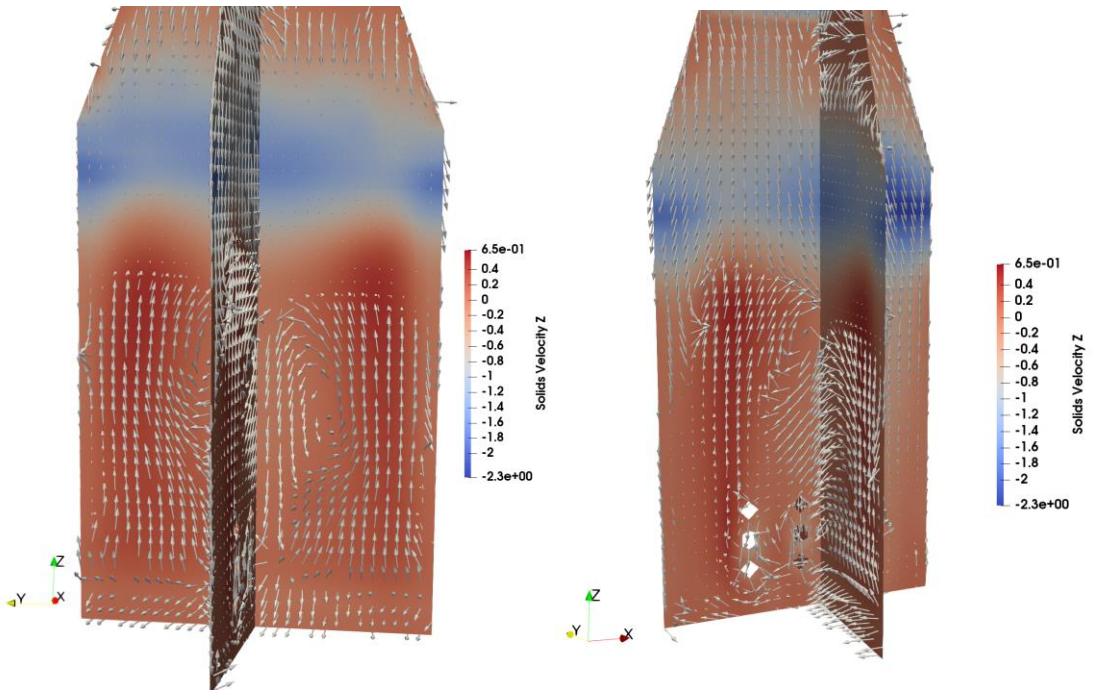

Figure 40 3-D gas solid velocity vectors in slices of x = 0 and y = 0

For the combustor with heat exchanger, the vortex ring where solid particles fall along the centerline are broken up into several vortex structures with small scales. The solids under the heat exchangers flow from the inlet of solids all the way to the other end and then rise around the heat exchangers. As shown in Fig. 41, vortex structures exist on top of and on the left of the heat exchanger. Moreover, small vortices form between different columns of heat exchangers. Along the perpendicular direction of the heat exchangers, two symmetry vortices exist, as shown in Fig. 42 (a). The local vortex structures are harmful to the heat exchanging efficiency.

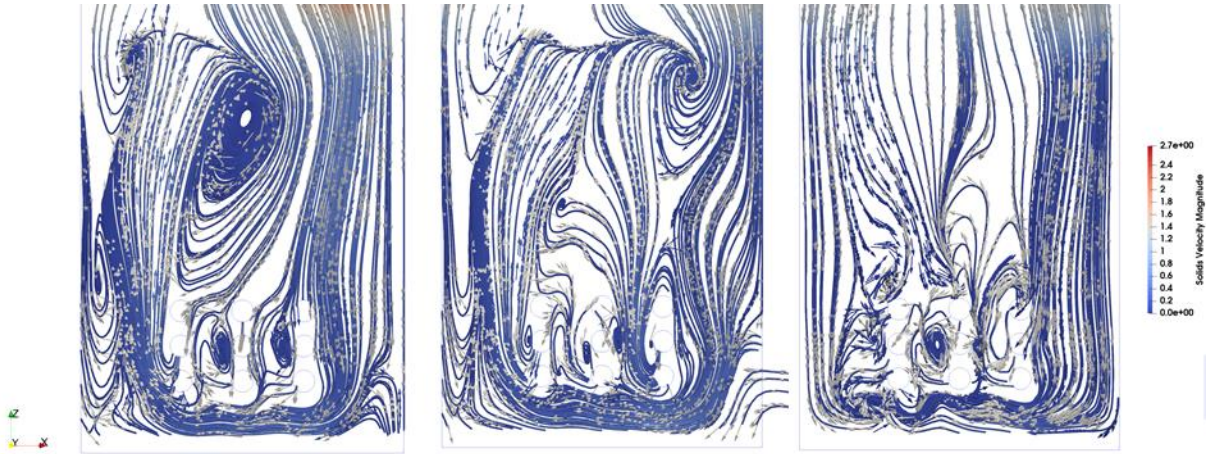

(a) $y = 0m$ (b) $y = 0.5m$ (c) $y = 1m$

Figure 41 Streamlines projected to the y plane

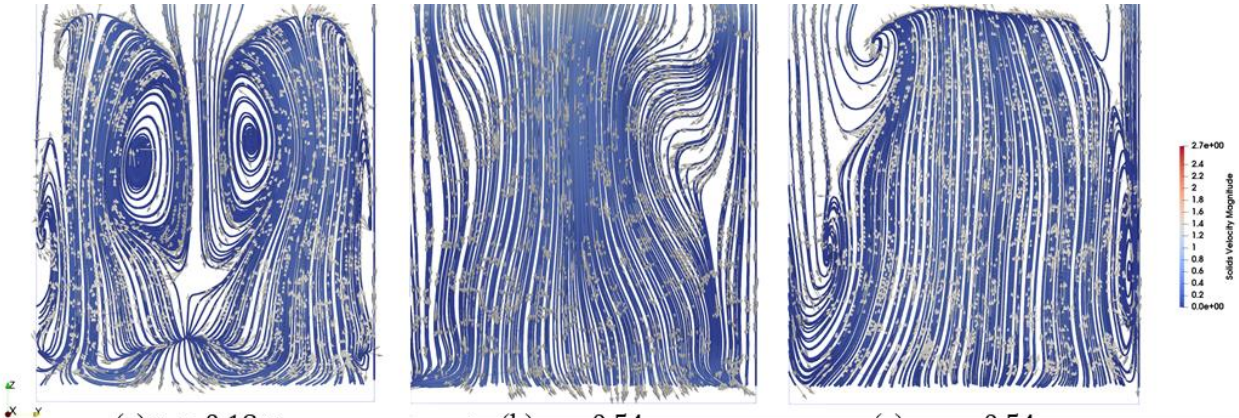

(a) $x = 0.18m$ (b) $x = 0.54m$ (c) $x = -0.54m$

Figure 42 Streamlines projected to the x plane

Figure 43 shows the distribution of particle age which is obtained through the Lagrangian filter with source locating in the inlet of particles. It shows that the particles are elder with the increase of combustor height and seldomly distributed in the vortex region near the left wall, i.e., on the opposite side of the particle inlet. The particles are able to distribute through the reactor within 20 seconds, which is shorter than, but in the same order of magnitude of, the time required for oxidation reaction. Thus, local hot spot due to maldistribution of solids are unlikely. More detailed solid transportation simulation can be performed once the detailed configuration of in-bed heat exchangers are given.

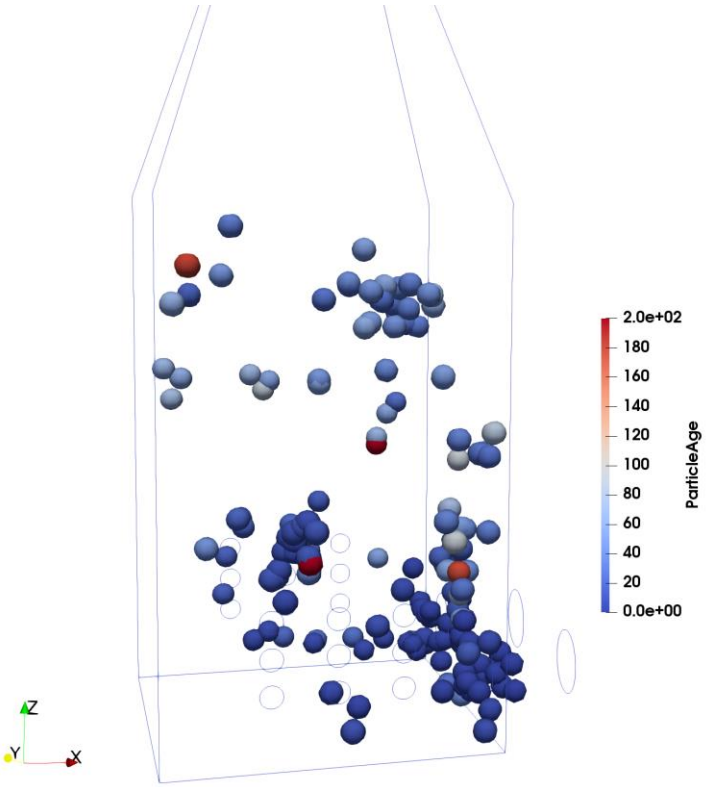

Figure 43 Particle Age (0.1s) distribution after 50 seconds of evolution

2.2.5 Conclusion of the Section

In this section, the hydrodynamic properties of the fluidized bed were studied, mainly focusing on the effects of solid wall boundary conditions and the diameter of the fluidized bed.

The solid wall boundary conditions can be characterized by Eq. (2.33). The parameter *A* can be either modeled by the method of Johnson and Jackson [20] using a specularity coefficient (as in

Ansys Fluent) or a tangential friction coefficient (as in MFIX), or be modelled by a constant value (as in MFIX).

Firstly, the grid convergence for the TFM simulation was studied and showed that the mesh with grid size of order 2.5 particle diameters is fine enough to predict the slug rising velocities. However, the grid size of order 2.5 particle diameters is still too fine for a large scale simulation, the grid size of order 10 particle diameters was also checked under Ansys Fluent, and the result shows that even with grid size of order 10 particle diameters, the macro cluster structures and the slug rising velocities can be captured almost unchanged.

Secondly, to best fit the slug rising velocities with the experimental result by Wang [14], the frictional angle in MFIX should be chosen as $\beta = 6°$ or a constant value of A should be chosen as $A = 1/40$, and the specularity coefficient in Ansys Fluent should be chosen as $\phi = 0.001$.

Then, with the calibrated parameters of solid wall boundary conditions, the effect of the diameter of the fluidized bed was verified using MFIX. In can be concluded that, with a certain bed height and a certain superficial velocity, whether the slug happens depends on the bed diameter. With the increasing of bed diameter, the slugging phenomena will disappear eventually.

For the bed with heat exchangers, a 2-D simplified cases were studied. It was observed even with the existence of the heat exchanger tubes, the slug will not happen with the horizontal space b between tubes to be 3, 6 or 12 inches (see Fig. 29) duce to the vertical space between them which allows the bypass of particles and fluid bubbles.

Lastly, a large-scale combustor with and without heat exchangers is studied. With the current set-up of the heat exchangers, the solid particles can be conveyed all the way to the leftist column of exchanger. But a large vortex exists near the left wall which needs to be further studied in the future design.

2.3 Heat transfer properties

For the heat exchanger in a fluidized bed, the heat convection coefficient is determined by the hydrodynamics characteristics, which includes the superficial velocity, the heat conduction coefficient of the gas and solid phase, etc. In this section, firstly, a bench scale fluidized bed was used to do the calibration of the heat conductivity coefficient of the solid phase. Secondly, a fluidized combustor coupling with a shrinking-core model was simulated and discussed.

A bench scale fluidized bed was firstly used to calibrate the heat transfer coefficient for the solid phase in this subsection.

2.3.1 Experimental Setup

The experimental apparatus is setup as shown in Fig. 44. The experiments are conducted in a column with interior diameter of 0.1397 m (5.5 inch). The total height of the column is 1.8288 m (6 ft). The diameter of the particle is 0.0015 m and the density is 2500 kg/m^3. The particles used for the experiment consists of Fe_2O_3 and TiO_2 and is the same as used in the previous sections. The minimum fluidized velocity under room temperature is 0.89 m/s. The initial bed height is 0.4 m. A heat exchanger with outer diameter of 0.0254 m (1 inch) is placed in the height of 0.3048 m.

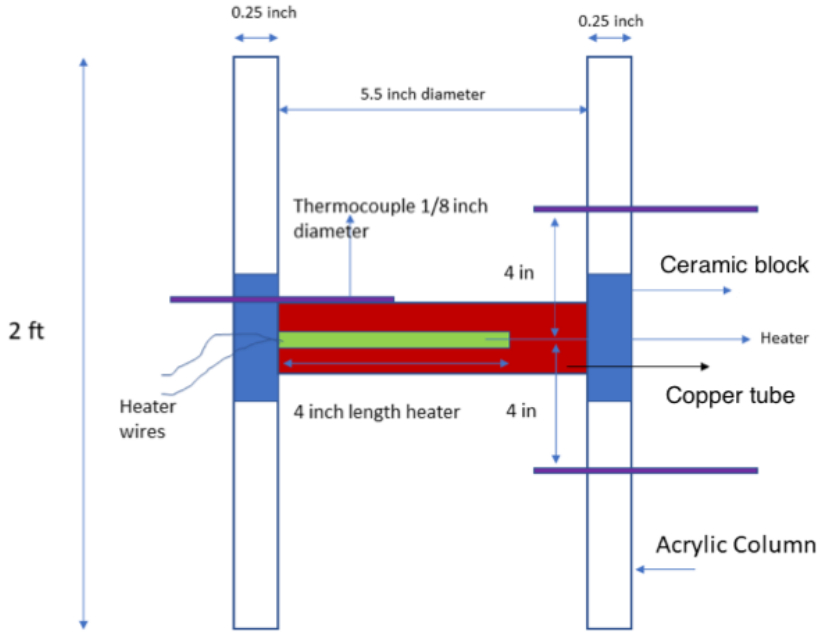

Figure 44 Schematic of the bench scale fluidized bed

The heat convection coefficients under different superficial velocity are shown as in Fig. 45. The value in Fig. 45 was calculated based on the temperature difference between the surface of the heat exchanger and the heat couple located 4 inches up and down the exchanger as shown in Fig. 44.

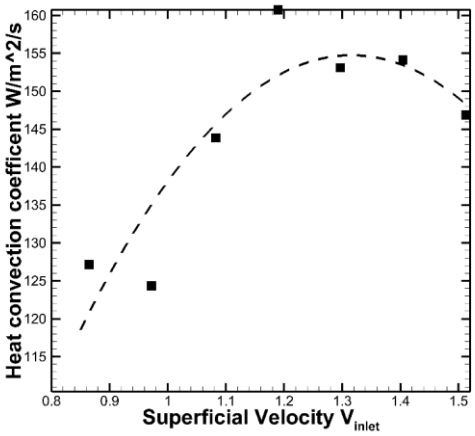

Figure 45 Effect of gas superficial velocity on heat convection coefficient

2.3.2 Mesh Dependency

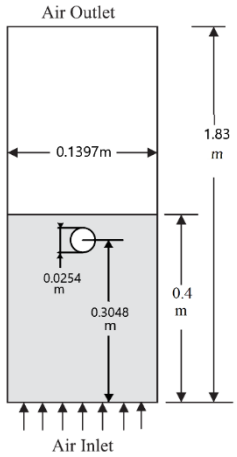

Figure 46 Illustration of the 2-D cold flow simulation

Firstly, a simplified 2-D model is setup in the simulation to check the mesh dependency of the heat convection coefficient, shown as in Fig. 46, where the cylinder heat exchanger is represented by a 2-D circle located in the height of 0.3048 m.

The initial bed height is set to be 0.4 m. And the initial bed void fraction is set to be 0.37. The wall of the left and right boundaries and around the heat exchanger are set to be non-slip for the gas phase with

$$v_{g,w} = 0, \tag{2.35}$$

and partial-slip for the solid phase with

$$v_{s,w} + A\frac{\partial v_{s,w}}{\partial n} = 0, \tag{2.36}$$

and A = 1/40 m in MFIX or a Johnson and Jackson [20] boundary condition with specularity coefficient of $\phi = 0.001$ in Ansys Fluent, which was calibrated in the previous section. The bottom is a mass inlet boundary and the upper is a pressure outlet boundary with pressure of 101325 Pa.

As to the thermal conditions, the left and right wall boundaries are set to be adiabatic and the wall boundary around the heat exchanger is set to be isothermal. The inlet temperature of the bottom boundary was set to be 298.15 K.

Four different sets of mesh, the close view of which are shown as in Fig. 47, are used to verify the mesh dependence of the heat convection coefficient. The superficial velocity V_{intlet} is chosen as 0.9716 m/s. And $k_p = 59.4\ W/(m \cdot K)$ in Eq. (2.29). The heat conductivity coefficient for the solid phase was determined by Eq. (2.27). The cell number for the base mesh, i.e. mesh 1 is 40×280. For meshes 2-5, the cell size around the heat exchanger are gradually reduced by a factor of 0.5. The heat convection coefficients developed over time simulated under different meshes are shown as in Fig. 48. The time averaged convection coefficient after $t = 6s$ is shown as in Table 4. It is shown that with the refinement of grids, the heat convection coefficient increases.

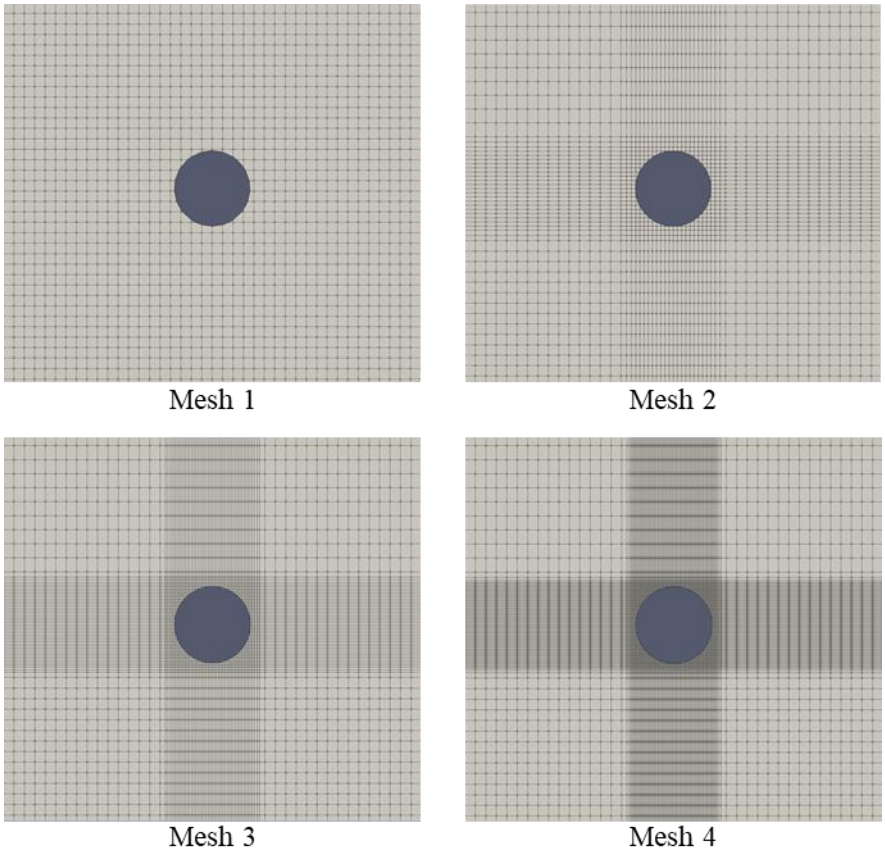

Figure 47 Close view of grids around the heat exchanger

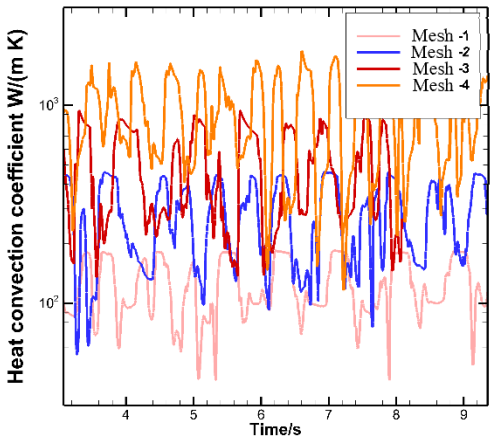

Figure 48 The heat convection coefficient under different grids with superficial velocity V_{intlet} = 0.9716 m/s

Table 4 The time averaged convection coefficient for different grids with V_{intlet} = 0.9716 m/s

	Mesh 1	Mesh 2	Mesh 3	Mesh 4
h_g	2.8	7.9	14.6	26.7
h_s	125.0	257.9	449.2	826.5
$h = h_g + h_s$	127.8	265.8	463.8	853.2

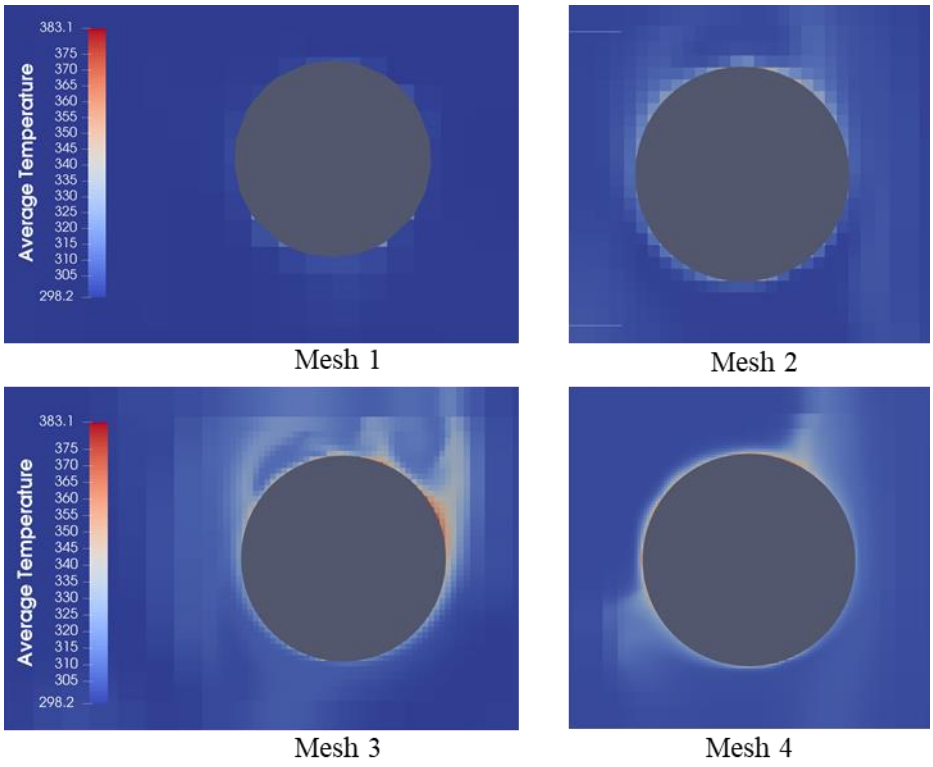

Figure 49 Snapshots (after time t = 6s) of the temperature field averaged over gas and solid phase as $T_{ave} = \epsilon_g T_g + (1 - \epsilon_g) T_s$

To explain the phenomenon in Table 4, snapshots of the phase averaged temperature field after time t = 6 s are plotted. As Fig. 33 shows, for the base grid, i.e. grid 1, the temperature boundary layer cannot even be captured. Thus, the temperature gradient around the hot exchanger is very small and obviously mismatched with experimental results. With the refinement of computational cells, the temperature boundary layer around the hot heat exchanger can be resolved. It should be noted that, the finest grid, i.e. Grid 4, the mesh size around the heater is of order 0.3 particle diameters and still no grid convergence was observed from the result in Table 4.

With such a refined computational mesh, the simulation will become extremely expensive. One possible approach is to use a filtered model for the heat conductivity coefficient. Another approach is that, we can keep on using a coarse mesh, i.e. with grid size of order 3-10 particle diameters, but with a calibrated solid heat transfer coefficient k_p as in Eq. (2.29).

2.3.3 Calibration of the Heat Transfer Coefficient

Figure 50 Illustration for the mesh with near wall grid size of order 3 particle diameters

As discussed in the last section, a mesh convergent numerical result is too expensive to be obtained and a filtered TFM which can accurately predict the heat flux is current unavailable. Thus, in this section, we keep the grid resolution in the normal direction of the wall boundary to a certain size, which is 3 particle diameters, and then use the grid of this scale to calibrate the solid heat conductivity coefficient. Figure 50 shows the 3-D mesh used for the simulation. The computational domain is the same as the experimental one. The development of the heat coefficient is shown as in Fig. 51.

The averaged heat convection coefficients under different superficial velocities are shown as in Fig. 51. The numerical results are comparable in the order of magnitude to the experimental ones when the heat conductivity coefficient for the particle k_p is chosen as 5.5 $W/(m^2 \cdot K)$.

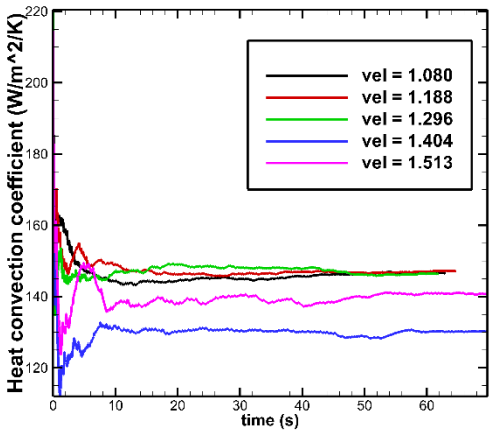

Figure 51 The time development of the averaged heat convection coefficient

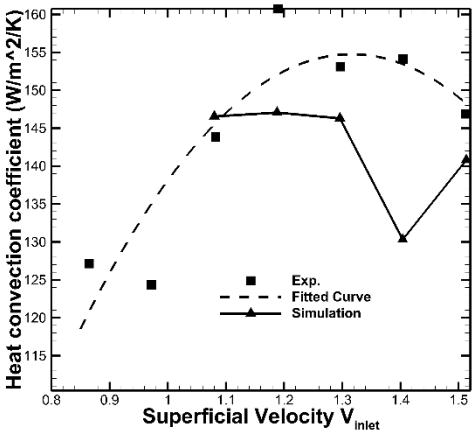

Figure 52 The numerical results for the heat convection coefficient. $k_p = 5.5\ W/(m^2 \cdot K)$

2.3.4 Conclusion of the Section

In this section, the heat transfer properties for the granular flow in the fluidized bed are studied using the TFM. A cold flow experiment was used as a baseline to calibrate the coefficient for the heat conductivity coefficient of the solid phase.

With a certain scale of the grid size, which is about 3 particle diameters in the current study, a calibrated $k_s = 5.5\ W/(m^2 \cdot K)$ was obtained, with which the experimental results can be approximately matched.

2.4 The Coupling of Shrinking Core Model

In this section, the shrinking core model for the reaction of the particles in the combustor will be coupled with the TFM model based on the Ansys Fluent solver.

The shrinking core model has been explained in the previous report of our group and will not be introduced again in this report.

The reaction equation is:

$$4Fe + 4TiO_2 + 3O_2 \rightarrow 2Fe_2TiO_5 + 2TiO_2 \tag{2.37}$$

The fully oxidized particle constitutes of Fe_2TiO_5 and TiO_2, with molar ratio of 1:1. The density for the fully oxidized particle is 2500 kg/m^3. For the shrinking model, the particle volume is assumed to be unchanged in the reaction. Thus, for the fully reduced particle, the density is 1808.17 kg/m^3.

In Fluent solver, we assumed that the particles constitute of two type of materials, one is $Fe \cdot TiO_2$ (material 1), the other is $FeTi_{0.5}O_{2.5} \cdot Ti_{0.5}O$ (material 2). The reaction can be written as:

$$Fe \cdot TiO_2 + 0.75O_2 \rightarrow FeTi_{0.5}O_{2.5} \cdot Ti_{0.5}O \tag{2.38}$$

According to the mass fraction of $Fe \cdot TiO_2$ and $FeTi_{0.5}O_{2.5} \cdot Ti_{0.5}O$, and the assumption of constant particle volume, the density of the particle can be obtained as:

$$\rho_p = \frac{\rho_1 \cdot \frac{X_1}{M_1} + \rho_2 \cdot \frac{X_2}{M_2}}{\frac{X_1}{M_1} + \frac{X_2}{M_2}}, \tag{2.39}$$

And the radius of unreacted $Fe \cdot TiO_2$ core can be obtained as:

$$r_1 = \frac{d_p}{2} \sqrt[3]{\frac{\frac{X_1}{M_1}}{\frac{X_1}{M_1} + \frac{X_2}{M_2}}} \tag{2.40}$$

where $\rho_1 = 1808.17$ kg/m^3, $M_1 = 135.709$ kg/kmol, $\rho_2 = 2500$ kg/m^3, $M_1 = 187.633$ kg/kmol, X_1 and X_2 are the mass fraction for $Fe \cdot TiO_2$ and $FeTi_{0.5}O_{2.5} \cdot Ti_{0.5}O$, respectively. After the determination the unreacted $Fe \cdot TiO_2$ cores, the reaction rate can be obtained through the shrinking core model.

Along with the exothermic reaction, heat will be released to the combustor. The standard (under 1 atm and 25 Celsius) reaction heat for reaction (2.38) is:

$$\Delta H = -3.970184 \times 10^8 \text{ J/kmol}.$$

The specific heat capacities for $Fe \cdot TiO_2$ and $FeTi_{0.5}O_{2.5} \cdot Ti_{0.5}O$ are shown as in Fig. 53. The specific heat capacities for the gas phase are set according to the property of idea gas, i.e. R/M_g, where R = $8.314 J/(mol \cdot K)$, and M_g is the mass per mole for the gas.

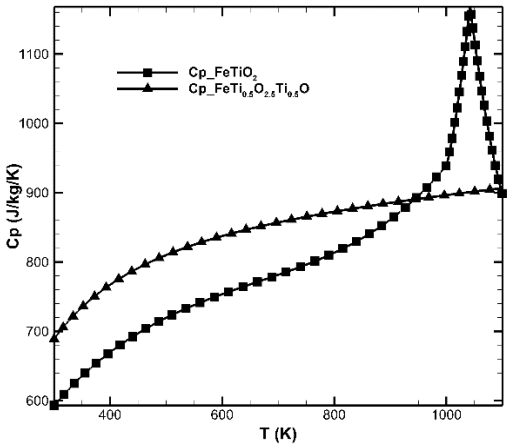

Figure 53 The specific heat capacities for $Fe \cdot TiO_2$ and $FeTi_{0.5}O_{2.5} \cdot Ti_{0.5}O$

A fluidized combustor with six heat exchangers is shown as in Fig. 54. The bed is 1 m high and the diameter of the heat exchanger is 0.0635 m (2.5 inches). Fully reduced particles are injected from a tube of diameter of 0.0254 m (1 inch) located at the bottom left of the bed. The velocity of particle injection is 0.054 m/s. A uniform air inflow with mole fraction of oxygen to be 20% is introduced from the bottom with a velocity of 1.36 m/s (2 times as the minimum fluidized velocity). The temperatures of the injected particles and the inflow air are 700 Celsius and 500 Celsius, respectively. The temperature at the surface of the heat exchanger is set to be 477 Celsius.

The bed was initialized fully filled with air. Figures 39-42 show the result of void fraction, mass fraction of Oxygen in air, mass fraction of FeTiO2 in solid particles and bed phase-averaged temperature at 10s, 50s, 100s and 150s.

As shown by the mass fraction of Oxygen in air and the phase-averaged temperature, although the particles are injected asymmetrically from only one side, with the bed diameter to be 14 inches and the superficial velocity to be 2 times of the minimum fluidized velocity, the particles can still be uniformly mixed with air, resulting in almost evenly distributed bed temperature in bed width direction. Figure 43 is an illustration of the particle residence time through particle tracer, which again confirmed that the granular phase is fully mixed with gas phase.

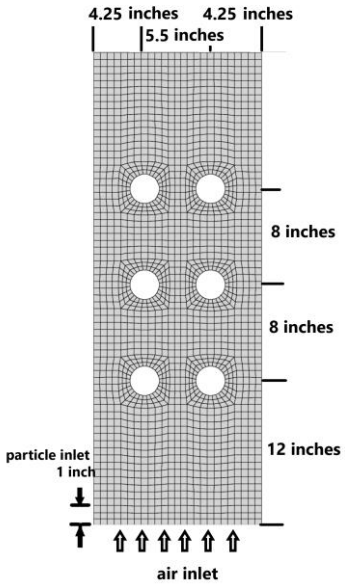

Figure 54 Illustration of the computational domain for the combustor with reaction

With the given air and particle flow rate, the percent conversion of the $\mathrm{Fe} \cdot \mathrm{TiO}_2$ in the combustor will be approximately:

$$\frac{\rho_{air} V_{air_{inlet}} D_{air_{inlet}} X_{O_2} * M_{FeTiO2}}{M_{air} * 0.75 * \rho_p V_p D_{particle_{inlet}} \epsilon_s} = 0.26,$$

which is in accordance with the result shown by Fig. 57, where in most area the percent conversion of the $\mathrm{Fe} \cdot \mathrm{TiO}_2$ is about 0.31. The simulation percent conversion result is a little high than 0.26 because of the extra air inflow along with the particle injection in the bottom left tube.

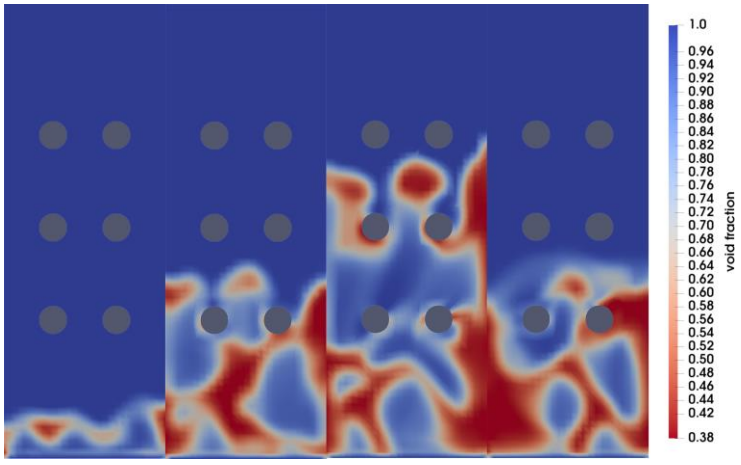

Figure 55 Void fraction at time 10s, 50s, 100s, 150s from left to right

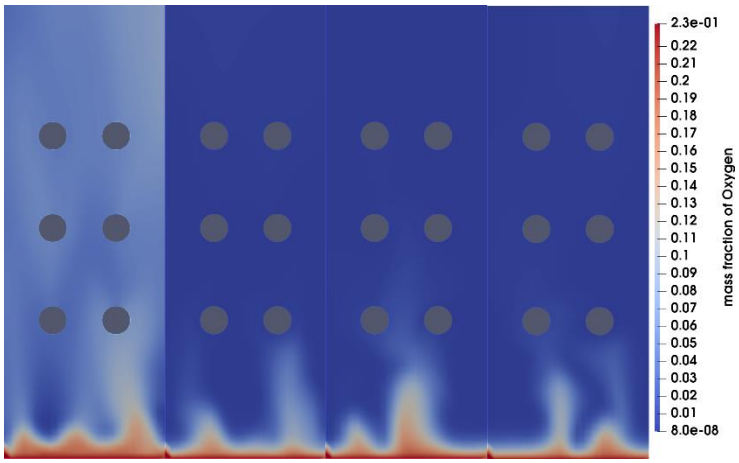

Figure 56 Mass fraction of Oxygen in air at time 10s, 50s, 100s, 150s from left to right

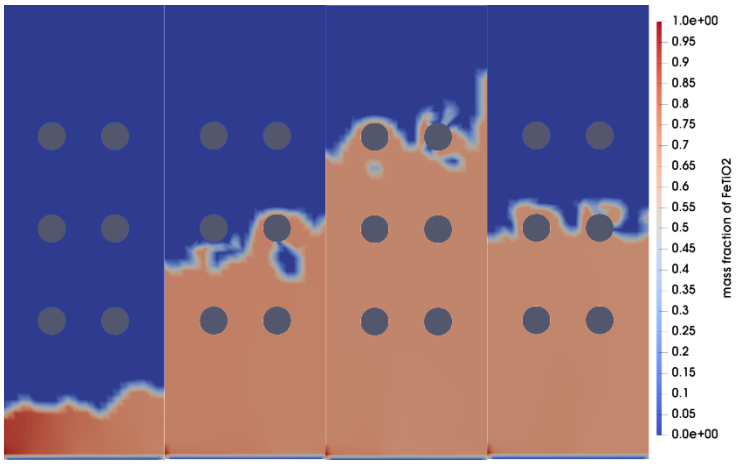

Figure 57 Mass fraction of FeTiO2 in solid particles at time 10s, 50s, 100s, 150s from left to right

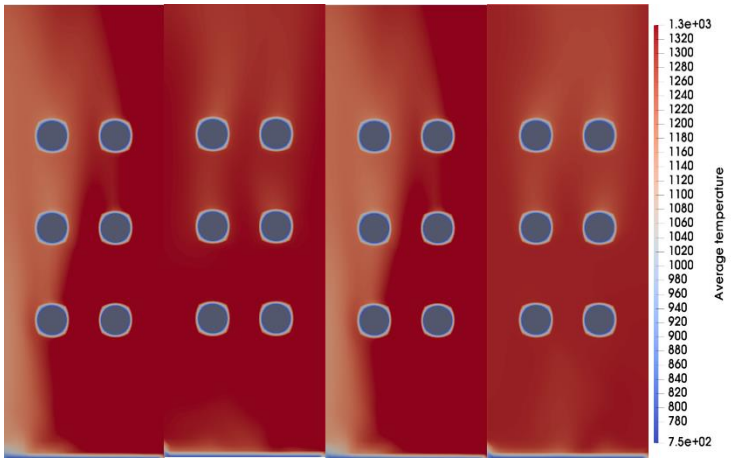

Figure 58 Phase averaged bed temperature at time 10s, 50s, 100s, 150s from left to right

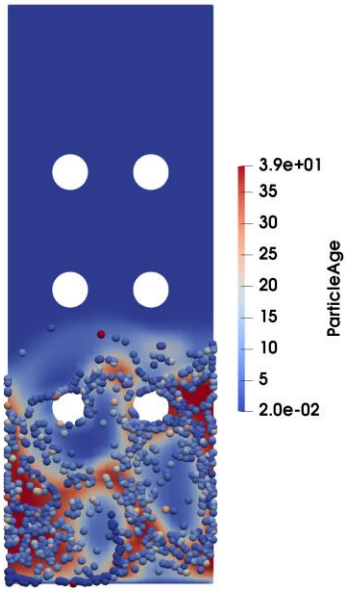

Figure 59 Illustration of the particle tracer at time 150 s. The particles are colored by particle residence time in the bed. The background color is the void fraction

Figure 60 shows the development of the averaged bed temperature. It shows that the steady state bed temperature is around 1325 K with the current setting. Figure 61 shows the time development of the heat transfer coefficient based on the averaged bed temperature and heat exchanger surface temperature. Since upper and middle heat exchangers are only partially immersed in the granular flow, as shown by Fig. 55, the heat convection coefficients are much lower than the bottom tube. This phenomenon reveals that the hydrodynamic properties around the heat exchangers plays an important role in the determination of heat convection coefficient and the solid particle phase is the dominant factor determining the heat convection coefficient.

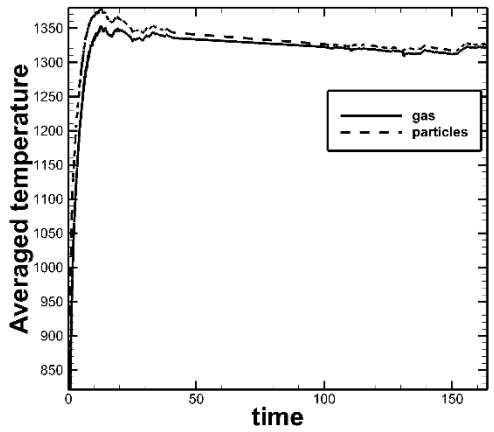

Figure 60 Average bed temperature of the combustor

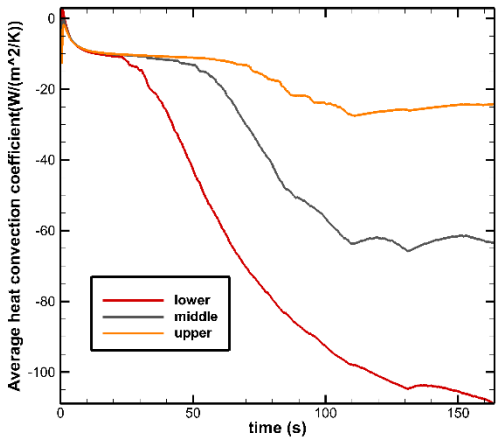

Figure 61 Average heat convection coefficient for the three rows of heat exchangers

3. Heat Exchanger Network Integration and Optimization

The design of heat exchanger network (HEN) is one of the most important aspects in the design of coal direct chemical looping (CDCL) process. Besides, an optimized HEN can maximize the heat recovery within CDCL process, thus increasing the net plant efficiency of CDCL process, which leads to potential cost saving for the whole process.

3.1 Configuration of CDCL Unit and Static Model Setup

Based on previous developed Aspen Plus model of CDCL unit, the project team updated the original design of individual CDCL unit based on experience of experiment these years.

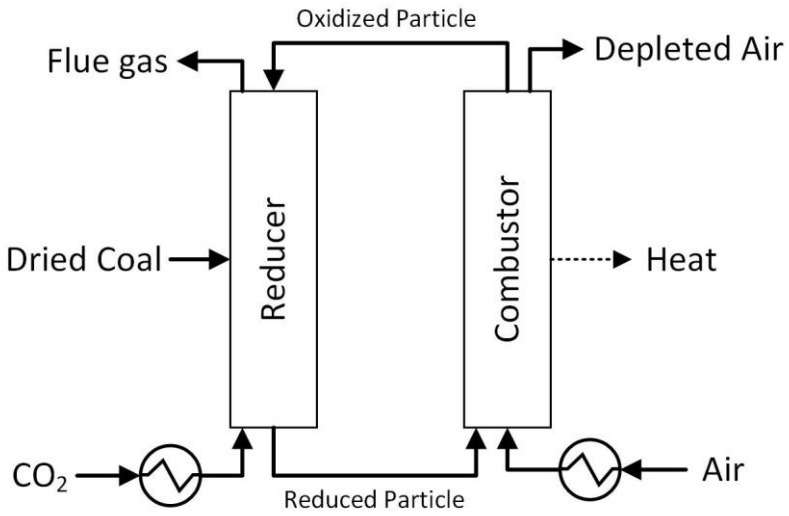

Figure 62 Block flow diagram of CDCL unit

Figure 62 shows the configuration of individual CDCL unit. The reducer reactor is a moving bed reactor and combustor reactor is a fluidized bed reactor. Dried coal is prepared to inject to the middle of reducer and oxidized by iron-based oxygen carrier particle moving downward. CO_2 is preheated and injected to the bottom of reducer as the enhancer gas to intensify oxidation of coal. Reduced particle is transported to combustor to be fluidized and oxidized by preheated air. Then oxidized particle is sent back to reducer to start another redox cycle. In-bed heat exchanger (IBHX) is installed in combustor to extract high quality heat shown in Figure 62, which is the main heat source for power generation. Heat is also recovered in flue gas from the top of reducer and O_2 depleted air from the top of combustor. As a standalone CDCL unit, the

configuration shown in Figure 62 neglects heat integration choices for gas preheating and heat recovery.

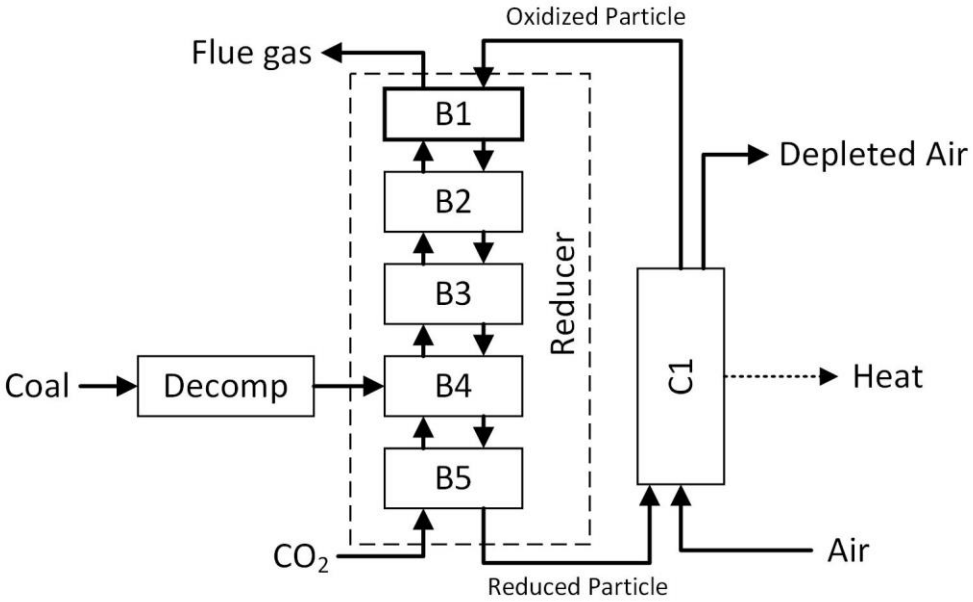

Figure 63 Aspen Plus model of CDCL unit

The Aspen Plus model of CDCL unit is shown in Figure 63. Coal is treated as a non-conventional component. “Decomp” is a conversion reactor block to enable the reaction between coal and other component in simulation. The calculation of “Decomp” is based on the result of proximate and ultimate analysis for coal. “B1” – “B5” are RGibbs blocks connected as solid moving downward and gas moving upward. They are corresponding to the sections from top to the bottom of reducer. “C1” is a RGibbs block representing combustor. The RGibbs block gives the outlet component concentration under thermodynamic equilibrium. The heat from combustor is calculated when the combustor temperature is set.

With the setup of basic Aspen Plus model, further modifications were applied to the CDCL reactor model to match experimental results from sub-pilot CDCL unit operation. We then updated the experiment validated model to reflect the practical reactor setting in large scale plant.

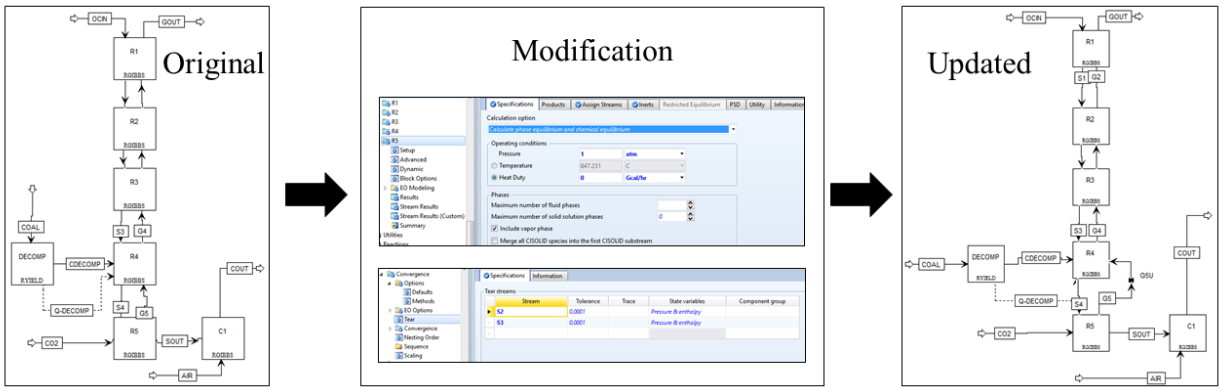

Figure 64 Modification of CDCL model

The experimental results from sub-pilot CDCL unit were utilized to validate the isothermal CDCL model. Under the same operating conditions, i.e., temperature, pressure, feedstock flowrate, etc., both experiment and simulation show nearly full conversion of coal. The validated model was then modified to reflect real reactor settings and operation situation in large scale plant, as shown in Figure 64. The reactor blocks shown in Figure 63 were set to be adiabatic and parameters related to calculation within the block were also adjusted to help balance and convergence of blocks. Besides, stream tearing and calculation methods of the whole model were set to convergent this model with multiple cycle. With the established static CDCL unit model, the project team continued to develop the process model for the overall CDCL power generation process including flue-gas desulfurization (FGD) unit, fans, compressors, steam cycle and HEN.

3.2 Overall Process Model Setup for CDCL Power Generation Process

The process model for overall CDCL power generation process was developed by integrating other essential units and equipment to the CDCL reactor model, which includes but not limit to fans for feedstock introduction, product extraction, and gas recycle, FGD unit, compressor for CO_2 sequestration, drying unit for coal, and steam cycle for power generation.

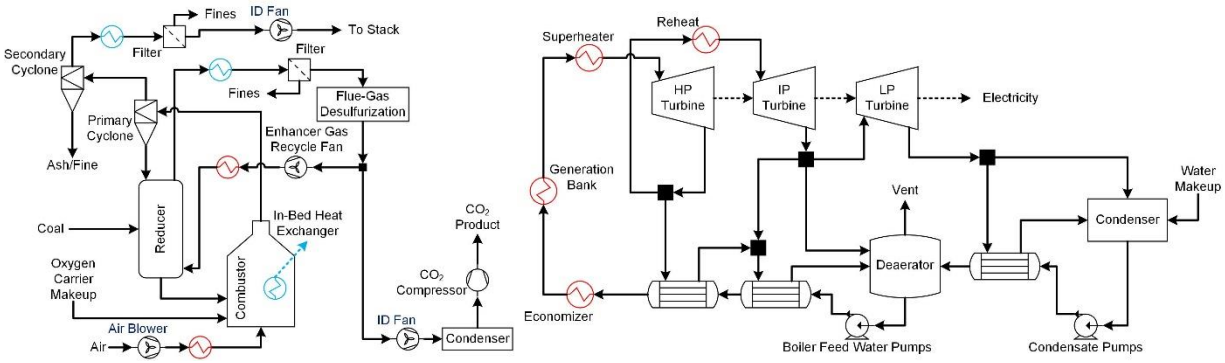

Figure 65 CDCL power generation process block flow diagram (HEN not specified)

Figure 65 depicts the layout of the overall process. The highlighted heat exchangers are identified heat sources (blue) and heat sinks (red). While there is only heat transfer between steam cycle and other components of the process, steam cycle is shown as an isolated part in Figure 65. The steam cycle was simulated under supercritical condition based on a steam cycle model developed by Babcock and Wilcox (B&W) and Pacific Northwest National Laboratory (PNNL) for prior studies on separate applications. It is noted that steam is extracted at various points along the high pressure (HP), intermediate pressure (IP) and low pressure (LP) turbine to provide heat for feedwater preheating shown in Figure 4. The block settings and stream parameters of the steam cycle model were adapted to match the energy efficiency of steam cycle used in baseline case, which is referring to Case B12A in DOE/NETL-2015/1723.[25] The project team considers the adaption of steam cycle model would maintain the reliability of the comparison between CDCL power plant and conventional power plant.

According to the process layout shown in Figure 65, the overall process model was established based on the CDCL static model integrated with auxiliary equipment and steam turbine cycle. Table 5 summarizes the basic simulation settings for Aspen Plus model. The compressed CO_2 pressure is retrieved from the target pressure for CO_2 sequestration and the parameters of steam cycle is the same as the parameters of supercritical steam cycle in DOE/NETL-2015/1723.[25] Table 6 shows the composition of coal in use, which is Illinois #6 bituminous coal in DOE/NETL-341/011812.[26]

Table 5 Simulation settings for Aspen Plus model

Name	Setting
Property Method	PR-BM (CDCL unit) STEAMNBS (steam cycle)
Coal	Illinois #6
Oxygen carrier composition	Fe_2O_3 20%, TiO_2 80% (weight %)
Compressed CO2 pressure, bar (psi)	153 (2215)
Steam cycle, MPa/°C /°C (psig/°F/°F)	24.1/593/593 (3500/1100/1100)

Table 6 Composition specification of coal used in simulation[26]

Proximate Analysis (weight %)		Ultimate Analysis (weight %)	
Moisture	11.12	Moisture	11.12
Ash	9.70	Carbon	63.75
Volatile Matter	34.99	Hydrogen	4.50
Fixed Carbon	44.19	Nitrogen	1.25
HHV, kJ/kg	27113	Chlorine	0.29
HHV, Btu/lb	11666	Sulfur	2.51
LHV, kJ/kg	26151	Ash	9.70
LHV, Btu/lb	11252	Oxygen	6.88

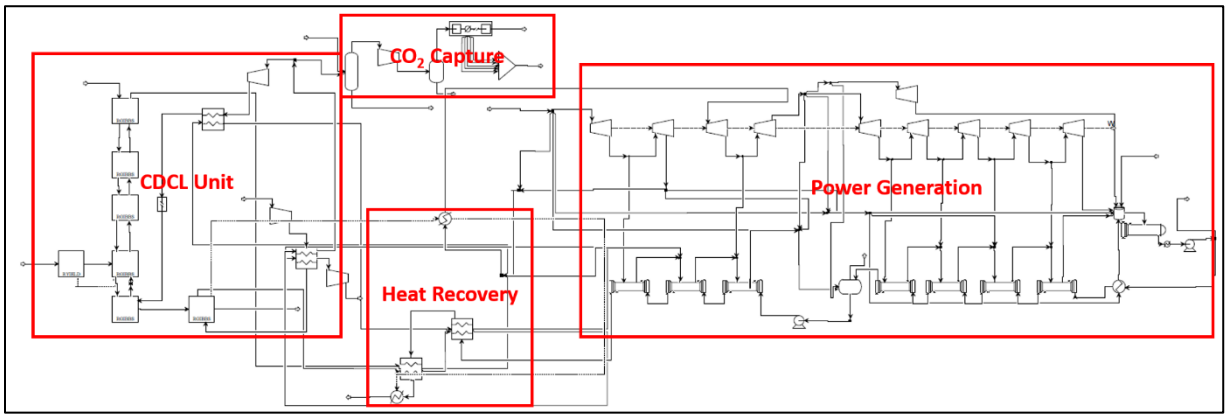

Figure 66 Aspen Plus model of CDCL power generation process

Figure 66 shows the comprehensive Aspen Plus process model, of which the heat recovery part covers the preliminary HEN design by balancing the recoverable heat from heat sources and heat consumption for preheating and steam generation. Gas from reducer is cooled down, purified and compressed to capture high purity CO_2. Heat is recovered from in-bed heat exchanger in

combustor as well as hot gas produced by reducer and combustor. Part of the heat would preheat air to combustor and enhancer gas to the bottom of reducer. The major part of heat is recovered by steam cycle for power generation. The key operating target and limitations to develop the process model are listed below:

- The combustor of CDCL unit is operated lower than 1050 ℃;
- The particle circulation rate in CDCL unit is determined to achieve full conversion of coal to CO_2/H_2O, maintain the bottom temperature of reducer higher than 800 ℃, and reflect the circulation rate tested in sub-pilot and pilot CDCL unit;
- The amount of air sent in combustor is set to be at least 5% excess compared to the stoichiometric amount required to convert all the reduced iron oxide from reducer to Fe_2O_3;
- Streams with temperature lower than 371 ^{o}C (700 ^{o}F) were not considered as heat source that are available for steam cycle based on design experience of the project team.

3.3 HEN Design and Optimization for CDCL Power Generation Process

With the information of heat balance from the heat recovery section in Figure 66, the composite curve of the overall process was plot and the HEN were specified accordingly. Besides, the project team decided to consider the eight CDCL modules of the commercial process as one object in the design of HEN, which could represent the actual operation and reduce the calculation effort as the modules would be operated identical with the heat from IBHX assigned to different usage.

Based on prior design of power system, streams with temperature lower than 371℃ (700 ℉) were not considered as heat source that are available for steam generation or reheat. Besides, streams with temperature lower than 149 ℃ (300 ℉) were not considered as heat source for feedstock preheat. The HEN of the overall CDCL power generation process was divided into two individual sub-networks, one with hot streams higher than 371℃ (steam network) and the other with hot streams lower than 371℃ (preheat network). Two sub-networks saved computation effort for modification and optimization compared to one large network. Additionally, Aspen Energy Analyzer (AEA) was utilized to support HEN optimization.

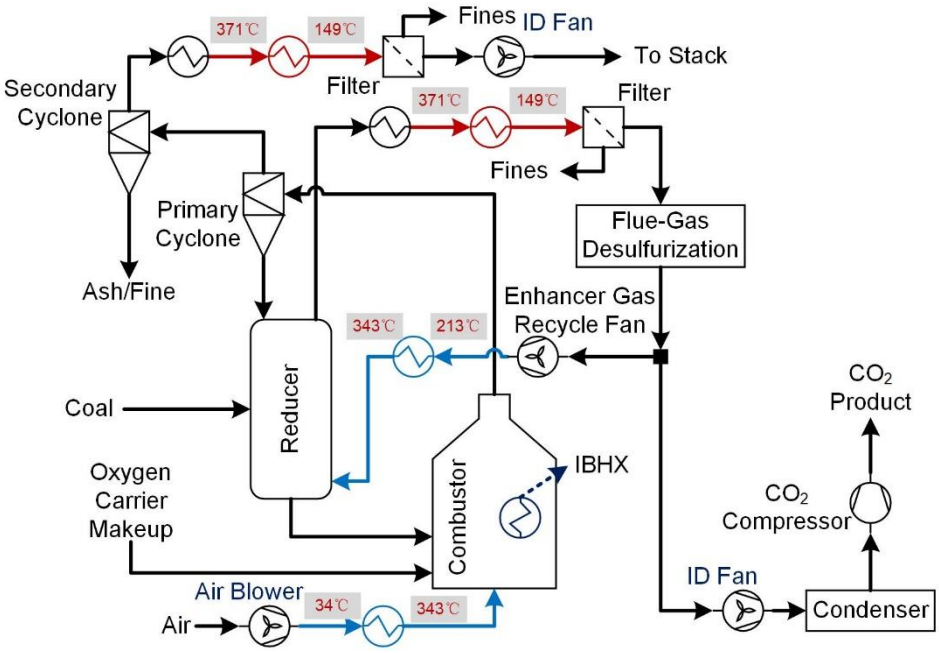

Figure 67 Hot and cold streams in preheat network

The sub-network with hot streams lower than 371 ℃, or preheat network, includes hot gas from chemical looping reactors and cold feedstock to be preheated. The hot and cold streams in this sub-network are shown in Figure 67. Here, the preheated feedstock to reactors can only reach 343 ℃ as the highest temperature of hot streams is 371 ℃ and the minimum cold/hot end temperature approach is 28 ℃ (50 ℉) for gas-gas heat exchange.[27]

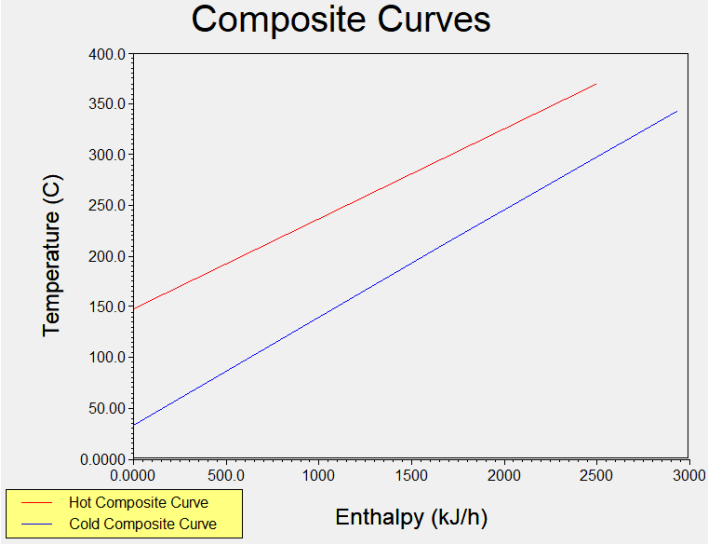

Figure 68 Composite curves of hot and cold streams in preheat network

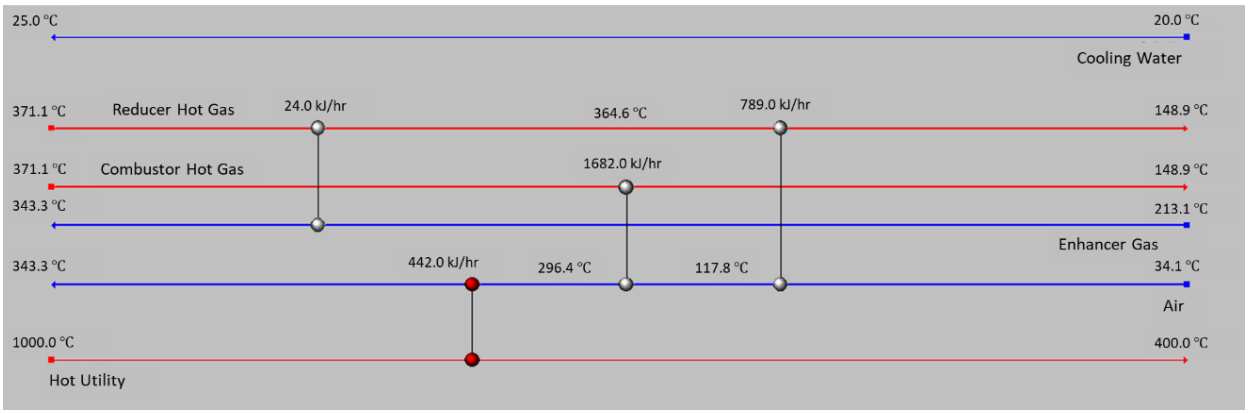

Figure 69 Optimized HEN design of preheat network

The composite curve of the preheat network is shown in Figure 68. For convenience, the heat duty and mass flow rate of each stream were scaled based on 1 kg/hr of Illinois #6 coal injected to reducer. Figure 69 shows the optimized HEN design configured by AEA using a minimum approach temperature of 28 ℃. In this optimized design, enhancer gas is preheated by hot gas from reducer. Then all the left recoverable heat from reducer and combustor hot gas is utilized to preheat air. Hot utility makes up the final heat up step for air. The requirement of hot utility indicates that the recoverable heat from the hot streams was not sufficient for air preheat to 343 ℃ with the 371 ℃ limitation of the hot streams in preheat network, which could significantly the recoverable heat from IBHX.

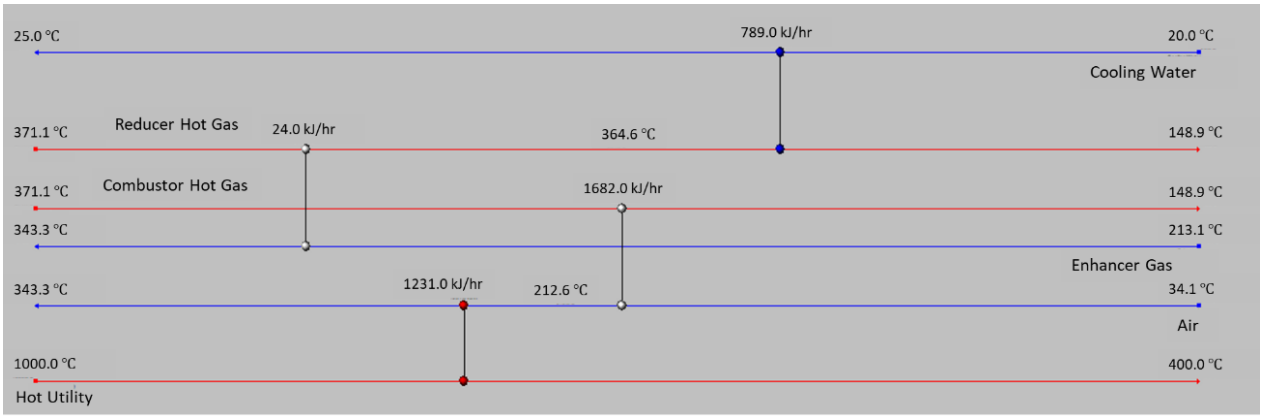

Figure 70 Refined HEN design of preheat network

The optimized HEN design of preheat network was further refined based on previous industrial designs and experience on power system. During CDCL plant operation, it is possible that the hot gas from reducer, as well as enhancer gas split from it, contains unconverted coal volatile or CO, which is combustible. Besides, O_2 is included in air and hot gas from combustor. The project team decided to forbid heat exchange between reducer hot gas and air as well as combustor hot gas and enhancer gas to prevent the risk that flammable materials meet O_2 in heat exchangers due to false operation or equipment malfunction. The refined HEN design is shown in Figure 70. Further, hot streams higher than 371 ℃ or any possible hot utility was used to generate steam for power production instead of feedstock preheat. Thus, for this case, air was injected to combustor at 212.6 ℃ in the 550 MWe CDCL plant.

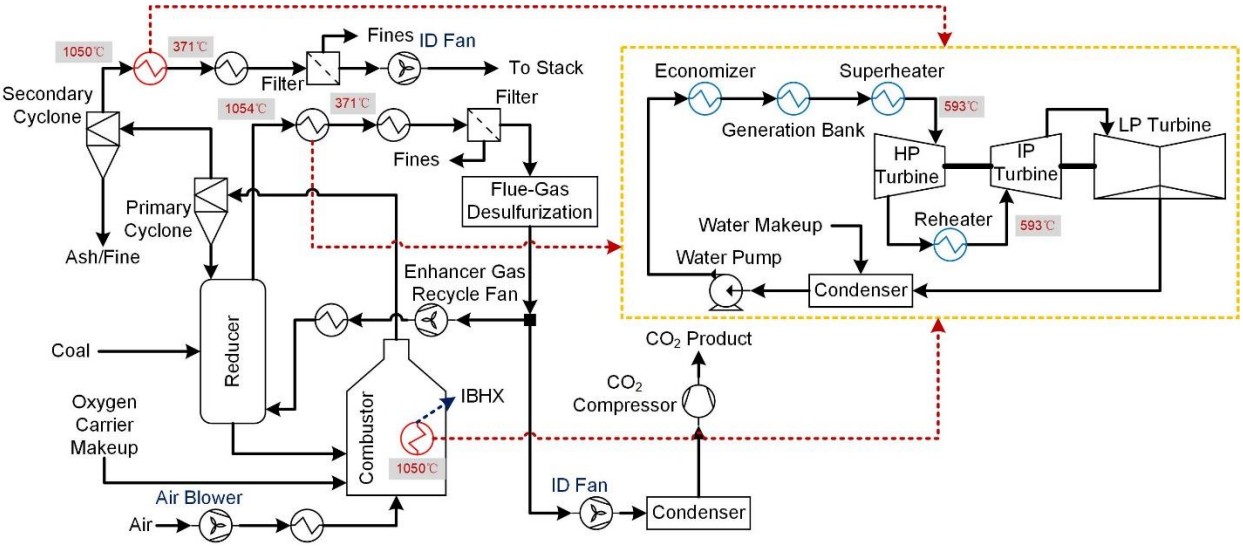

Figure 71 Heat exchange positions in steam network

The sub-network with hot streams higher than 371 ℃, or steam network, includes hot gas streams from reducer and combustor, heat from in-bed heat exchanger (IBHX) and membrane wall, and water/steam for superheat or reheat. The heat exchange positions are highlighted in Figure 61. Specifically, for the heat from IBHX, we use a 1 ℃ temperature change and mass flow rate of combustor hot gas to create a hot stream for that heat to enable calculation in AEA.

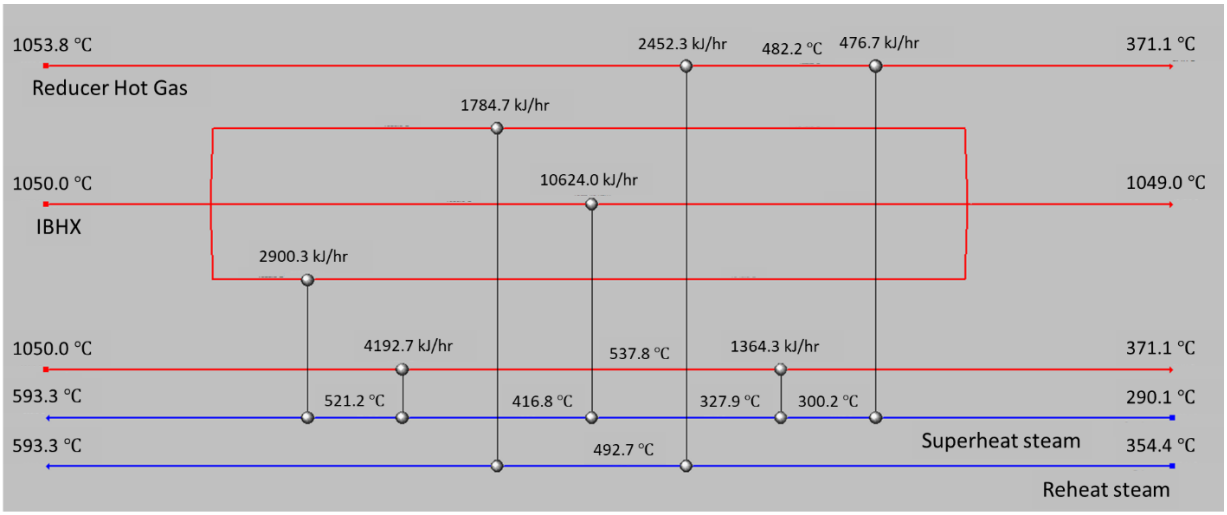

Figure 72 Refined HEN design of steam network

Follow the same procedure done for the preheat network, the steam network design was optimized and refined. For convenience, heat duty and mass flow of all the streams were scaled based on 1 kg/hr of Illinois #6 coal injected to reducer. Figure 72 shows the refined HEN design of steam network.

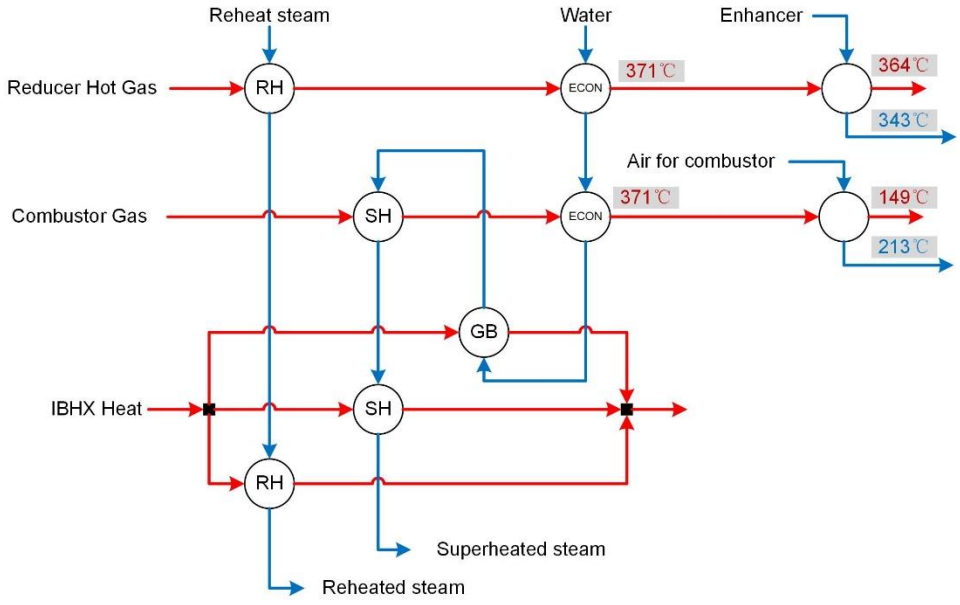

Figure 73 Optimized HEN design of CDCL power generation process (ECON: Economizer; GB: Generation Bank; SH: Superheater; RH: Reheater)

Combining the HEN design of the sub-networks in Figure 70 and Figure 72, Figure 73 shows the layout of the optimized HEN design for the overall process. It was noticed that the reducer hot gas is at 364 ℃ after heat recovery and much heat is still recoverable as the lower temperature limit is 149 ℃. The boundary of HEN design should be expanded to include as many streams as possible to make use of the heat. Besides, the temperature of heated air is only 213 ℃ due to the restriction of exchangeable streams and hot stream temperature, which we expected to be not less than 300 ℃ for the convenience of combustor operation and heat extraction from IBHX. As the limitation of hot stream temperature (lower than 371 ℃) is due to the property of material of normal air preheater, the restriction of air preheat could be relaxed by using material sustaining under high temperature to manufacture the air preheater.

Following the improvement possibility from the optimized HEN design, two changes was made for the design of HEN. The air for coal pulverizer was included in the HEN to be preheated by the hot gas from reducer. The other one is to relax the 371 ℃ and 149 ℃ limitation of air preheater and to preheat the air to 400 ℃. In addition, suggestions based on CDCL related experiments during the project period were incorporated to the simulation model as well as the HEN design. For the simulation model, the project team increased the amount of enhancer gas to the bottom of reducer to maintain full conversion of coal in reducer based on the results from CDCL pilot unit operation. For the HEN design, the requirement of higher than 371 ℃ (700 ℉) for steam generation or reheat was relaxed to be higher than 343 ℃ (650 ℉).

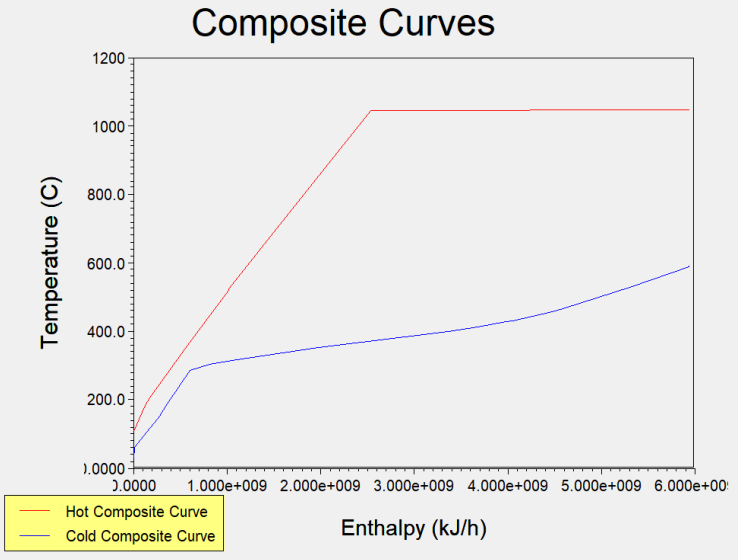

Figure 74 Updated composite curve for CDCL power generation process

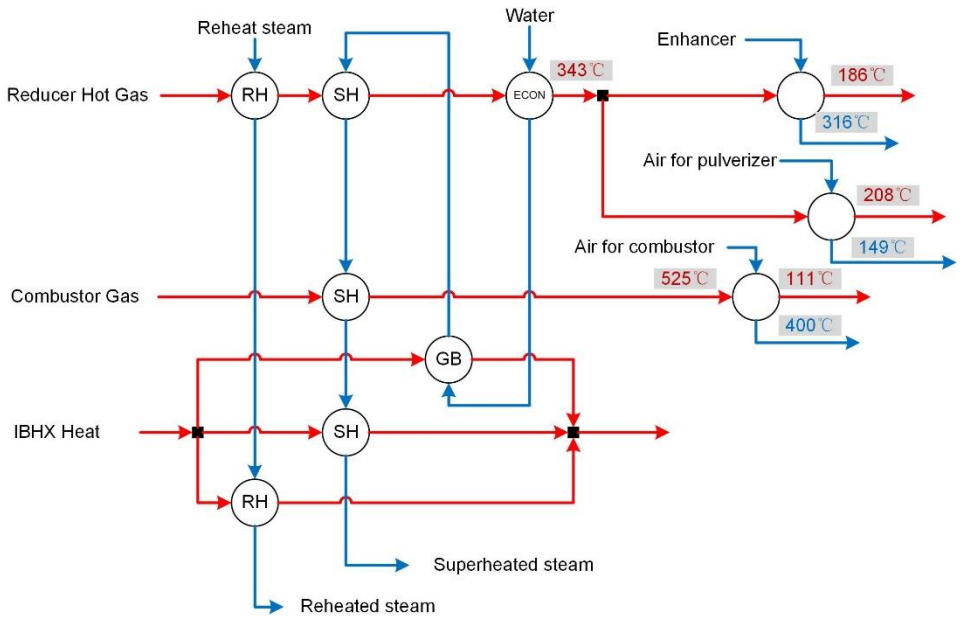

Figure 75 Updated HEN design of CDCL power generation process (ECON: Economizer; GB: Generation Bank; SH: Superheater; RH: Reheater)

With all the changes included, Figure 74 shows the updated composite curve (for 550 MWe net power production) and Figure 75 shows the updated HEN design. Compared to the design in Figure 73, the structure of HEN in Figure 75 only has minor change. The economizer on combustor gas stream was removed due to the increased heat consumption for air preheat. Part of the superheater area was assigned to reducer gas stream to make use of the excess high-grade heat due to the relaxation of hot streams available for steam generation from 371 ℃ to 343 ℃. After preheating the air for pulverizer and enhancer gas, the temperature of reducer gas is at 186 ℃ and 208 ℃, which indicates more heat is recovered compared to the HEN in Figure 73.

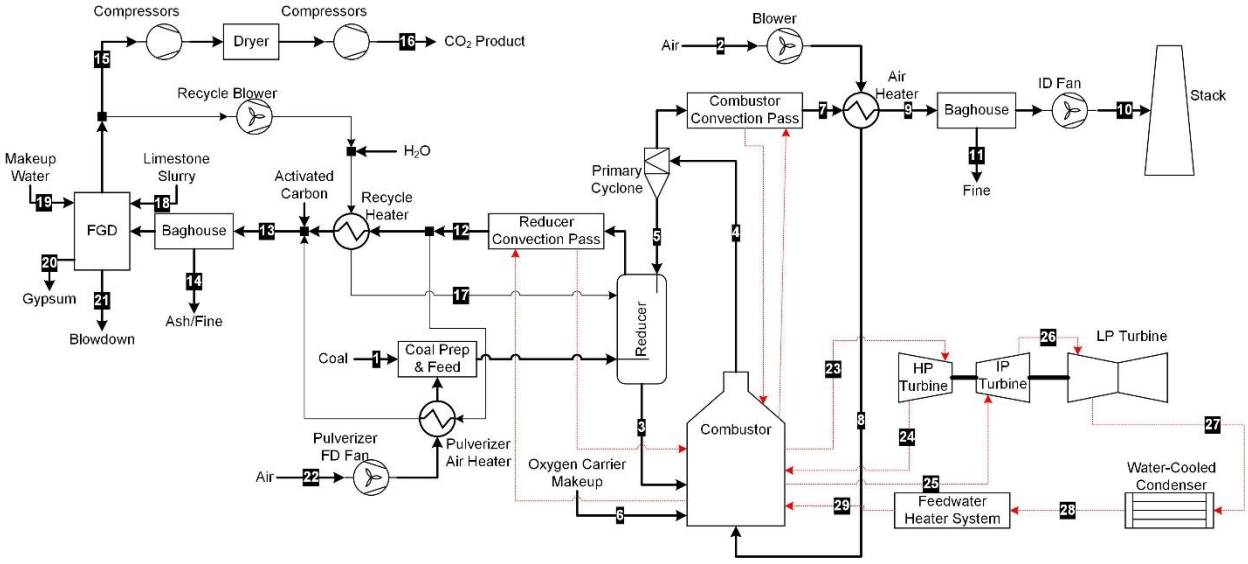

Figure 76 550 MWe CDCL power generation process flow diagram

With the updated HEN design, the overall process model of the CDCL power generation process with 550 MWe net power production was finalized by the project team. The process flow diagram is shown in Figure 76 and Table 7 provides the stream information for the corresponding mass balance. The commercial embodiment of CDCL produces 550 MWe with a steam output of 1,104,498 kg/hr (4,198,611 lb/hr) at 24.23 MPa (3514.7 psia) / 593 ℃ (1100 ℉), and 1,583,363 kg/hr (3,490,717 lb/hr) reheat steam at 4.73 MPa (685.8 psia) / 593 ℃ (1100 ℉). In addition, Table 8 shows the performance summary of the CDCL power generation process. Compared to the net plant HHV efficiency of baseline Case B12B in DOE/NETL-2015/1723, which is 32.5% with 90% CO_2 capture, the CDCL power plant with updated HEN design shows 12.9% increase.[25]

Table 7 550 MWe CDCL power generation process mass balance

	1	2	3	4	5	6	7	8	9	10	11	12	13	14	15
V_L Mole Fraction															
Ar	0.0000	0.0092	0.0000	0.0112	0.0000	0.0000	0.0112	0.0092	0.0112	0.0112	0.0000	0.0001	0.0001	0.0000	0.0006
CO2	0.0000	0.0003	0.0000	0.0004	0.0000	0.0000	0.0004	0.0003	0.0004	0.0004	0.0000	0.6488	0.6505	0.0000	0.8174
H2	0.0000	0.0000	0.0000	0.0000	0.0000	0.0000	0.0000	0.0000	0.0000	0.0000	0.0000	0.0000	0.0000	0.0000	0.0000
H2O	0.0000	0.0099	0.0000	0.0121	0.0000	0.0000	0.0121	0.0099	0.0121	0.0121	0.0000	0.3369	0.3352	0.0000	0.1740
HCl	0.0000	0.0000	0.0000	0.0000	0.0000	0.0000	0.0000	0.0000	0.0000	0.0000	0.0000	0.0008	0.0008	0.0000	0.0000
N2	0.0000	0.7732	0.0000	0.9451	0.0000	0.0000	0.9451	0.7732	0.9451	0.9451	0.0000	0.0058	0.0058	0.0000	0.0075
O2	0.0000	0.2074	0.0000	0.0310	0.0000	0.0000	0.0310	0.2074	0.0310	0.0310	0.0000	0.0002	0.0002	0.0000	0.0003
SO2	0.0000	0.0000	0.0000	0.0000	0.0000	0.0000	0.0000	0.0000	0.0000	0.0000	0.0000	0.0075	0.0075	0.0000	0.0000
SO3	0.0000	0.0000	0.0000	0.0000	0.0000	0.0000	0.0000	0.0000	0.0000	0.0000	0.0000	0.0000	0.0000	0.0000	0.0000
V-L Flowrate (kgmol/hr)	0	68596	0	56113	0	0	56128	68596	56128	56128	0	13532	20927	0	12935
V-L Flowrate (kg/hr)	0	1979393	0	1579931	0	0	1580361	1979393	1580361	1580361	0	477718	739671	0	509103
Solids Flowrate (kg/hr)	200303	0	9615762	10016978	10015225	1753	1753	0	1753	0	1753	12625	19468	20745	0
Temperature (oC)	15	15	921	1049	1049	15	1049	403	111	123	111	343	149	27	57
Pressure (Mpa, abs)	0.10	0.10	0.10	0.10	0.10	0.10	0.10	0.15	0.10	0.11	0.10	0.10	0.10	0.10	0.10
Density (kg/m3)		1.2	4729.2		4527.4	5020.1	0.3	0.8	0.9	0.9	4527.4	0.7	1.0	2285.3	1.5
V-L Molecular Weight	0	29	0	28	0	0	28	29	28	28	0	35	35	0	39
V-L Flowrate (lbmol/hr)	0	151229	0	123707	0	0	123740	151229	123740	123740	0	29832	46136	0	28517
V-L Flowrate (lb/hr)	0	4363814	0	3483151	0	0	3484099	4363814	3484099	3484099	0	1053188	1630695	0	1122380
Solids Flowrate (lb/hr)	441592	0	21199127	22083655	22079791	3865	3865	0	3865	0	3865	27833	42919	45734	0
Temperature (oF)	59	59	1690	1920	1920	59	1920	758	232	253	232	650	300	80	135
Pressure (psia)	14.7	14.7	14.7	14.7	14.7	14.7	14.7	21.9	14.7	15.8	14.6	14.7	14.6	14.5	14.7
AspenPlus Enthalpy (Btu/lb)	-902.3	-41.9	-3738.7		-3781.2	-3546.3	440.1	131.2	-12.9	-3.1	-4141.2	-4000.0	-4094.4	-4590.6	-3963.3
Density (lb/ft3)		0.0762	295.2321		282.6380	313.3920	0.0162	0.0484	0.0558	0.0580	282.6380	0.0447	0.0652	142.6671	0.0911

	16	17	18	19	20	21	22	23	24	25	26	27	28	29
V_L Mole Fraction														
Ar	0.0008	0.0005	0.0000	0.0000	0.0000	0.0092	0.0092	0.0000	0.0000	0.0000	0.0000	0.0000	0.0000	0.0000
CO2	0.9874	0.6400	0.0000	0.0000	0.0000	0.0003	0.0003	0.0000	0.0000	0.0000	0.0000	0.0000	0.0000	0.0000
H2	0.0000	0.0000	0.0000	0.0000	0.0000	0.0000	0.0000	0.0000	0.0000	0.0000	0.0000	0.0000	0.0000	0.0000
H2O	0.0022	0.3533	1.0000	1.0000	1.0000	0.0099	0.0099	1.0000	1.0000	1.0000	1.0000	1.0000	1.0000	1.0000
HCl	0.0000	0.0000	0.0000	0.0000	0.0000	0.0000	0.0000	0.0000	0.0000	0.0000	0.0000	0.0000	0.0000	0.0000
N2	0.0091	0.0059	0.0000	0.0000	0.0000	0.7732	0.7732	0.0000	0.0000	0.0000	0.0000	0.0000	0.0000	0.0000
O2	0.0004	0.0003	0.0000	0.0000	0.0000	0.2074	0.2074	0.0000	0.0000	0.0000	0.0000	0.0000	0.0000	0.0000
SO2	0.0000	0.0000	0.0000	0.0000	0.0000	0.0000	0.0000	0.0000	0.0000	0.0000	0.0000	0.0000	0.0000	0.0000
SO3	0.0000	0.0000	0.0000	0.0000	0.0000	0.0000	0.0000	0.0000	0.0000	0.0000	0.0000	0.0000	0.0000	0.0000
V-L Flowrate (kgmol/hr)	10601	4660	4472	7856	8	12497	12497	105713	87890	87890	73919	60231	79966	105713
V-L Flowrate (kg/hr)	464285	161810	80558	141540	142	360606	360606	1904458	1583363	1583363	1331676	1085071	1440612	1904458
Solids Flowrate (kg/hr)	0	0	20140	673	24110	0	0	0	0	0	0	0	0	0
Temperature (oC)	30	316	15	57	57	15	149	593	354	594	362	39	37	290
Pressure (Mpa, abs)	15.27	0.07	0.20	0.10	0.10	0.10	0.12	24.23	4.90	4.73	0.95	0.01	0.01	27.65
Density (kg/m3)	739.1	0.5	1147.2	991.4	4098.3	1.2	1.0	69.2	18.6	12.1	3.3	0.1	993.2	765.0
V-L Molecular Weight	44	35	22	18	116	29	29	18	18	18	18	18	18	18
V-L Flowrate (lbmol/hr)	23371	10272	9858	17320	17	27551	27551	233058	193764	193764	162964	132786	176295	233058
V-L Flowrate (lb/hr)	1023573	356730	177600	312041	312	795000	795000	4198611	3490717	3490717	2935843	2392172	3176005	4198611
Solids Flowrate (lb/hr)	0	0	44400	1484	53152	0	0	0	0	0	0	0	0	0
Temperature (oF)	86	600	59	135	135	59	300	1100	670	1101	683	102	99	553
Pressure (psia)	2214.5	10.0	29.7	14.7	14.7	14.7	17.4	3514.7	710.8	685.8	137.7	1.0	0.9	4010.0
AspenPlus Enthalpy (Btu/lb)	-3926.4	-4035.7	-6547.7	-6746.1	-4658.8	-41.9	16.6	-5375.0	-5545.4	-5299.5	-5501.9	-5834.5	-6803.1	-6321.3
Density (lb/ft3)	46.1410	0.0306	71.6147	61.8913	255.8464	0.0762	0.0615	4.3192	1.1634	0.7553	0.2056	0.0032	62.0010	47.7597

Table 8 550 MW CDCL power generation process performance summary

Coal Feed Rate, kg/h (lb/h)	200,303 (441,592)
Total HHV Heat Input, kWt (MMBTU/h)	1,508,558 (5,152)
Gross Electric Power Output, kWe	656,782
Total Auxiliaries, kWe	103,560
Net Electric Power Output, kWe	553,222
Net Plant HHV Heat Rate, kJ/kWh (Btu/kWh)	9,817 (9,312)
Net Plant HHV Efficiency, %	36.7%
CO_2 Capture Efficiency, %*	98.9%
Net CO_2 Emissions, kg/MWhnet (lb/MWhnet)	9.8 (21.5)
Raw Water Withdrawal, m^3/min (gpm)	23.0 (6,082.0)
Cooling Tower Load, GJ/h (MMBTU/h)	2,951 (2,797)
*CO_2 capture efficiency = (carbon in CO_2 product for geologic storage) ÷ (carbon in fuel + carbon in FGD sorbent – carbon in ash – carbon in FGD byproduct)	

3.4 Cost Update from HEN Optimization

Based on the heat and material balance of the overall process model with the updated HEN design in Figure 75, the project team estimated the cost savings of the CDCL island with the corresponding heat exchanger configuration. Using B&W's in-house database, the surface area of each heat exchanger was estimated using corresponding heat transfer coefficients and stream information. The change in surface area was compared to earlier estimates. The changes in surface configuration and area was evaluated and translated to weight and cost savings associated with the supply and fabrication of the heat exchanger bundles and associated components. Specifically, the cost analysis was performed to reflect the changes of total surface area due to changes in heat transfer arrangement based on optimization studies. The arrangement capitalizes on the higher heat transfer coefficients in the in-bed heat exchanger sections within the combustor which is significantly higher than the heat transfer coefficients for the tube banks within the convection passes of the reducer and combustor gas outlet. The optimization leads to a shift in tube sections from the convection pass to the IBHX section and results in nearly a 36 % reduction of surface area within the tube bank sections from earlier estimates. This reduction translates to cost savings of $14.5M in equipment cost and $8.1M in labor cost with a weight reduction of 7.6 Mlbs. The

corresponding Bare Erected Cost (BEC) saving is $22.5M which then translates to Total Cost Savings of $27.2M. These savings take into consideration adjustments in the following:

- Heat Exchanger Tubing and Header Piping
- Fabrication and Supply of the Heat Exchanger Sections
- Tubing Flue Platework
- Flue Refractory Lining, Insulation & Lagging
- Support Rods for Flues and Ducts
- Suspension Steel -Hanger Rods
- Structural Steel, Supports and Attachments
- Erection Labor
- Construction Management & Home Office Fees, Process & Project Contingencies

During this effort additional cost saving measures were identified, such as the need for only one FGD unit for the current design of a CDCL plant rather than two required in previous designs. Besides, because of the changes on the HEN design, modifications are needed to the arrangement of the overall 550 MWe CDCL plant, which may also potentially lead to additional cost savings. These items will be further reviewed and discussed in the pre-FEED project that is looking at the broader system level components.

4. Dynamic Modeling of Integrated CDCL-Steam Cycle System

A dynamic model of the 10 MWe CDCL pilot plant is developed to study the dynamics and transient behavior of the system. The design of the 10 MWe CDCL pilot plant is developed in project DE-FE0027654 "10 MWe CDCL Large Pilot Plang – Pre-FEED Study". The CDCL pilot plant is designed to include four parallel 2.5 MWe reactor systems, each include a counter-current moving bed reducer, a fluidized bed combustor, a riser, and the associated gas sealing devices and solid circulation device (L-valve). The steam cycle is an existing 20 MWe sub-critical steam cycle installed at the Dover Light & Power plant.

The dynamic model is developed in the ProTRAX simulation software. The steam cycle is simulated using the intrinsic modules/blocks in ProTRAX, while the CDCL system is simulated using custom model coded in FORTRAN.

4.1 Dynamic Modeling of Pilot Scale CDCL System

4.1.1 Physical Model

The chemical looping system considered here is a CFB system, which consists of a fluidized bed combustor, a lean phase riser, and a packed/moving bed reducer, as shown in Figure 77. The solid particles in the fluidized bed reactor will be entrained by gas, enter the lean phase riser above, and be transported upwards. After gas-solid separation, the particles will fall into the moving bed and move downwards in a packed manner. At the bottom of the moving bed reducer, the particles are transported into the fluidized bed reactor again by a non-mechanical valve, i.e. L-valve.

Coal is entrained by a carrier gas and introduced into the middle of the reducer. Oxygen carriers in the reducer heats the coal to the bed temperature and react with the volatiles generated. An enhancer gas flow, consists of CO_2 and H_2O, is introduced from the bottom of the reducer. The enhance flows upwards and gasifies the coal / coal char that flows down along with the solids to form combustible gases, which is converted by the oxygen carriers to form CO_2 and H_2O. The overall reaction in the reducer is:

$$FeO_x + CH_{2b}O_{2c} \cdot dH_2O = FeO_y + CO_2 + (b+d)H_2O \tag{4.1}$$

where

$$x - y = 1 - \frac{1}{2}b - c$$

In the reducer, the oxygen carrier particles lose heat due to the reaction with coal and reactor heat loss. The flue gas leaves the reducer from its top and enters a series of heat exchangers for energy recovery.

The reduced oxygen carriers are transported into the combustor, where they are oxidized by air:

$$FeO_y + \frac{(x-y)}{2} O_2 = FeO_x \tag{4.2}$$

Part of the heat released in this reaction is recovered by two in-bed heat exchangers (IBHX) to generate steam. The rest of the energy is used to heat the oxygen carriers and the air to the operating temperature. In addition, natural gas is introduced to the combustor for start-up purpose.

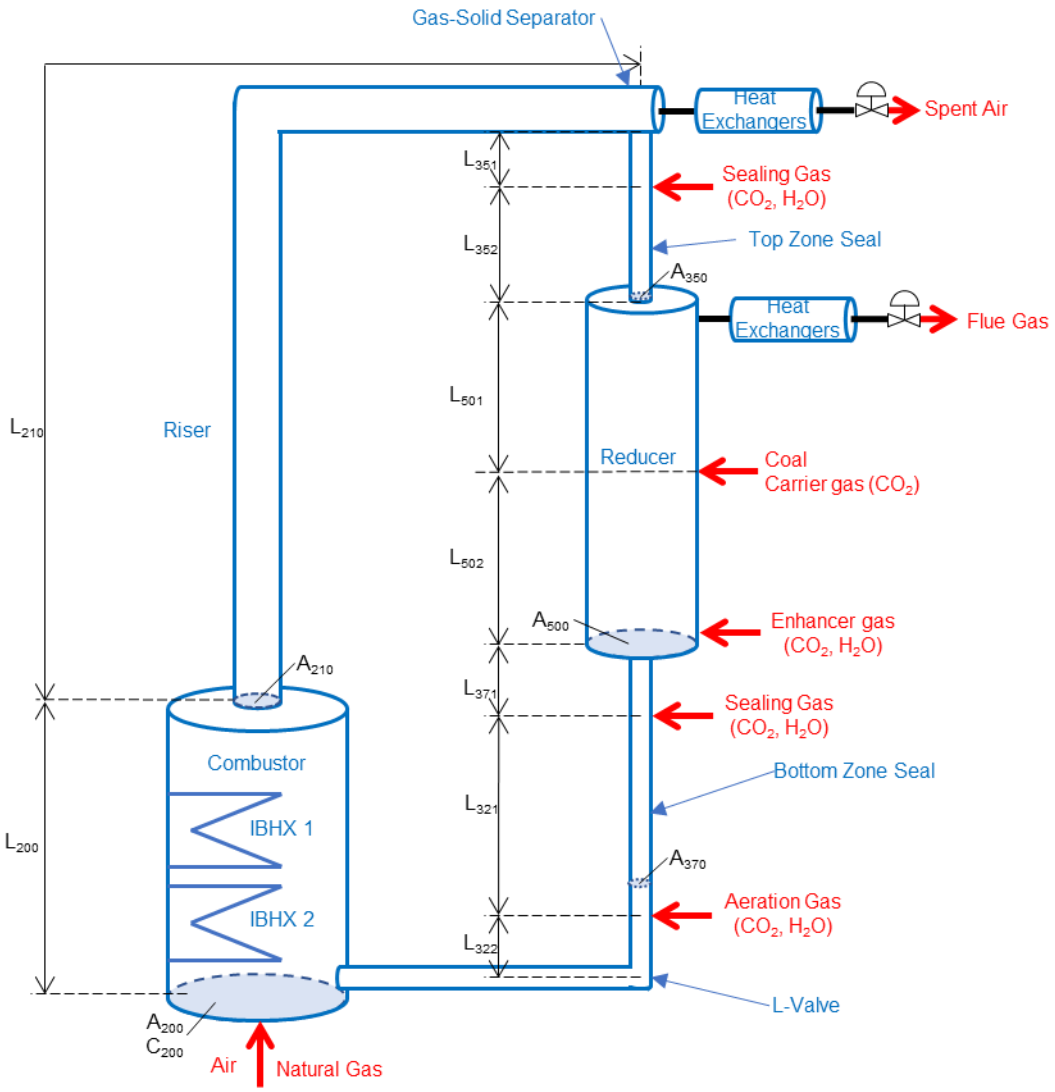

Figure 77 Conceptual model of the

The reducer, combustor, and other components of the CDCL system is constructed using refractory-lined water walls. The water walls are metal walls cooled by embedded water tubes. A layer of refractory material is lined between the metal wall and the high-temperature bed material in the reactor. The heat dissipated through the refractory material will be recovered by the water/steam in the water walls and be used to generate steam.

Two IBHX are installed in the combustor. One of the IBHX is used as the generation bank, which boils water from the vertical separator and generates steam. The other IBHX is used as the final super heater, which super heats the steam before it is sent to the steam turbine system. Figure 78 shows the heat integration scheme developed in the Pre-FEED project DE-FE0027654 for the 10 MWe CDCL pilot plant.

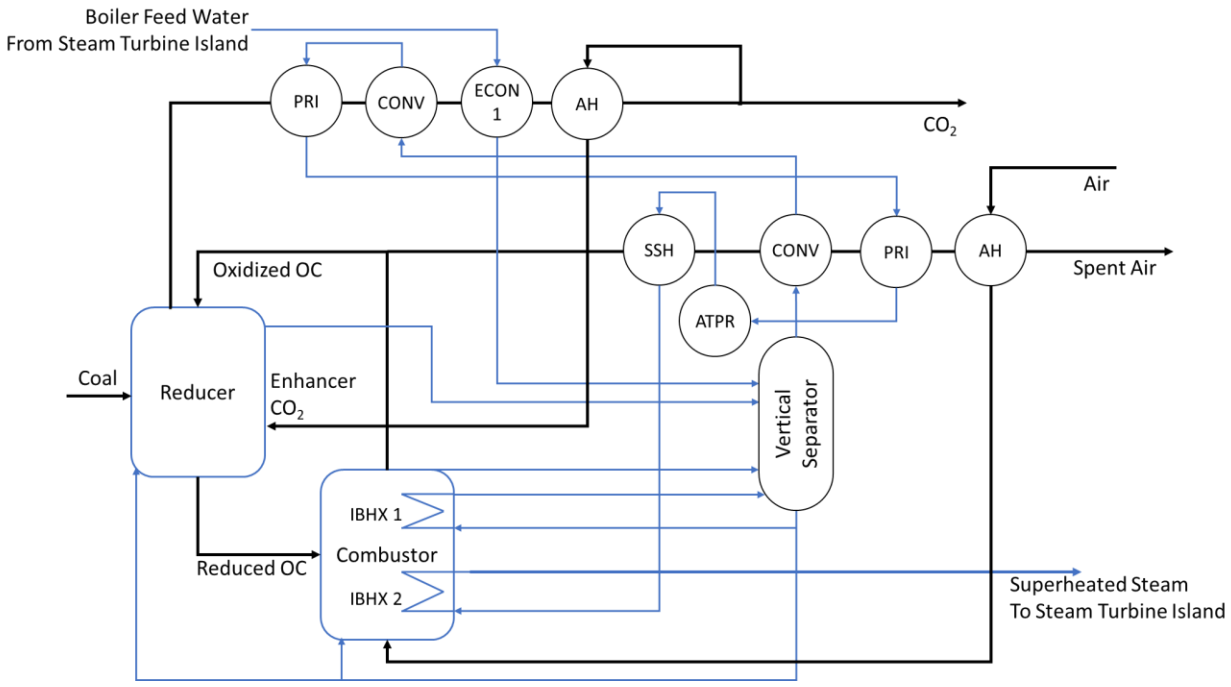

Figure 78 Heat Exchange Network for the 10 MWe CDCL Pilot Plant

4.1.2 Mathematical Model

To efficiently simulate the CDCL system at large time scale, the following assumptions are made for simplification.

- The gases in the system follows the ideal gas law: $pV = nRT$.

- Due to the large heat capacity between the oxygen carrier particles and the gases, the gas temperature is assumed to be the same as the solid temperature at a given location.
- The moving bed reactor is simulated as a one-dimensional flow reactor. Due to numerical considerations as discussed in Section 4.1.3, it is further simplified as 101 CSTR reactors in series. Each CSTR reactor has a uniform temperature, gas composition, and solid conversion (Figure 79).
- The fluidized bed combustor is simulated as a CSTR reactor. Thus, it has a uniform temperature, gas composition, and solid conversion.
- The transient change of pressure gradient along the moving bed is not simulated because its time scale (~1s) is significantly shorter than the time scale of interest.
- The inner refractory wall temperature is assumed to be equal to the bed temperature. This corresponds to a very large heat transfer coefficient between the bed and the reactor wall, resulting in an over-estimation of reactor heat loss.
- The heat transfer resistance of the metal wall is omitted. The outer refractory wall temperature is assumed to be the water / steam temperature in the water wall. This is reasonable because the thermal conductivity of the refractory material is much smaller than that of the metal wall.

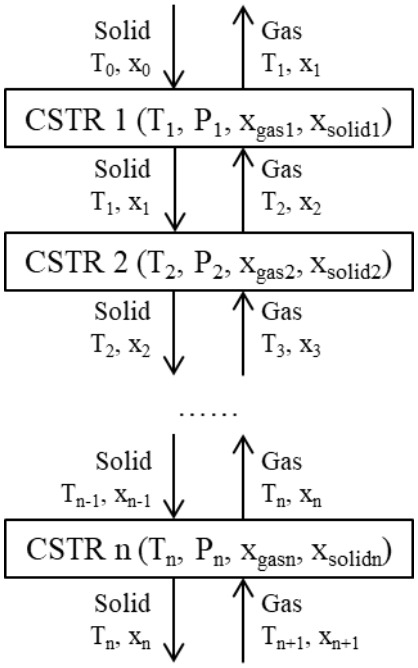

Figure 79 Counter-current Moving Bed Simulated as CSTR reactors in series

The moving bed side of the reactor is simulated as a series of CSTR reactors (Figure 79). For each CSTR reactor, mass balance and heat balance are simulated. Mass balance of gas gives:

$$\frac{dn_{i,j}}{dt} = F_{i,j}^{in} - F_{i,j}^{out} + r_{i,j} \tag{4.3}$$

where $F_{i,j}^{in}$ and $F_{i,j}^{out}$ are the flow rate of gas *i* flowing into and out of CSTR *j*, respectively. $r_{i,j}$ is the rate of generation of gas *i* in CSTR *j* due to chemical reactions. $n_{i,j}$ is the mole amount of gas *i* in CSTR *j*. The gas flow rate between the CSTR reactors satisfies:

$$F_{i,j}^{in} = F_{i,j-1}^{out} \tag{4.4}$$

The flow rate between two CSTRs can be determined by hydrodynamics:

$$\frac{\Delta P}{\Delta h} = \frac{150\mu(1-\epsilon)^2}{d_p^2\epsilon^3}v + \frac{1.75\rho(1-\epsilon)}{d_p\epsilon^3}v|v| \tag{4.5}$$

where ΔP is the pressure difference between the two CSTRs; v is the gas velocity between the two CSTRs; μ, ρ, ϵ, and d_p are the gas viscosity, gas density, bed voidage, and particle diameter, respectively.

At the bottom boundary of the moving bed reducer, the inlet gas flow rate and temperature are set by the enhancer gas flow. At the top boundary of the reducer, the outlet gas flow rate is determined by the pressure difference between the reducer and the ambient pressure and the outlet valve opening.

The mass balance of oxygen in solids gives:

$$\frac{dX_j}{dt} = \frac{F_{Fe}\left(X_j^{in} - X_j^{out}\right)}{n_{Fe,j}} + \frac{r_{O,j}}{1.5n_{Fe,j}} \tag{4.6}$$

where F_{Fe} is the mole flow rate of iron in the moving bed reducer, which is a constant along the moving bed reducer based on the plug-flow assumption. n_{Fe} is the mole amount of iron in CSTR *j*. $r_{O,j}$ is the rate of oxygen consumption due to chemical reactions. X_j is the oxygen carrier conversion in CSTR *j*, defined by:

$$X_j = 1 - \frac{n_{O,j}}{1.5n_{Fe,j}} \tag{4.7}$$

where $N_{O,j}$ is the mole amount of oxygen that can be reduced in the oxygen carrier in CSTR *j*. When the oxygen carrier is at Fe_2O_3 oxidation state, the conversion is $X = 0$; when the oxygen carrier is at Fe_3O_4 oxidation state, the conversion is $X = 1/9$; when the oxygen carrier is at FeO oxidation state, the conversion is $X = 1/3$; when the oxygen carrier is at Fe oxidation state, the conversion is $X = 1$.

At the top boundary of the moving bed, the inlet solid conversion and temperature is determined by the solid condition in the combustor.

The heat balance of in the CSTR gives:

$$\left(\sum_i n_{i,j} C_{P,i,j}\right) \frac{dT_j}{dt} = \sum_i C_{P,i,j} F_i^{in} \left(T^{in} - T_i\right) - \Delta H_j + \dot{Q}_J \tag{4.8}$$

where $C_{P,i,j}$ is the heat capacity of species *i* in CSTR *j*. The species considered here include gases, iron oxides at different oxidation states, and the support material in the oxygen carriers. T^{in} is the inlet temperature of the gas and solid flows. For upward-flowing gases, $T^{in} = T_{i+1}$; for downward-flowing solids, $T^{in} = T_{i-1}$. ΔH_j and $\dot{Q}_j$ are the heat of reaction and heat loss occurring in the CSTR, respectively. The heat loss is calculated by:

$$\dot{Q}_J = -h_j C_j \frac{(T_i - T_w)}{W} k_r \tag{4.9}$$

where h_j and C_j are the height and perimeter of the CSTR; W and k_r are the thickness and the thermal conductivity of the refractory wall, and T_w is the water / steam temperature in the water wall.

The mass balance of gas in the combustor yields an equation similar to equation (4.3). The inlet gas flow rate and temperature are determined by the air and natural gas flow. The outlet flow rate is determined by the pressure difference between the combustor and the ambient pressure. The energy balance in the combustor yields an equation similar to equation (4.8). Due to the existence of IBHX, the heat loss term is calculated by:

$$\dot{Q}_c = -h_c C_c \frac{(T_c - T_w)}{W} k_r - (ha)_1 (T_c - T_1) - (ha)_2 (T_c - T_2) \tag{4.10}$$

where h_j and C_j are the height and perimeter of the combustor; T_w, T_1, and T_2 are the water / steam temperature in combustor metal walls and the two IBHX, respectively; T_c is the bed temperature of the fluidized bed combustor; $(ha)_i$ is the product of heat transfer coefficient and the surface area of the IBHX, which is a function of hydrodynamic condition in the fluidized bed.

The parameters used in the mathematical model are taken from the pilot plant design generated in the Pre-FEED project DE-FE0027654 or estimated from the designed operating condition.

4.1.3 Numerical Considerations and Simplifications

The time scales involved in the simulation of the CDCL system span a wide range. The characteristic time for chemical reaction kinetics involved in the process, e.g. the reaction between the oxygen carriers and combustible gases in the moving bed reducer, can be as short as 10^{-3}s. The

characteristic time for transient change of pressure differentials in the system, e.g. when a sudden change in gas flow occurs, is also in 10^{-3}s. The characteristic time for gas convection in the system is in seconds. The characteristic time for temperature ramping may be in the range of hours. Thus, the numerical simulation of such a system will encounter the stiffness problem. If a very short numerical time step is chosen to capture detailed behavior of chemical reactions and transient pressure variation, the simulation may be very slow and inefficient for long-time behaviors.

In this project, the dynamic behaviors that are closely related to the system ramping and steam generation are of interest. Thus, the model is simplified to omit the sub-second dynamics. The kinetics of chemical reactions in the moving bed reducer is not simulated. Instead, the model assumes that the gases in the reducer reaches thermodynamic equilibrium with the oxygen carriers.

In addition, the way to discretize the moving bed reactor is adjusted. Conventionally, a plug flow reactor can be described by partial differential equations such as:

$$\frac{\partial n_i}{\partial t} = -u_g \frac{\partial n_i}{\partial h} + V \cdot r_i$$

$$\frac{\partial T}{\partial t} = -u_g \frac{\partial T}{\partial h} + \frac{\dot{Q} - \Delta H_R}{\sum n_i C_{p,i}}$$

$$\frac{\partial P}{\partial h} = \frac{150\mu(1-\epsilon)^2}{d_p^2 \epsilon^3} v + \frac{1.75\rho(1-\epsilon)}{d_p \epsilon^3} v|v|$$

Numerical solution of these equations in a counter-current moving bed requires special discretization techniques in order to prevent negative solutions and instability. Numerical integration time step needs to be very small. To simplify the numerical scheme and reduce computation time, the reactor is simulated as 101 CSTR reactors. This results in numerical dispersion of mass and energy along the axial direction.

The accumulation of gas in the individual CSTRs of the reducer is omitted. Equation (4.3) is changed to:

$$n_j \frac{dx_{i,j}}{dt} = F_j^{in} x_{i,j+1} - F_j^{out} x_{i,j} + r_{i,j} \tag{4.11}$$

where F_j^{in} and F_j^{out} are the total flow rate of gas flowing into and out of CSTR *j*, respectively; $x_{i,j}$ is the mole fraction; $r_{i,j}$ is the rate of generation of gas *i* in CSTR *j* due to chemical reactions; n_j is the total mole amount of gas in CSTR *j*, which is calculated from the pressure of the CSTR. This simplification may break mass balance slightly. However, the simplification, along with the use of

CSTRs in series, result in an increase of numerical integration time step from $2.5 \times 10^{-4} s$ to $5 \times 10^{-2} s$, or a 95% reduction of computation time.

4.2 Dynamic Modeling of Steam Cycle

The 20 MWe steam cycle installed at the Dover Light & Power plant is simulated in the ProTRAX simulation software. ProTRAX is a commercial process simulation software specialized in power plant simulation. It includes built-in models for common components in thermal power plants such as turbines, heat exchangers, pumps, valves, and other accessories. ProTRAX models are configured in a graphical programming environment, where icons of various modules are placed and interconnected by streams. ProTRAX compiles the graphical program into executable files, which are used to perform dynamic simulation.

Figure 80 shows the graphical program of the steam cycle model, which includes the steam turbine, condenser, feed water heaters, feed water pump, and other accessories. The design and operating parameter used in the model is obtained from Dover Light & Power.

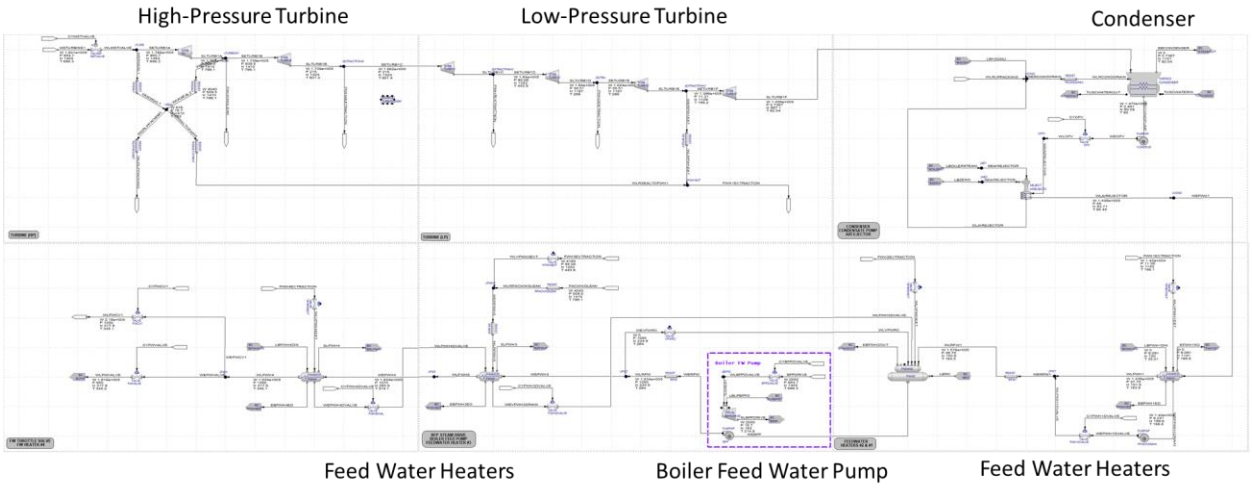

Figure 80 ProTRAX model of 20 MWe steam cycle

The steam generated from the existing boiler or the CDCL reactor is feed to the steam turbines, which is simulated as 6 turbine modules in the ProTRAX model. Leaks through the packing as well as the steam extraction between the turbine stages are modeled. The leaked or extracted steam are sent to four feed water heaters to preheat the feed water.

The spent steam/water from the low-pressure turbine is sent to a condenser, where it is condensed to liquid state. A condenser pump and a feed water pump drive the feed water through four feed water heaters and eventually enters the boiler or the CDCL system.

The heat exchanger network shown in Figure 78 is also simulated in ProTRAX. The IBHX and the water walls of the reducer and the combustor are simulated using the built-in PIPEQ module. The CDCL dynamic model calculates the heat duty to the PIPEQ modules based on the steam/water temperature of the modules. PIPEQ modules calculates the enthalpy change of the steam/water based on the heat duty provided by the CDCL model. Besides, the CDCL model calculates the gas flows and compositions from the reducer and combustor, which are fed to the streams in the ProTRAX steam cycle model. Table 9 summarizes the variables exchanged at the boundary of the CDCL model and the ProTRAX steam cycle model.

Table 9 Variables exchanged at the boundary of the two dynamic models

FLOW STREAM / COMPONENT	**INPUT VARIABLES** (from Steam Cycle Model to CDCL)	**OUTPUT VARIABLES** (from CDCL to Steam Cycle Model)
Enhancer Gas	Enthalpy, Composition, Flowrate	Back Pressure
Reducer Exit Gas	Pressure	Enthalpy, Composition, Flowrate
Combustor Exit Gas	Pressure	Enthalpy, Composition, Flowrate
FD Fan Air	Enthalpy, Flowrate, Composition	Back Pressure
Coal	none	Flowrate
GB	Temperatures	Heat Rate
FSH	Temperatures	Heat Rate
Waterwall	Temperatures	Heat Rate
NG into Combustor for start-up	Flowrate, Enthalpy	Back Pressure

4.3 Dynamics of Integrated CDCL-Steam Cycle System

4.3.1 Designed Operating Condition

Table 10 summarizes the steady state flow rate, enthalpy, and temperature of key streams or locations in the steam cycle. At designed operating condition, the steam cycle consumes 1.8×10^5 lb/hr of super-heated steam at 865 psia and 898F, and generates 20 MWe power. Note that only one 2.5 MWe CDCL module is shown in this condition.

Table 10 Steam/water conditions in the steam cycle

Location	Flow rate (lb/hr)	Pressure (psia)	Enthalpy (BTU/lb)	Temperature (°F)
Master steam feed to turbine	1.80×10^5	865	1453	898
Turbine outlet	1.44×10^5	0.7	997	92.4
Condenser outlet	1.48×10^5	2.5	60	92
Boiler feedwater pump outlet	1.83×10^5	1080	235	264
Feed water to boiler	1.62×10^5	950	318	345
Feed water to single 2.5 MWe CDCL module	2.16×10^4	1050	318	345
Steam drive for boiler feedwater pump	2000	865	1453	898

Table 11 summarizes the operating parameters of the CDCL pilot plant dynamic model at full load condition. The corresponding thermal input to the CDCL system is about 9.5 MW_{th}. Table 12 summarizes the performance of the CDCL pilot plant at steady state of full load operation as simulated by the dynamic model. The performance obtained from the steady state of the dynamic model is in close agreement with the designed performance as developed in the Pre-FEED project, showing that the dynamic model correctly simulates the heat and material balance of the CDCL pilot plant.

Table 11 Operating parameters at full load condition

Stream	Flow rate (lb/hr)	Temperature (°F)	Composition
Combustor air	27,780	716	
Coal	2,593	59	C: 70.1% wt O: 7.30% wt H: 4.77% wt Moisture: 5.4% wt Ash: 9.5% wt HHV: 12,563 BTU/lb
Coal carrier gas	1,549	500	69% CO_2, 31% H_2O
Enhancer gas	1,137	494	69% CO_2, 31% H_2O

Table 12 Performance of CDCL pilot plant at full load condition

Outlet Stream Conditions			
	Flow rate (lb/hr)	**Temperature (°F)**	**Composition**
Combustor outlet gas	22,235	1873	$x_{O_2} = 3.3\%$
Combustor outlet solid	268,881	1873	X_{solid}=0.8%
Reducer outlet gas	10,611	1870	$x_{CO_2} = 69\%$
Reducer outlet solid	263,230	1663	X_{solid}=20.8%

Heat Exchanger Performances			
	Steam Temperature (°F)	**Steam Pressure (psia)**	**Heat Rate (kW)**
IBHX 1: Generation Bank	545	1002	5402
IBHX 2: Final Super Heater	905	880	171
Reducer water wall	545	1002	328
Combustor water wall	545	1002	392

As shown in Table 12, the IBHX and water walls recovers about 6.3 MW of thermal power. The rest is carried by the flue gases from the reducer and the combustor, which is recovered by the heat exchangers in the convection path.

4.3.2 Ramping Dynamics of CDCL Pilot Plant

A simple ramp-down test is performed on the dynamic model of the CDCL pilot plant. At t=4 hr, the coal input flow rate is reduced to 90% of its full-load value. Correspondingly, the solid circulation rate is also reduced to 90% of the original value to maintain a constant coal-to-solid flow ratio. Meanwhile, the air flow rate, enhancer gas flow rate, and carrier gas flow rate are kept constant. The response of the system is shown in Figure 81 through 83. As shown in Figure 81, the combustor temperature reduced rapidly from 1873F to 1840F due to the reduction of solid flow rate. Meanwhile, oxygen mole fraction in the combustor increased rapidly to above 5%. However, the further reduction of bed temperature and power output take about 10 hours to eventually reach the new steady state. “Waves” in the temperature and power profiles are observed, which is a result of the slow propagation of low temperature particles through the moving bed reducer.

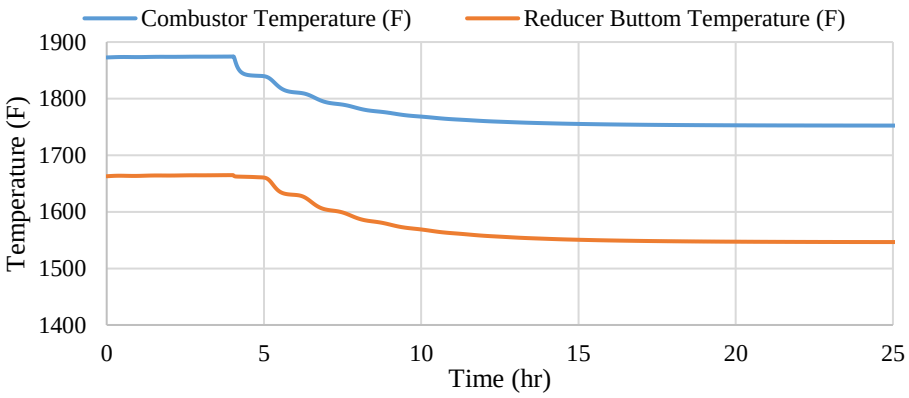

Figure 81 Bed temperature variation during ramp-down

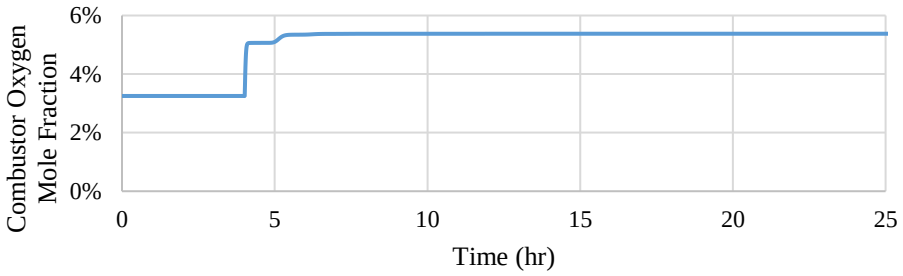

Figure 82 Combustor oxygen mole fraction variation during ramp-down

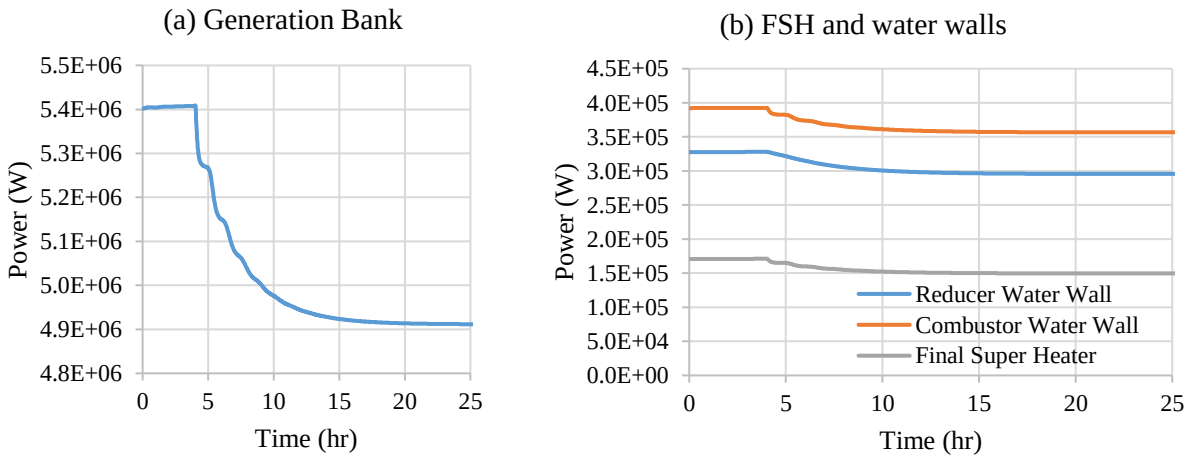

Figure 83 Power output of IBHX and water walls during ramp-down

A similar ramp-up simulation is performed after reaching steady state at 90% loading. The coal input flow rate is increased back to 100% of its full-load value. Correspondingly, the solid

circulation rate is also increased to the designed condition. Meanwhile, the air flow rate, enhancer gas flow rate, and carrier gas flow rate are kept constant. The response of the system is shown in Figure 84 through 86. Similar to the ramp-down test, oxygen mole fraction in the combustor decreased rapidly to 3% while the temperature and power output of the system take several hours to reach steady state.

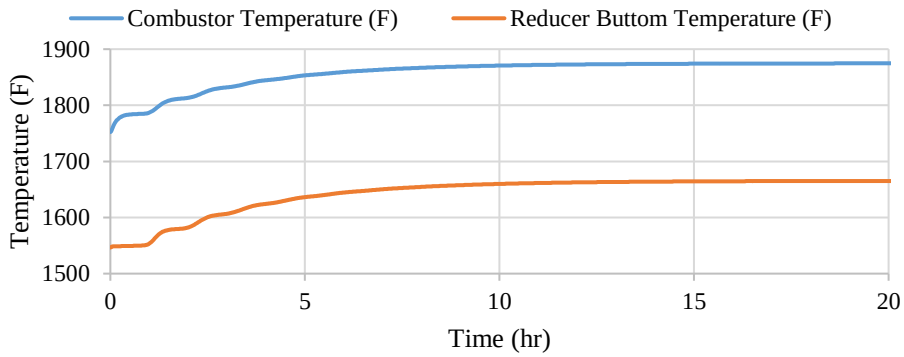

Figure 84 Bed temperature variation during ramp-up

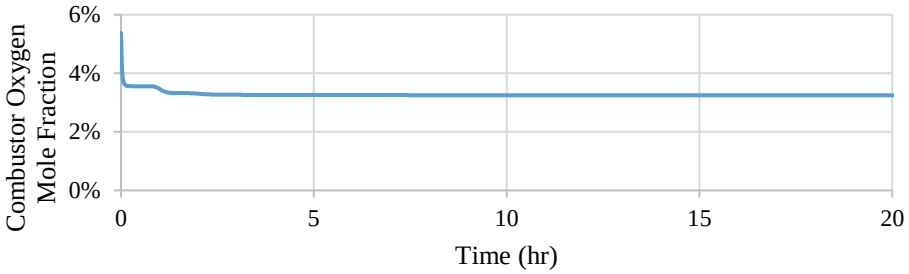

Figure 85 Combustor oxygen mole fraction variation during ramp-up

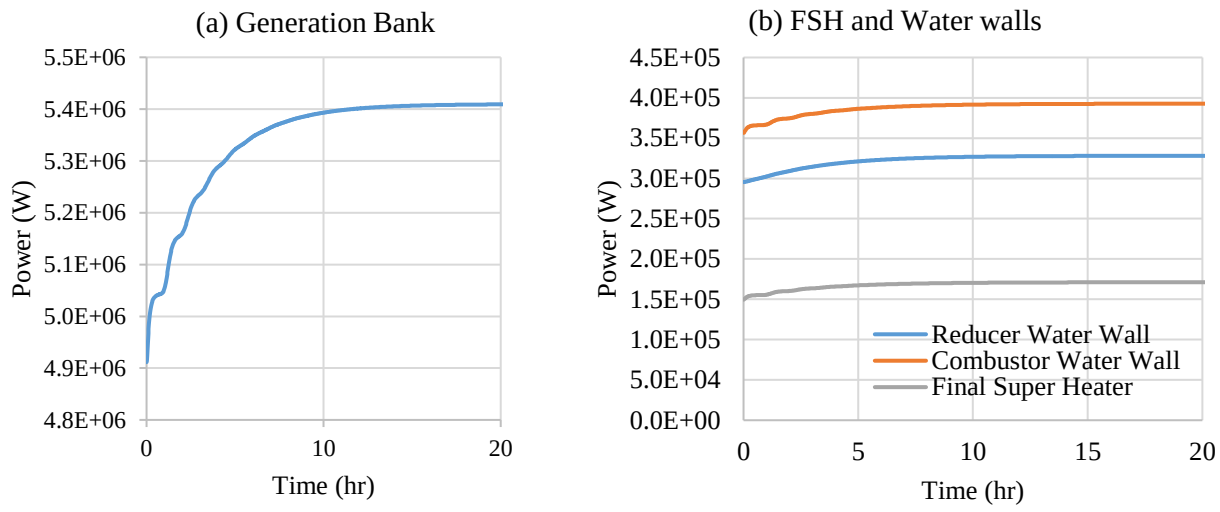

Figure 86 Power output of IBHX and water walls during ramp-up

The slow response of the CDCL system to load variation is due to the large amount of thermal energy stored in the oxygen carrier particles. The largest power output from the CDCL system is the generation bank located in the combustor as an IBHX, which can be calculated by:

$$Pw_{GB} = (ha)_{GB}(T_c - T_{GB})$$

The temperature of steam/water temperature in the generation bank, T_{GB}, is relatively stable due to the phase-change occurring in it. Thus, the power output of the generation bank is almost a linear function of the combustor temperature. To ramp down or ramp up the power output, the bed temperature has to vary significantly. However, due to the large amount of thermal energy stored in the oxygen carrier particles, varying the bed temperature can be time consuming. This slow response may cause problems to load-following operation of CDCL power plants.

Special control strategies can be developed to facilitate rapid ramp-up and ramp-down of the process. For example, one method to rapidly ramp-down the capacity of the system is:

1. Pause coal injection and oxygen carrier circulation.
2. Wait until the combustor temperature drop to the desired value.
3. Start coal injection and oxygen carrier circulation. Control the flow rate of coal and oxygen carrier to maintain a steady combustor temperature.

In the first step, after oxygen carrier circulation is paused, the IBHX and combustor air will remove a large amount of heat from the solids in the combustor. Thus, the power output of the CDCL system can be ramped down quickly. After the power output reaches the desired value, the system is adjusted to maintain this load level. The ramp-down dynamics of this strategy is shown

in Figure 87 and Figure 88. By actively controlling the flow rate of coal and oxygen carriers, the bed temperature and power output of the CDCL system reaches the steady state value within 2 hours. The desired temperature power output is first reached in about 20 minutes. This performance is much faster than simply reducing the coal input to the system. Although this strategy can ramp down the system power output rapidly, undesirable oscillation is still observed in the system variables. More sophisticated control algorithms such as model predictive control can be developed to further optimize the ramping control.

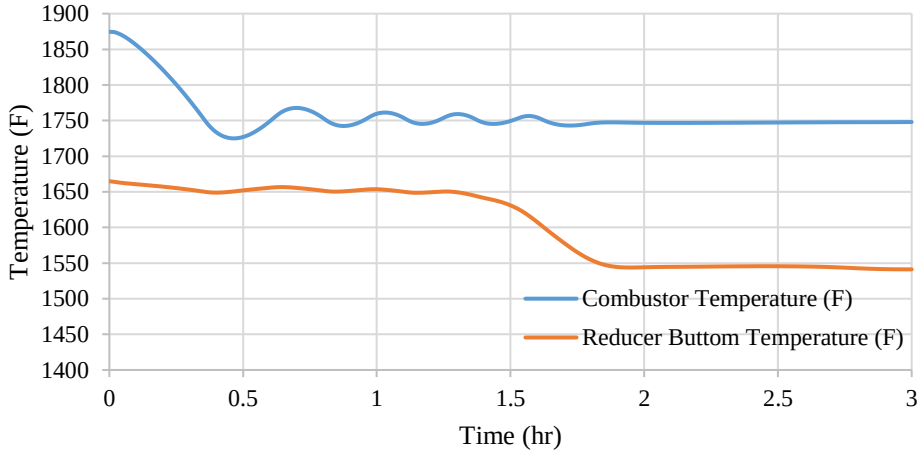

Figure 87 Bed temperature variation during controlled ramp-down

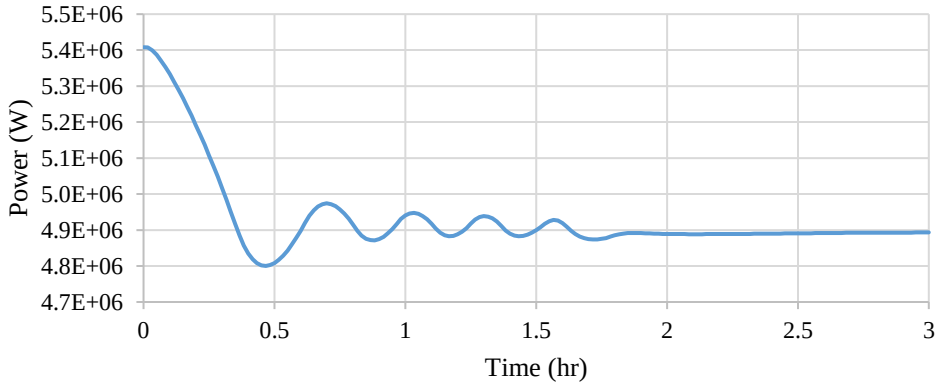

Figure 88 Generation bank IBHX heat rate variation during controlled ramp-down

5. References

1. Spitzer RH, Manning FS, Philbrook WO. Generalized model for the gaseous, topochemical reduction of porous hematite spheres. AIME Met Soc Trans. 1966 Dec;236(12):1715-24.
2. Abad A, Adanez J, Cuadrat A, García-Labiano F, Gayán P, Luis F. Kinetics of redox reactions of ilmenite for chemical-looping combustion. Chemical Engineering Science. 2011 Feb 15;66(4):689-702.
3. Spitzer RH, Manning FS, Philbrook WO. Mixed-control reaction kinetics in the gaseous reduction of hematite. AIME MET SOC TRANS. 1966 May;236(5):726-42.
4. Fuller EN, Giddings JC. A comparison of methods for predicting gaseous diffusion coefficients. Journal of Chromatographic Science. 1965 Jul 1;3(7):222-7.
5. Fuller EN, Schettler PD, Giddings JC. New method for prediction of binary gas-phase diffusion coefficients. Industrial & Engineering Chemistry. 1966 May 1;58(5):18-27.
6. Fuller EN, Ensley K, Giddings JC. Diffusion of halogenated hydrocarbons in helium. The effect of structure on collision cross sections. The Journal of Physical Chemistry. 1969 Nov;73(11):3679-85.
7. Mehrabadi M, Horwitz JA, Subramaniam S, Mani A. A direct comparison of particle-resolved and point-particle methods in decaying turbulence. Journal of Fluid Mechanics. 2018 Sep;850:336-69.
8. Igci Y, Andrews IV AT, Sundaresan S, Pannala S, O'Brien T. Filtered two-fluid models for fluidized gas-particle suspensions. AIChE Journal. 2008 Jun;54(6):1431-48.
9. Verma V, Deen NG, Padding JT, Kuipers JA. Two-fluid modeling of three-dimensional cylindrical gas–solid fluidized beds using the kinetic theory of granular flow. Chemical Engineering Science. 2013 Oct 11;102:227-45.
10. Wang J, van der Hoef MA, Kuipers JA. Why the two-fluid model fails to predict the bed expansion characteristics of Geldart A particles in gas-fluidized beds: a tentative answer. Chemical Engineering Science. 2009 Feb 1;64(3):622-5.
11. Goldschmidt, M.J.V., 2001. Hydrodynamic modeling of fluidized bed spray granulation. Ph.D. Thesis, University of Twente, Enschede, Netherlands
12. Bokkers, GA., 2005. Multi-level modeling of the hydrodynamics in gas phase polymerisation reactors. Ph.D. Thesis, University of Twente, Enschede, Netherlands

13. Garzó V, Tenneti S, Subramaniam S, Hrenya CM. Enskog kinetic theory for monodisperse gas–solid flows. Journal of Fluid Mechanics. 2012 Dec;712:129-68.
14. Wang D, Xu M, Marashdeh Q, Straiton B, Tong A, Fan LS. Electrical Capacitance Volume Tomography for Characterization of Gas-Solid Slugging Fluidization with Geldart Group D Particles under High Temperatures. Industrial & Engineering Chemistry Research. 2018 Jan 19.
15. Benyahia S, Syamlal M, O'Brien TJ. Extension of Hill–Koch–Ladd drag correlation over all ranges of Reynolds number and solids volume fraction. Powder Technology. 2006 Mar 1;162(2):166-74.
16. Lun CK, Savage SB, Jeffrey DJ, Chepurniy N. Kinetic theories for granular flow: inelastic particles in Couette flow and slightly inelastic particles in a general flowfield. Journal of fluid mechanics. 1984 Mar;140:223-56.
17. Schaeffer DG. Instability in the evolution equations describing incompressible granular flow. Journal of differential equations. 1987 Jan 1;66(1):19-50.
18. Stewart, P. S. B.; Davidson, J. F. Slug flow in fluidized beds. Powder Technol. 1967, 1, 61.
19. Wang D, Fan LS. Bulk coarse particle arching phenomena in a moving bed with fine particle presence. AIChE Journal. 2014 Mar 1;60(3):881-92.
20. Johnson PC, Jackson R. Frictional–collisional constitutive relations for granular materials, with application to plane shearing. Journal of fluid Mechanics. 1987 Mar;176:67-93.
21. Li T, Benyahia S. Revisiting Johnson and Jackson boundary conditions for granular flows. AIChE journal. 2012 Jul 1;58(7):2058-68.
22. Fullmer WD, Hrenya CM. Quantitative assessment of fine-grid kinetic-theory-based predictions of mean-slip in unbounded fluidization. AIChE Journal. 2016 Jan;62(1):11-7.
23. Milioli, C.C., Milioli, F.E., Holloway, W., Agrawal, K. and Sundaresan, S., 2013. Filtered two-fluid models of fluidized gas-particle flows: new constitutive relations. AIChE Journal, 59(9), pp.3265-3275.
24. Igci, Y., Andrews IV, A.T., Sundaresan, S., Pannala, S. and O'Brien, T., 2008. Filtered two-fluid models for fluidized gas-particle suspensions. AIChE Journal, 54(6), pp.1431-1448.

25. Fout T, Shultz T, Woods M, Turner MJ, Zoelle AJ, James III RE. Cost and Performance Baseline for Fossil Energy Plants, Volume 1: Bituminous Coal and Natural Gas to Electricity, Revision 4. NETL; 2018 Aug 2.
26. Woods MC, Matuszewski M, Summers WM. Quality guidelines for energy system studies: Specification for selected feedstocks. Tech. Rep. NETL/DOE-341/011812, US Department of Energy; 2012.
27. Black J. Quality guidelines for energy systems studies: Process modeling design parameters. Technical report, National Energy Technology Labratory. DOE/NETL-341/051314; 2014 May.